2012

Direct Measurement Of Thicknesses, Volumes Or Compositions Of Nanomaterials By Quantitative Atomic Number Contrast In High-angle Annular Dark-field Scanning Transmission Electron Microscopy

Biao Yuan
University of Central Florida

DIRECT MEASUREMENT OF THICKNESSES, VOLUMES OR COMPOSITIONS OF NANOMATERIALS BY QUANTITATIVE ATOMIC NUMBER CONTRAST IN HIGH-ANGLE ANNULAR DARK-FIELD SCANNING TRANSMISSION ELECTRON MICROSCOPY

by

BIAO YUAN
B.S., Inorganic Materials Science & Engineering, Zhejiang University, 1984
M.S., Inorganic Nonmetallic Materials Science & Engineering, Zhejiang University, 1987
M.C.I.S., Computer & Information Science, Cleveland State University, 2003

A dissertation submitted in partial fulfillment of the requirements
for the degree of Doctor of Philosophy
in the Department of Mechanical, Materials and Aerospace Engineering
in the College of Engineering and Computer Science
at the University of Central Florida,
Orlando, Florida

Summer Term
2012

Major Professor: Helge H. Heinrich

ABSTRACT

The sizes, shapes, volumes and compositions of nanoparticles are very important parameters determining many of their properties. Efforts to measure these parameters for individual nanoparticles and to obtain reliable statistics for a large number of nanoparticles require a fast and reliable method for 3-D characterization. In this dissertation, a direct measurement method for thicknesses, volumes or compositions of nanomaterials by quantitative atomic number contrast in High-Angle Annular Dark-Field (HAADF) Scanning Transmission Electron Microscopy (STEM) is presented. A HAADF detector collects electrons scattered incoherently to high angles. The HAADF signal intensity is in first-order approximation proportional to the sample thickness and increases with atomic number. However, for larger sample thicknesses this approach fails. A simple description for the thickness dependence of the HAADF-STEM contrast has been developed in this dissertation. A new method for the calibration of the sensitivity of the HAADF detector for a FEI F30 transmission electron microscope (TEM) is developed in this dissertation. A nearly linear relationship of the HAADF signal with the electron current is confirmed. Cross sections of multilayered samples provided by TriQuint Semiconductors in Apopka, FL, for contrast calibration were obtained by focused ion-beam (FIB) preparation yielding data on the interaction cross section per atom.

To obtain an absolute intensity calibration of the HAADF-STEM intensity, Convergent Beam Electron Diffraction (CBED) was performed on Si single crystals. However, for samples prepared by the focused ion beam technique, CBED often significantly underestimates the sample thickness. Multislice simulations from Dr. Kirkland's C codes are used for comparison with experimental results. TEM offers high lateral resolution, but contains little or no information on the thickness of samples. Thickness maps in energy-filtered TEM (EFTEM), CBED and tilt series are so far the only methods to determine thicknesses of particles in TEM. In this work I have introduced the use of wedge-shaped multilayer samples prepared by FIB for the calibration of HAADF-STEM contrasts. This method yields quantitative contrast data as a function of sample thickness. A database with several pure elements and compounds has been compiled, containing experimental data on the fraction of electrons scattered onto the HAADF detector for each nanometer of sample thickness. The use of thick samples reveals an increased signal at the interfaces of high- and low-density materials. This effect can be explained by the transfer of scattered electrons from the high density material across the interface into the less-absorbing low-density material. The calibrations were used to determine concentration gradients in nanoscale Fe-Pt multilayers as well as thicknesses and volumes of individual Au-Fe, Pt, and Ag nanoparticles. Volumes of nanoparticles with known composition can be determined with accuracy better than 15%. Porosity determination of materials becomes available with this method as shown in an example of porous Silicon.

THIS DISSERTATION IS DEDICATED TO MY FAMILY

ACKNOWLEDGMENTS

This dissertation would not have been possible without the continuous Graduate Research Assistantship support from my advisor, Professor Helge H. Heinrich, Ph.D., since May 2007. Neither would it have been possible without his encouragement, guidance, and cooperation. Thank you from the bottom of my heart.

I would like to thank my co-advisor, Professor Yongho Sohn, Ph.D., for the Graduate Research Assistantship support from August 2005 to May 2007 that gives me the chance to pursue my Ph.D. in Materials Science at University of Central Florida (UCF), and for serving on my dissertation committee as co-advisor.

I would like to thank Professors Kevin R. Coffey, Ph.D., Beatriz Roldan Cuenya, Ph.D., and Jiyu Fang, Ph.D., for serving on my dissertation committee. Their support is critical.

I would like to thank Professor Lee Chow, Ph.D., for serving on my dissertation committee until February 2012 due to his sabbatical leave out of country.

I would like to thank all faculty and staff members at Advanced Materials Processing and Analysis Center (AMPAC) at UCF for their service that makes Materials Characterization Facility (MCF) one of the state of the art facilities in materials. Especially, thank you Mr. Mikhail Klimov for keeping the Focused Ion Beam (FIB) and Transmission Electron Microscope (TEM) TECNAI running, thank you Mr. Kirk

Scammon for keeping the Scanning Electron Microscope (SEM) and X-Ray Diffractometer (XRD) running, thank you Ms. Karen Glidewell for processing my equipments reservation in time, thank you Ms. Cindy Harle, Ms. Kari Stiles and Ms. Angelina Feliciano for your excellent administrative support.

I would like to thank all faculty and staff members at Department of Mechanical, Materials, and Aerospace Engineering at UCF for their service that makes Materials Science Ph.D. program one of the top programs in materials.

I would like to thank Drs. E. Perez, Prabhakar Mohan, L. K. Ono, Gazi N. Aliev, Bo Yao, Mr. Aniruddha Dutta, Mrs. Haritha Nukala, and Miss. Hilary Palmer, for their cooperation.

I would like to thank Professor Stephen Kuebler, Ph.D., Mr. C. Grabill and Professor Beatriz Roldan, Ph.D., from UCF, as well as Drs. Gernot Fattinger, Taeho Kook, Paul Stokes, Kenneth Orlowsky, and Robert Aigner from TriQuint for providing calibration samples.

I would like to thank UCF College of Graduate Studies Travel Award program that partially supports my attending at Materials Science & Technology 2009 Conference & Exhibition in Pittsburgh, Pennsylvania.

I would like to thank UCF Student Government Association Travel Award program that partially supports my attending at Microscopy & Microanalysis 2010 Meeting in Portland, Oregon.

I would like to thank TriQuint Semiconductors, UCF, National Science Foundation (NSF), Siemens Westinghouse Power Corp., Mitsubishi Power Systems, Idaho National Engineering & Environmental Laboratory (INEEL), Clemson University, US Army Research Laboratory (ARL), Siemens Energy, Inc., National Renewable Energy Laboratory (NREL), etc. that fund my Assistantship and / or research either by grant or by work order.

Last, but not least, I am indebted to my family. It is a challenge to express my appreciation in language, especially in English as a second language. However, this dissertation is dedicated to my family.

It is possible that I forget to acknowledge those who support me anyway. If you are the one, I am sorry, please let me know. I can be reached at biaoyuanusa@knights.ucf.edu or biaoyuanusa@yahoo.com and would be happy to rewrite this acknowledgement.

TABLE OF CONTENTS

LIST OF FIGURES

LIST OF TABLES

LIST OF ACRONYMS/ABBREVIATIONS

2-D	Two-Dimensional Space
3-D	Three-Dimensional Space
ADF	Annular Dark Field
AFM	Atomic Force Microscopy
AMPAC	Advanced Materials Processing and Analysis Center
AP-FIM	Atom-Probe Field Ion Microscopy
BF	Bright-Field
CB	Contrast & Brightness
CBED	Convergent-Beam Electron Diffraction
CCD	Charge-Coupled Device
CPU	Central Processing Unit
DF	Dark-Field
EDX	Energy-Dispersive X-Ray Spectroscopy
EELS	Electron Energy-Loss Spectroscopy

EFTEM	Energy Filtered Transmission Electron Microscopy
EXAFS	Extended X-Ray Absorption Fine Structure
FIB	Focused Ion Beam
FL	Florida
HAADF	High-Angle Annular Dark-Field
HRTEM	High-Resolution Transmission Electron Microscopy
K-M	Kossel-Möllenstedt
LAADF	Low Angle Annular Dark Field
MCF	Materials Characterization Facility
NP	Nano Particle
QD	Quantum Dot
STDEV	Standard Deviation
STEM	Scanning Transmission Electron Microscopy
TDS	Thermal Diffuse Scattering
TEM	Transmission Electron Microscopy
TOF	Time-Of-Flight

UIUC	University of Illinois at Urbana–Champaign
XANES	X-Ray Absorption Near Edge Structure
XRD	X-Ray Diffraction
ZOLZ	Zero Order Laue Zone

LIST OF SYMBOLS

a_H	Bohr Radius
a_{Bohr}	Bohr Radius
a_j	Fitting Parameter
A	Coefficient
b	Vector
b_j	Fitting Parameter
B	Coefficient
B	Vector
c	Speed of Light
C	Speed of Light
C_c	Chromatic Aberration Coefficient
C_s	Spherical Aberration Coefficient
d	Distance
D	Diameter

df	Depth of Focus
e	Electron
eV	Electron Volt
f	Atomic Scattering Factor
F	Fraction of Intensity per nm
h	Planck Constant
ħ	Reduced Planck Constant or Dirac Constant
I	Intensity
I_0	Intensity of the Zero-Loss Peak
I_{max}	Maximum Intensity
I_T	Total Integrated Intensity
J_{2T}	Relative Intensity at a Thickness of 2T
J_T	Maximum Relative Intensity
k	Integer
l	Mean Free Inelastic Path
K	Kelvin, Constant

L	Ratio of $(J_T)^2/J_{2T}$
m_0	Rest Mass
M_0	Rest Mass
n_k	Integer
N_A	Avogadro's Number
r	Correlation Coefficient
r	Vector
R	Correlation Coefficient, Shielding Radius
S_i	Deviation for the i^{th} Fringe
t	Thickness
T	Temperature, Thickness
U	Potential
V	Volume, Voltage
V_0	Accelerating Voltage
W_{at}	Atomic Mass
y	Intercept

Z	Atomic Number
ΔD	Differential Diameter
ΔV	Differential Volume
α	Coefficient, or Convergence Semi-Angle, Tilt Angle
γ	Angle, Relativistic correction
ε	Initial Slope of Wedge Shaped Sample in per nm
ε_0	Vacuum Permittivity
ξ_g	Extinction Distance
μ	Absorption Coefficient, Reciprocal Mean Free Inelastic Path
θ	Braggs Angle
Θ	Half of the Scattering Angle
λ	Wavelength
λ_p	Mean Free Path
π	Mathematical Constant (Ratio of a Circle's Circumference to its Diameter)
σ	Interaction Cross Section

Θ_{max}	Half of the Outer Radius of the Detector
Θ_{min}	Half of the Inner Radius of the Detector

1. INTRODUCTION

With many new techniques [1] developing for nanomaterials [2-4] processing there is an increasing demand for improved characterization techniques. Some techniques are capable of structural (X-ray diffraction, XRD) [5] or compositional analysis of nanomaterials (Energy-dispersive X-ray spectroscopy, EDX), others provide information on chemical bonds [6] (high-resolution electron energy-loss spectroscopy, EELS [7], X-ray Absorption Near Edge Structure, XANES, Extended X-ray absorption fine structure, EXAFS). One important aspect to tailor properties is the knowledge of size, arrangement, and shape of nanomaterials. In Transmission Electron Microscopy (TEM) [8-10] nanomaterials are imaged in projection, and therefore two dimensions can be directly measured using conventional High-Resolution Transmission Electron Microscopy (HRTEM) [11] or Scanning Transmission Electron Microscopy (STEM). Atomic Force Microscopy (AFM) [12] offers height information in nanomaterials while the lateral extent of nanoparticles can only be estimated if the shape of the tip is known. While AFM and TEM provide information on individual nanoparticles, X-Ray Diffraction (XRD) provides a method to obtain information on particle size and size distribution by averaging the scattering contributions of a large number of nanoparticles. However, apart from Atom-Probe Field Ion Microscopy (AP-FIM), where individual nanoparticle sizes can be measured in all three dimensions if they are embedded in a matrix, a three-dimensional (3-D) characterization of nanoparticles has only been recently accomplished [13, 14] in TEM. Nevertheless, 3-D characterization of large numbers of

individual NPs is highly desired in the research community. The thicknesses of nanoparticles, and their volumes and surface areas are quantities, which can only be obtained through a measurement of all three dimensions of the objects. In order to obtain this information, a simple and fast method to directly measure these three-dimensional parameters is presented here.

Transmission Electron Microscopy (TEM) techniques like Tilt Series, Convergent-Beam Electron Diffraction (CBED), EELS (electron energy-loss spectroscopy) / Energy Filtered Transmission Electron Microscopy (EFTEM) [15, 16] Thickness Maps [17], etc., seem plausible candidates to accomplish this. However, by looking at these methods carefully, the limitations of each method in accomplishing this task become clear. These will be discussed in following sections.

In this dissertation the High-Angle Annular Dark-Field Scanning Transmission Electron Microscopy (HAADF-STEM) method [18-28] will be evaluated as a method to obtain quantitative 3-D information on individual nanoparticles because it is predominantly based on incoherent elastic scattering between electrons and atoms, thus reducing the typical multiple scattering effects found in transmission electron microscopy. With appropriate calibration HAADF-STEM will reveal the third dimension of each nanoparticle and thus yield thickness information. More importantly, this dissertation will address the capability of HAADF-STEM to obtain statistically relevant data on particle volume distributions, particle shapes, and compositions from binary alloys for TEM samples of known thickness.

Standard methods to determine all three dimensions of individual nanoparticles or nanomaterials are described in the chapters below, followed by an overview of the HAADF-STEM method as used in this work:

- Bright- and dark-field imaging in TEM provide no or only limited information on the vertical sizes of nanoparticles.

- Tilt-series imaging for 3D characterization of samples in TEM is widely used in biology, but has limitations for imaging of crystalline materials.

- Atomic Force Microscopy (AFM) provides excellent means to determine heights of nanoparticles on the surface substrates.

- Atom Probe Field Ion Microscopy (APFIM) is a useful tool to quantitatively characterize nanoparticles embedded in a matrix.

- Convergent-Beam Electron Diffraction (CBED) gives useful thickness information for TEM samples containing large crystalline grains.

- Thickness maps in Energy-Filtered Transmission Electron Microscopy (EFTEM) are only useful if inelastic scattering parameters are known. Without calibration for each crystal orientation, they give only relative thickness information.

1.1. 2-D TEM Approach

In TEM, the 2-D image is the projection of 3-D object. There is no thickness information in the 2-D image. In other words, some objects can produce the same 2-D image which gives us a hard time to interpret the object.

In TEM, information is either averaged through the thickness of the specimen or it is a complicated non-linear function of scattering contributions of all atoms along the beam direction. In other words, a single TEM image has no simple depth sensitivity. Thicknesses and volumes of objects cannot be determined from a single projected (2-D) TEM image. One example is contrast oscillations for wedge shaped samples in two-beam imaging or weak-beam imaging [29].

1.2. Tilt Series Approach

A tilt series [30-35] is a sequence of TEM images of the same object projected in different directions, see Figure 1. First of all, the object is imaged at no sample tilt (0°). In this example the sample object is then imaged at every + / - 5° tilt of the TEM sample holder. Often, even smaller tilt angle intervals are used. Tilt series imaging has a long history in biological transmission electron microscopy [36]. An example of 3-D tilt series of Silicon is shown in Figure1. In biological TEM tilt series are often performed at cryo-temperatures and at low electron doses to minimize radiation damage.

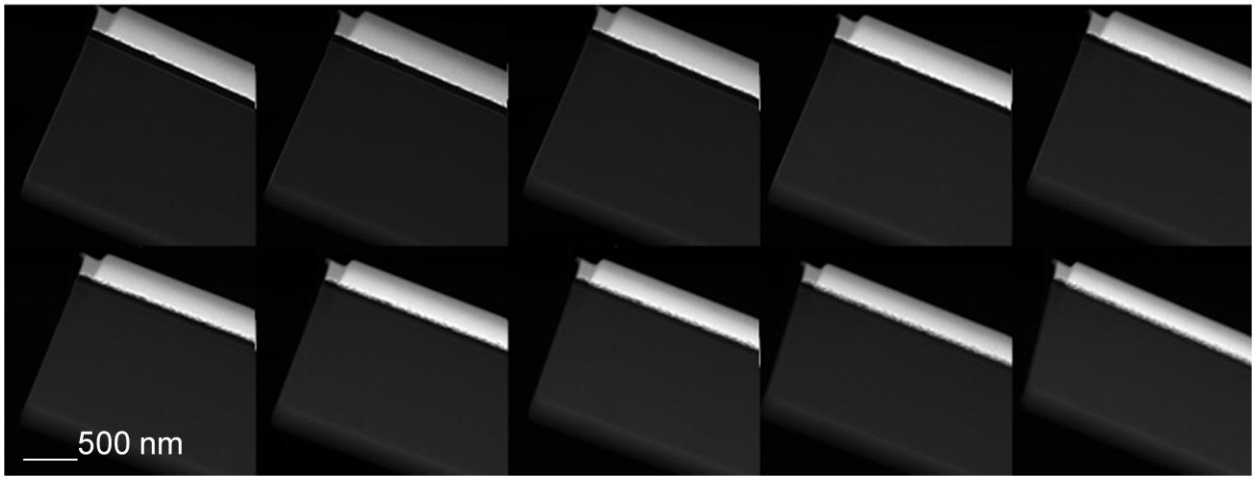

Figure 1: Tilt series of silicon. From top left to top right, 5, 10, 15, 20 and 25 degrees tilt. From lower left to lower right, 30, 35, 40, 45 and 50 degrees tilt.

However, in materials science 3-D TEM has rarely been used to study the shape and volume of nanomaterials. For conventional HRTEM the main reason is the image formation which is highly influenced by multiple scattering. Through tilting the imaging conditions change drastically for crystalline materials. In BF imaging the material appears dark when the Bragg condition is fulfilled, while the same material appears significantly brighter if the sample is tilted away from any Bragg condition. For high-resolution TEM of crystalline nanomaterials, the second reason for the rare use of a three-dimensional analysis is the lack of a high number of suited crystallographic orientations for HRTEM. Only a few low-indexed beam directions can be used in HRTEM for lattice or atomic column imaging. The resolution in HRTEM is limited by the point resolution and the information limit, thus only a few low-indexed lattice plane spacing can be resolved. The point resolution of a typical transmission electron microscope operated at 300 kV as the Tecnai F30 used in this work is about 0.2 nm.

For a face-centered cubic material like aluminum, only {111} and {200} lattice planes can be imaged without image reconstruction methods, thus limiting high-resolution lattice plane images to the 12 <110> and 6 <100> beam directions. Considering typical tilt capabilities of a sample holder in a transmission electron microscope in the range of about 40 degrees in any direction, one or two (in rare cases three) orientations are reachable through sample tilting for high-resolution imaging.

The limited resolution in conventional HRTEM can now be overcome by corrector systems for the spherical aberration C_s of the objective lens, providing a point resolution in the 0.1 nm range. This now makes imaging of crystalline materials along a large number of crystallographic directions possible. With these systems, additionally {220} and {311} lattice planes can be directly imaged. This provides a larger number of possible sample orientations for 3D high-resolution TEM: The directions <100>, <110>, <111>, <211>, <310> amount to 74 possible beam orientations in 4π. This increases the number of available orientations for high-resolution imaging of a single grain to over 10. However, the problem with multiple scattering remains, which renders image interpretation difficult.

The drawbacks of this tilt series approach are related to unstable samples which are subject to radiation damage, as well as the missing cone information [37]. The object may move on a supporting film during tilting, or the support itself can deform due to radiation damage and local temperature changes during electron exposure. The specimen may be damaged during long time exposure to the electron beam, and the

cone information is missing. Recently, tilt series have been obtained with high-resolution STEM. Van Aert et al. [13] have successfully performed a 3-D analysis of several Ag-nanoclusters embedded coherently in an Al matrix using HAADF-STEM with a C_s corrected system for the electron probe forming (upper) part of the objective lens. They were able to determine the distribution of silver atoms from a few projections. However, they point out that there may be several solutions for the reconstruction of the Ag distribution from the micrographs. This ambiguity of possible solutions is an inherent problem of discrete atomic tomography, as long as the number of projections is lower than the number of atoms in an atomic column.

1.3. AFM Approach

Atomic Force Microscopy provides very precise height (thickness) information, as a tip on a cantilever scans across a surface as seen in Figure 2. However, its lateral information is in some cases (for example at high steps and at the edges of nanoparticles) not as reliable as that of TEM because AFM has a better height resolution than lateral resolution. One might consider to use TEM and AFM together and to get lateral information from TEM and height (thickness) information from AFM. Unfortunately, it is not easy that the same object can be found easily in both the TEM and the AFM.

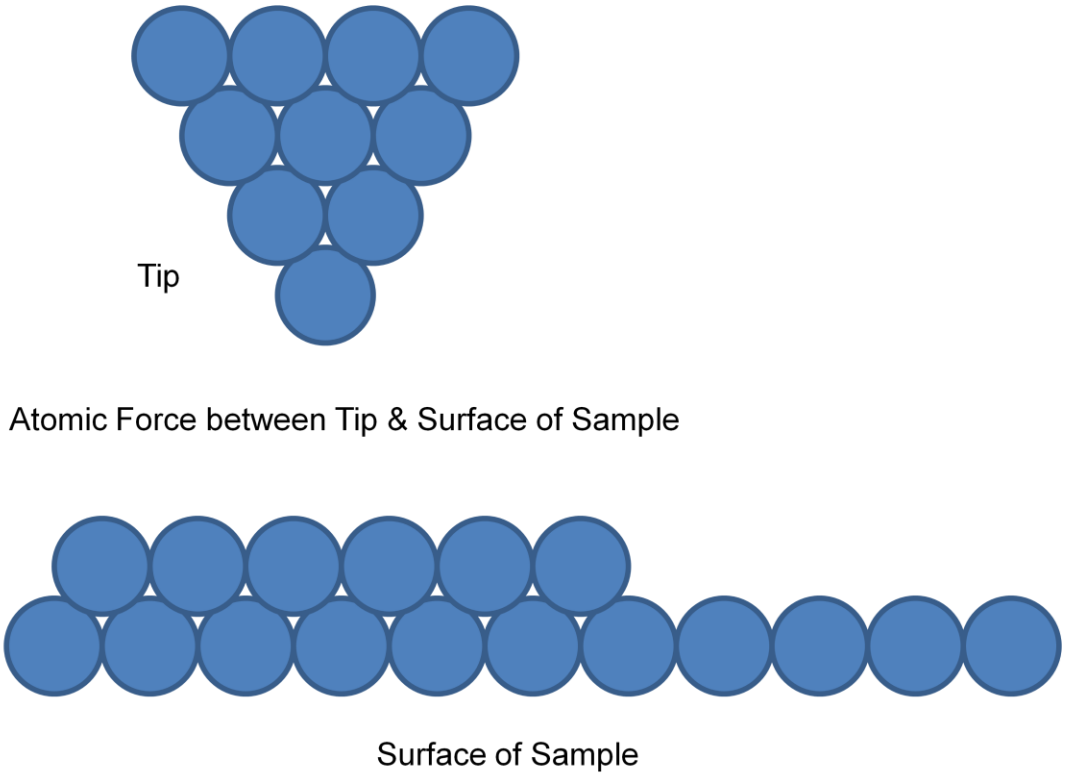

Figure 2: Schematic of Atomic Force Microscopy (AFM).

1.4. Atom-Probe Field Ion Microscopy

The AP-FIM technique provides a true 3-D method for the characterization of nanomaterials embedded in a matrix. The principle of the Tomographic Atom Probe is described in the following schematic (Figure 3). A sharp needle with a few 10 nm diameter of a material is produced by chemical, electrochemical etching, and inserted as an anode in the FIM system. Either by applying an electrical pulse (for electrically conductive materials) or by applying a short laser pulse “atoms are removed from the surface of the” tip and recorded using a position sensitive detector. The atoms typically

have a trajectory which starts perpendicular to the local surface. With the position sensitive detector in combination of a Time-Of-Flight (TOF) method [38], the original location of the atom in the sample and the atomic species of (each) atom can be determined, thus yielding true 3-D chemical information. However, the AP-FIM method does not provide true 3-D atomic resolution of the location of each atom. Specifically, the depth resolution is good enough to provide atomic imaging, while the lateral identification of the original atomic position is less accurate. Additionally, not all atoms are detected in the process.

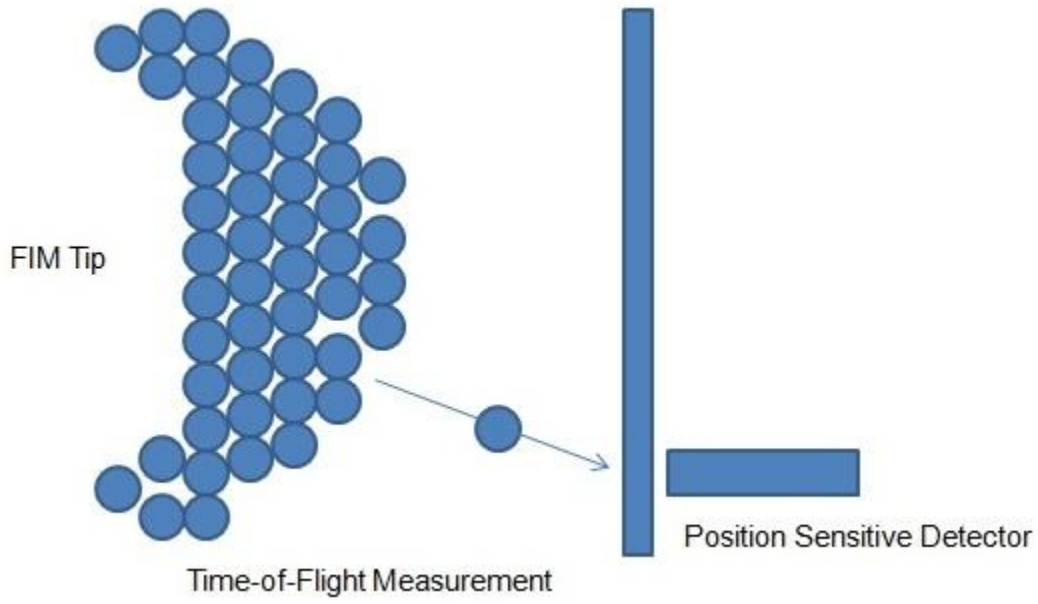

Figure 3: Schematic of Atom-Probe Field Ion Microscopy.

1.5. CBED Approach

In TEM convergent Beam Electron Diffraction (CBED) has long been used to determine the thickness of a specimen. Kossel-Möllenstedt (K-M) fringes [18] in a ZOLZ (zero order Laue zone) CBED pattern have to be obtained in the diffraction mode of TEM, see Figure 4.

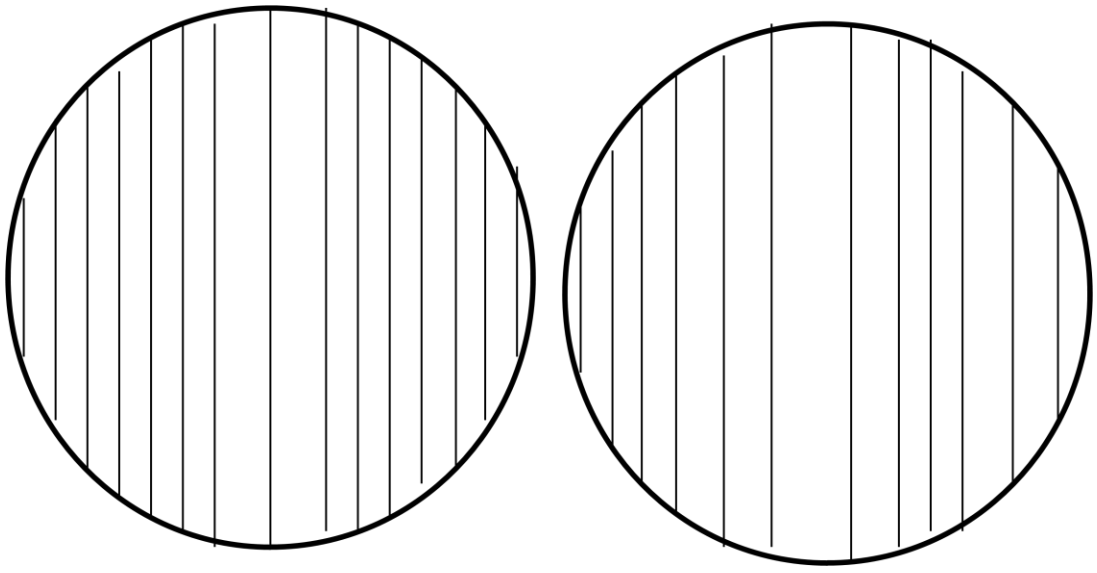

Figure 4: Schematic of Kossel-Möllenstedt fringes in a ZOLZ CBED pattern.

Kossel-Möllenstedt “fringes are commonly employed to measure the crystal thickness” as “they form a pattern that changes steadily with specimen thickness”. The thickness can be determined by comparing experimental diffraction patterns with simulated ones [18]. But for materials with known scattering strengths it can also be determined mathematically [18]. However, this method is limited only to single crystals.

For poly crystals or amorphous [39-42] nano sized objects, K-M fringe patterns cannot be obtained. If the extinction distance ξ_g is known, the thickness t can be determined by the following equation [18]:

$$\frac{S_i^2}{n_k^2} + \frac{1}{\zeta_g^2 n_k^2} = \frac{1}{t^2} \quad (1)$$

where n_k is a integer (k is an integer not related to λ), s_i is the deviation for the i^{th} fringe. If ξ_g is not known, a graphical method can be used to find the value of t [18].

1.6. EELS / Thickness Map Approach

If the specimen "is thin enough to ensure that only a single Plasmon peak is excited", Electron Energy-Loss Spectroscopy (EELS) methods can be used to obtain thickness maps [43, 44]. In this approach an image forming system is required after the energy filter. The most common instrumental options are a post-column Gatan Imaging Filter or the in-column Omega filter used in the Energy Filtered mode of TEM (EFTEM) to determine the thickness of the specimen. In both cases an energy selecting slit is introduced in the energy filter to obtain an image with zero loss electrons (electrons which suffered no energy loss or only phonon interactions) in the sample. This image is compared with an image formed without the energy selecting slit. In this latter case all transmitted electrons are collected. The ratio of these two intensities is determined for each pixel in the images (if there is no sample drift, otherwise, a correction through cross correlations is done to match the pixel positions). The thickness can be determined by the following equation [45]:

$$t = \lambda_p \ln \frac{I_T}{I_0} \tag{2}$$

Where: λ_p is the mean free path of the electron; "I_T is the total integrated intensity that includes the Plasmon and zero-loss peaks; and" I_0 denotes "the intensity of the zero-loss peak alone". A schematic EELS spectrum is shown in Figure 5.

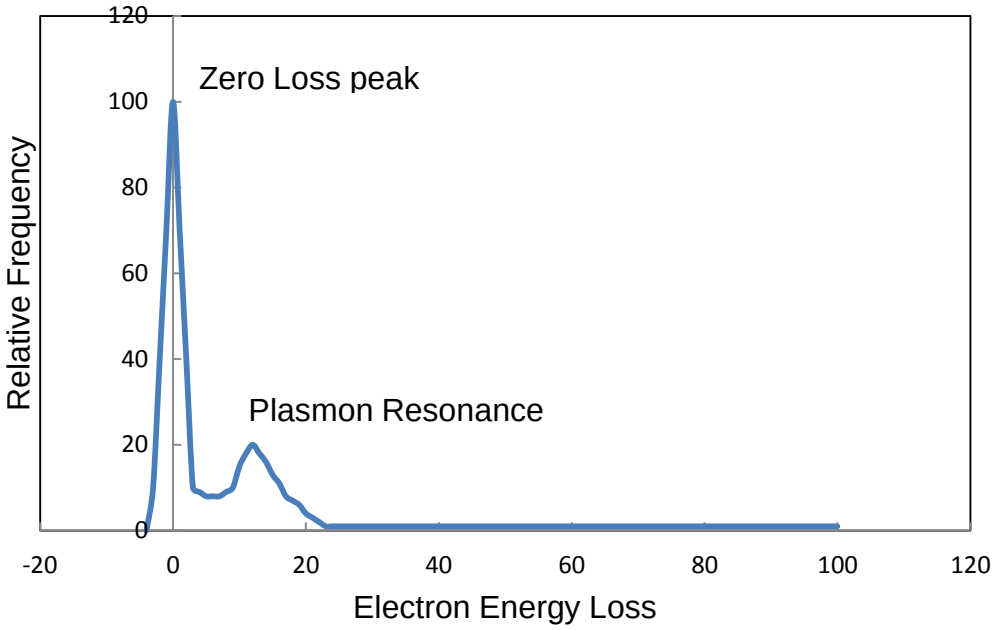

Figure 5: Idealized schematic of an EELS spectrum indicating Zero Loss peak, and Plasmon resonance.

The detailed equations to determine the specimen thickness are given in Brent Fultz and James Howe's textbook [46]. The problem is that the mean free inelastic path $l = 1 / \mu$ of the electrons has to be known for each specific material and crystal

orientation before the thickness can be obtained from EFTEM map or the EELS spectrum. Although there is a semi-empirical equation for the mean free inelastic path, its orientation dependence is not taken into account. Experimental values for the mean free inelastic path indeed show strong orientation dependence [47].

2. HIGH ANGLE ANNULAR DARK FIELD (HAADF) APPROACH

2.1. Theory and Experiment

Many transmission electron microscopes offer the option of scanning a small electron probe across a sample. Several detectors can be used to measure certain quantities for each scanning position. One measurable quantity is an Electron Energy-Loss Spectrometers, EELS, spectrum which can be acquired by sending the transmitted electron beam into an electron energy filter. A similar analytical option is Energy-Dispersive X-ray spectroscopy (EDX) to measure the energies of element-specific X-rays emitted from the sample for each scan position needed for EELS and EDX. Both EDX-STEM and EELS-STEM can yield chemical information with high lateral resolution. However, the acquisition time for each electron probe position is typically in the range of several seconds to obtain a spectrum with reasonable signal-to-noise ratio. If an area is scanned comprising even only 100 X 100 pixels, the acquisition times for EDX or EELS maps in STEM are in the range of several hours or even several 10 hours. This severely limits the application of STEM maps with EDX or EELS as costs for the user time of the instrument becomes high, and as sample drift corrections have to be maintained throughout the acquisition. Only few examples for high-quality elemental maps obtained from EELS-STEM or EDX-SEM are known.

More commonly used are detectors which measure intensities of the transmitted electron beams for each position. These detectors are always placed in a diffraction

plane of the sample. This is best accomplished by using the “transmission electron microscope in the diffraction mode” with the diffraction pattern being in focus at the location of the STEM detectors. Most STEM systems are equipped with three electron detectors, a Bright Field (BF) detector, a Dark Field (DF) detector, and a High Angle Annular Dark Field (HAADF) detector. The BF and DF detectors are usually positioned off axis in TEM / STEM systems. The electron beam is deflected in the projector system away from the optical axis when these STEM detectors are used. If these two STEM detectors were on the optical axis, they would block the electron path to other detectors like a CCD [48] camera in TEM mode or a post-column energy Filter. A HAADF detector can typically be retracted from the on-axis position to allow normal TEM operation. In most cases the HAADF detector cannot be simultaneously used with the BF and the DF detector as they are at different locations in a transmission electron microscope with respect to the optical axis.

For small camera lengths used in the diffraction mode the HAADF detector only collects electrons scattered to high angles (> 50 mrad) and does not interact with the low angle electrons. Therefore, the HAADF detector can be used together with a post column electron energy loss spectrometer which lets only electrons of no or small scattering angle into its entrance aperture.

Incoherent elastic scattering of electrons is responsible for a signal which can be collected by a HAADF detector in TEM. In principle, the simplified intensity (I)

expression in terms of specimen thickness (*t*) and atomic number (*Z*) is as following for electrons scattered to high angles:

$$I \propto tZ^{\alpha} I_{incident} \quad (3)$$

where: α is a fitting parameter, with $1 < \alpha < 2$ [18]. For large scattering angles the electrons are scattered predominantly by the electrostatic potential of the nucleus of each atom. This is the case of Rutherford scattering for which the exponent α is expected to be 2. However, the incident electrons also experience scattering by the potential caused by the electronic shell of each atom. This specially extended shell partially shields the electrostatic potential of the nucleus and reduces the exponent α. However, it should be noted here that this shielding differs from atomic species to species. Therefore, the approach from Equation 3 is only a first approximation for the HAADF intensity showing an overall trend for all elements. Similarly, the proportionality of the intensity with the thickness in Equation 3 is only valid if multiple scattering is negligible. Furthermore, this approach is only valid for thin samples where the vast majority is not scattered to higher angles. Obviously, Equation 3 becomes useless if the HAADF-STEM intensity approaches in this equation (or exceeds) the incident beam intensity with increasing sample thickness. Additional corrections are required for thick samples.

The experimental setup is shown in Figure 6. In STEM mode, an electron beam scans across a rectangular (or square) area of the specimen. The “HAADF detector

collects electrons scattered to" high angles defined by the camera length used, and those electrons are used to determine the image intensity for each scan position. TEM is operating in different mode. So the diffraction pattern is projected onto the plane of the HAADF detector [49].

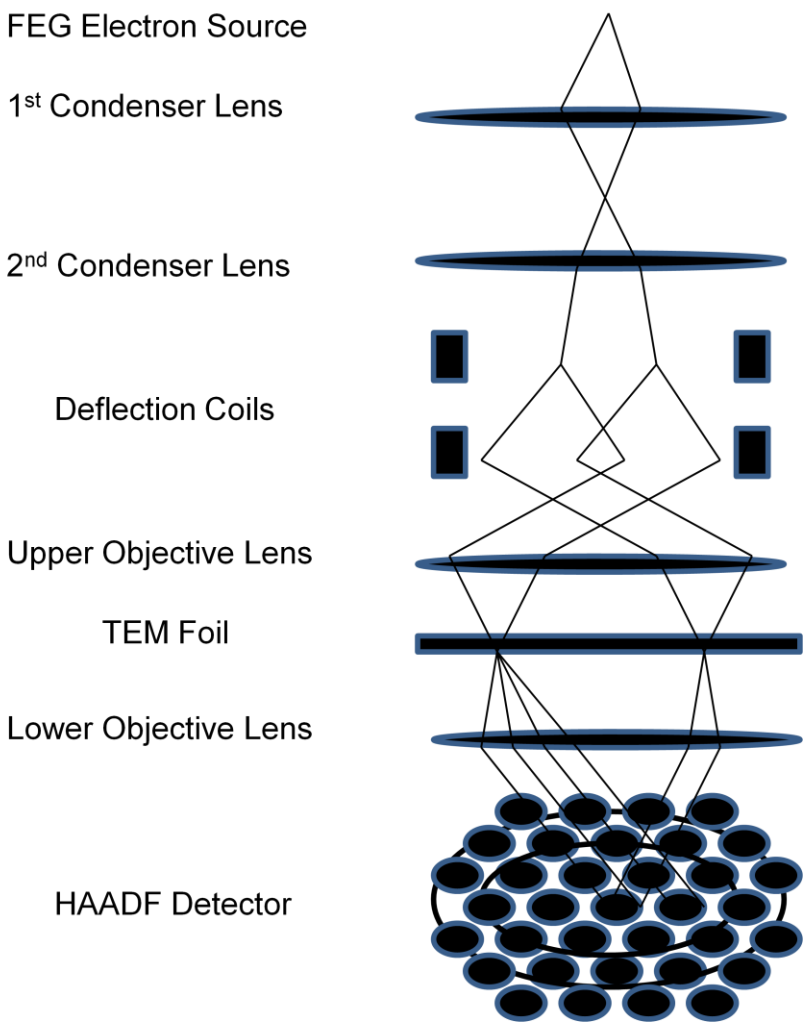

Figure 6: Schematic of the HAADF-STEM setup.

2.2. Work Done by Others

Since the development of scanning transmission electron microscopy in the 1970s and the wide-spread use of high-angle annular dark field detectors starting in the 1990s a vast of number of papers on the use of the HAADF-STEM technique has been published. Max Otten [50] described how to determine proper microscope parameters in transmission electron microscopes. Liu and Cowley [51] describe the image formation process in HAADF-STEM and show that atomic number contrast (Z-contrast) can be obtained. They also show that high-resolution imaging is possible with HAADF-STEM. Most applications of the HAADF-STEM technique are making use of this atomic number contrast to image chemical heterogeneities in materials. This Z-contrast method is uniquely suited for nanoscale imaging of compositional differences. However, as the Z-contrast method only provides a grayscale contrast, compositional analysis is not possible with HAADF-STEM, except for some binary systems as outlined in an example of Fe and Pt multilayers described further below in this dissertation. Most HAADF-STEM applications are exclusively devoted to qualitative imaging and on identification of sample areas for further quantitative chemical analysis using Energy Dispersive X-ray Spectroscopy or Electron Energy Loss Spectroscopy. In the following literature overview I want to focus on research presented on the quantitative characterization of HAADF-STEM micrographs.

One issue for the quantitative interpretation of HAADF-STEM images is the contribution of quasi-elastic scattering, often referred to as thermal diffuse scattering

(TDS), to the HAADF-STEM signal. According to Liu and Cowley [51] thermal diffuse scattering is the main contribution to the signal at high scattering angles. Therefore, incoherent scattering is the major part of the signal allowing for the use of eq. 3 for the thickness dependence of the HAADF-STEM signal (at least for thin samples where absorption is negligible).

The thermal contributions to the HAADF-STEM signal were the main focus of research for Dr. Rumyana Petrova [52] in her dissertation at UCF. She studied the HAADF-STEM intensity (I) as a function of temperature (T), specimen thickness (t), beam position, and beam convergence semi-angle (α), i.e., I = f(T, t, α), where: T = 100 K, 300 K; $t \leq 160$ nm; for on- or off-column positions; α = 4 mrad, 7 mrad, 20 mrad; for Si (Z = 14), **B** = <110>, with multislice frozen phonon simulations. She found a quantitative agreement between experimental data and simulations on the dependence of the high-angle scattering of 300 keV electrons on thickness at two different temperatures, 100 K and 300 K [52]. Dr. Kirkland [53, 54] has done extensive computational work in electron microscopy and provided software which was used, among others, by Dr. Petrova [52]. This software is based on the multislice algorighm and was used in the work presented here.

The aspect of coherent scattering versus incoherent scattering was studied by Dr. Findlay et al. [55]. They have studied “atomic number contrast in HAADF imaging of crystals”. They presented quantitative comparison between experimental and simulated “HAADF images of $SrTiO_3$, $PbTiO_3$, InP and $In_{0.53}Ga_{0.47}As$ in the” STEM. They found

significant discrepancies “in the signal to background ratios”. They pointed out that for “these strongly scattering samples, spatial incoherence and instabilities cannot account for the bulk of this discrepancy, as they could in previous explorations on silicon”. However, they discussed “where additional experiments and theoretical studies are needed for developing a quantitative understanding of HAADF image contrast”.

Quantitative HAADF-STEM research is an increasingly active area as new capabilities for high-resolution STEM become more and more available with the introduction of C_s-corrected microscopes. Several papers describe methods for quantitative analysis of HAADF-STEM micrographs, mostly for high-resolution imaging like Findley et al. [55].

Only few authors have reported quantification of low-resolution HAADF-STEM micrographs, for example Haritha Nukala [56] has done partial work on this project without simulations. She found that the “local thickness of nanoparticles can be measured which in principle gives us the volume of the nanoparticles.” Low-resolution HAADF-STEM can be quantitatively used to determine thicknesses or to determine compositions of binary systems as described in the following.

The important aspect of thickness determination in HAADF-STEM was studied in detail by V. Jantou-Morris et al. [57]. They studied the nano-morphological relationships between apatite crystals and collagen fibrils in ivory dentine. They have used a combination of HAADF-STEM imaging and EELS analysis for simultaneous acquisition of both spatial and spectral information pixel by pixel (spectrum imaging). They have

measured the relative thickness, t/λ, thickness/mean free path, of samples using EELS. They calculated the mean free path with some approximations. The uncertainty in their values is estimated to be about ±20%.

Low-resolution HAADF-STEM was also used to determine compositions of binary materials. D. Araújo et al. [58] determined the local boron doping levels in homoepitaxial diamond structures. They have demonstrated the capability of STEM using HAADF to quantify the boron concentration in the high doping range between 10^{19} cm^{-3} and 10^{21} cm^{-3}. Due to the large relative variation of atomic number Z between carbon and boron, doping concentration maps and profiles were obtained with a nanometer-scale resolution. They developed a novel numerical simulation procedure for concentration quantification of boron and demonstrated the high sensitivity and spatial resolution of this technique.

Most of the literature available on quantitative HAADF-STEM is focused on high-resolution imaging with atomic-column quantification in combination with contrast simulations [59]. A short description of these analyses is given below. For many materials atomic column resolution is not always possible due to limits in instrument resolution and inappropriate sample orientations, especially in the case of nanoparticles on a surface. The goal of the dissertation presented here is to develop quantitative methods of low-resolution HAADF-STEM which allow for reliable and fast measurements of particle size distributions. It is not the goal to improve the methods

developed in high-resolution HAADF-STEM as described below, rather to learn from the possible problems and opportunities the authors have outlined.

Dr. Rolf Erni et al. [59, 60] performed quantitative characterization of chemical in-homogeneities in Al-Ag using high-resolution Z-contrast STEM. They have applied the incoherent imaging model to interpret high-resolution Z-contrast micrographs. They developed a simple method for a column-by-column resolved characterization of Ag-rich precipitates in Al-Ag. This method needs no information on the details of the imaging process. Evaluating the high-angle scattering intensities of Al and Ag by image analysis, the number of Ag atoms contained in individual atomic columns was determined accurately and moreover, the thickness of the thin foil was calculated. Multislice simulations have confirmed the broad validity of the incoherent imaging model for Z-contrast STEM and were used to check the method. They have also applied the image analysis to experimental Z-contrast images of Guinier-Preston zones in Al-3 at% Ag. The Ag content of individual atomic columns was determined with an accuracy better than ±10%.

One approach to compare experimental data with models is the use of a well-known material. This is especially important for HAADF-STEM imaging to distinguish artifacts of the image forming process from the relevant contributions of the sample. Electron channeling, focus values, lens aberrations, beam size, beam convergence and beam shape, as well as contrast-brightness settings are important parameters to be considered for the imaging process. Yasutoshi Kotaka [61, 62] systematically

investigated the accuracy of quantitative analysis for Z-contrast images with a spherical aberration (C_s) corrected HAADF-STEM using $SrTiO_3$ (001). Atomic column and background intensities were measured accurately from the experimental HAADF-STEM images obtained under exact experimental condition. He examined atomic intensity ratio dependence on experimental conditions such as defocus, convergent semi-angles, specimen thicknesses and digitalized STEM image acquisition system brightness and contrast. He pointed out that quantitative analysis of C_s-corrected HAADF-STEM requires knowledge of the exact defocus to measure specimen thickness and to fix setting of brightness, contrast and probe current. To confirm the validity and accuracy of the experimental results, he compared experimental and HAADF-STEM calculations based on the Bloch wave method.

Koji Kuramochi et al. [63] have worked on the effect of the chromatic aberration (C_c) coefficient in a spherical aberration (C_s)-corrected electromagnetic lens on HAADF-STEM. They have demonstrated a new method for precise determination of the C_c coefficient, requiring measurement of an atomic-resolution one-frame through-focal HAADF STEM image. They found that the method is robust with respect to instrumental drift, sample thickness, all lens parameters except C_c, and experimental noise. They have also demonstrated that semi-quantitative structural analysis on the nanometer scale can be achieved by comparing experimental C_s-corrected HAADF STEM images with their corresponding simulated images when the effects of C_c coefficient and spatial incoherence are included.

With the knowledge of imaging parameters and appropriate image simulations, a quantitative interpretation of high-resolution HAADF-STEM images of thin samples becomes possible. One example is shown by D. Araújoa et al. [64], who have studied InAs/GaAs quantum dot morphologies combined with nanometric scale HAADF simulations. They have presented a quantitative methodology of measuring the In distribution in nominal InAs/GaAs individual quantum dots (QDs). They performed numerical simulations using the multislice-based approach, allowing predicting HAADF micrograph contrast in the STEM mode. This method is adapted for nanometric scale; it is shown that its high sensitivity can reveal In-segregation in QDs. They were able to show the indium distribution below the wetting layer resulting in an elliptical shape of the observed QDs.

P. M. Voyles et al. [65] have studied atomic-scale imaging of individual dopant atoms and clusters in highly n-type bulk Si by HAADF-STEM. They reported the direct, atomic-resolution observation of individual antimony (Sb) dopant atoms in crystalline Si, and identify the Sb clusters responsible for the saturation of charge carriers.

M. Haruta et al. [66] have studied the effects of electron channeling in HAADF-STEM intensity in La_2CuSnO_6. Unique contrast features make an intuitive interpretation of the HAADF-STEM images in La_2CuSnO_6, a double perovskite oxide, difficult. Multislice simulations confirmed that channeling processes of electrons in combination with the differing Debye-Waller factors for the two independent. Sn atoms and four independent La atoms in the unit cell. Haruta et al. [66] found that the HAADF intensity

did not decrease constantly with the increase in column separation, with the exception of a very thin sample, which could be interpreted by the specific charge in the electron-channeling process.

Z. Yu et al. [67] looked at the effects of specimen tilt in ADF-STEM imaging of a-Si/c-Si interfaces. They found that ADF-STEM imaging of a crystal depends strongly on specimen oritention, but for an amorphous sample it is insensitive to orientation changes. To fully investigate the effects of specimen tilt, an interface of amorphous Si (a-Si) and crystalline Si (c-Si) was rotated systematically off a zone axis in a STEM equipped with low-angle ADF (LAADF) and HAADF detectors. They found that the change of relative intensity across the interface shows very different trends in the LAADF and the HAADF images upon tilting. More importantly, they found that the HAADF signal decreases much more rapidly when tilted off a zone axis than does the LAADF signal. The high-resolution lattice fringes also disappear much faster in the HAADF image than in the LAADF image. They pointed out that these trends reflect the fact that the channelling peaks responsible for additional scattering into the HAADF detector decrease more quickly upon tilting than the lower-angle scattering to the LAADF detector.

Dmitri O. Klenov et al. [68] have analyzed the different contributions to the contrast in experimental HAADF images acquired in STEM. Experimental HAADF images were obtained from a model system consisting of an epitaxial perovskite $PbTiO_3$ film grown on a $SrTiO_3$ single crystal. The main objective of the research was to quantify

the influence of the TEM foil thickness on the image contrast, but the effects of the annular detector inner angle and the probe forming lens focus were also studied. Sample thicknesses ranging from 10 nm to more than 400 nm were investigated. They found that the image contrast was relatively insensitive to changes in inner detector angle. The main impact of sample thickness was a rapid increase in a background intensity that contributed equally to the intensities of the atomic columns and the channels between them. The background intensity and its increase with thickness reflected the average atomic number of the crystal. Subtraction of the background intensity allowed for a quantitative interpretation of the image contrast in terms of atomic numbers and comparison with multislice image simulations. They also discussed the consequences for the analysis of interfaces in terms of atom column occupancies.

Over the last years the Z-contrast method has developed from a simple imaging method to applications of quantitative high-resolution HAADF-STEM where atom counting becomes available for heavy atoms. Laurent D. Menard et al. [69-71] have studied sub-nanometer Au monolayer-protected clusters exhibiting molecular like electronic behavior by quantitative HAADF-STEM. They have characterized these clusters featuring the precise determination of the number of gold atoms in the cluster cores using HAADF-STEM, allowing the assignment of 13 gold atoms (±3 atoms) to the composition of both cluster molecules.

This ‘atom counting’ approach becomes more interesting when it can be combined with three-dimensional analysis. Konrad Jarausch et al. [72] performed three-

dimensional electron microscopy of individual nanopartices. STEM images were captured at regular tilt intervals over a complete 360° rotation to eliminate missing wedge artifacts. Standard tomography techniques were used to reconstruct the 3D structure of the individual nanoparticles from the STEM HAADF tilt series. Dr. Li et al. [73-75] characterized the three-dimensional atomic-scale structure of size-selected gold nanoclusters. A linear relationship between integrated HAADF intensity and size of gold clusters was observed.

J. M. LeBeau et al. [76-81] developed a standard-less atom counting method in HAADF-STEM. They have demonstrated that HAADF-STEM image allows for quantification of number and location of all atoms in a three-dimensional crystalline, arbitrarily shaped specimen without the need for a calibration standard. They have also shown that the method also provides for an approach to directly measure the finite effective source size of a scanning transmission electron microscope.

N. P. Young et al. [82] have determined the mass and 3D shape of nanoparticles on supports, using size selected nanoclusters as mass standards in STEM. Through quantitative image intensity analysis, they have shown that the integrated HAADF intensities of size-selected gold clusters soft-landed on graphite display a monotonic dependence on the cluster size as far as ~6500 atoms. They applied this mass standard to study gold nanoparticles prepared by thermal vapor deposition and by colloidal wet chemistry, and from which they deduced the shapes of these two types of nanoparticles as expected.

While atomic number contrast in STEM is often used to identify heavy atoms in a matrix of lower density material, some work has been done to identify lighter atoms in a matrix of heavy atoms. E. Carlino et al. [83] also used atomic-resolution quantitative composition analysis using HAADF-STEM. A general approach to measure compositions quantitatively with atomic resolution was developed. The distribution of a chemical species in a host matrix was derived and applied to a case study consisting of a layer of Si buried in a GaAs matrix. They have demonstrated a quasilinear dependence of the HAADF image intensity on the concentration of Si in the GaAs matrix by simulation and experiments performed on Si/GaAs. They also compared the results with those obtained by cross-sectional scanning tunneling microscopy on the same specimens.

Compositional differences also affect the distances of atoms in a material. Therefore, V. Grillo et al. [84] studied the influence of static atomic displacements. Due to atomic size effects in alloys with atoms having different covalent or ionic radii, the contrast of atomic resolution HAADF images is affected. They showed quantitatively by simulation and experiments that the static displacement can have a large influence on the Z contrast, depending on the alloy composition and on the STEM specimen thickness. They pointed out that this influence has to be taken into account for quantitative chemistry measurement based on Z-contrast imaging.

Several authors reported on quantitative analysis of non-equilibrium materials: Similar to Erni et al. [59, 60], T. J. Konno et al. [85] have also performed HAADF-STEM

studies on the early stages of precipitation in aged Al-Ag alloys. Konno et al. [85] found irregularly shaped small Ag particles of 1-2 nm which dominate an alloy annealed at 140°C for 10 h. Atomic resolution HAADF-STEM images revealed that Ag atoms tend to form {111} planar clusters. S. J. Pennycook et al. [86-88] have extensively applied Z-contast imaging in STEM. They were able to perform compositional mapping during crystal formation. T. Akita et al. [89] identified the gold catalyst supported on TiO_2 nano-rods by HAADF-STEM/TEM. HAADF-STEM has revealed that Au platelets with thicknesses of (0.5-1) nm form at the interfaces between TiO_2 nano-rods. T. Yamazaki et al. [90] have used quantitative high-resolution HAADF-STEM analysis on boundaries in Sb_2O_3-doped zinc oxide. They have compared the images with the aid of image simulations based on two different modeling techniques.

Image simulations have been an important part of the development of quantitative HAADF-STEM methods. J. Pizarro et al. [91] simulated HAADF-STEM images of large nanostructures. Due to the high computational requirements needed, a parallel software (SICSTEM) was developed. This software can afford HAADF-STEM image simulations of nanostructures composed of several hundred thousand atoms in manageable time. They have demonstrated the usefulness of this tool by simulating a HAADF-STEM image of an InAs nanowire.

Apart from multislice methods [53, 54, 91] Bloch wave methods as presented in [61, 62] can be used for periodic samples. Y. Peng et al. [92] performed a full coherent Bloch wave calculation to invesigate HAADF image formation for sub-angstrom probes

in STEM. They found that with increasing illuminating angle, the contribution of the 1s bound state increases to a maximum at an optimum probe angle, after which they found increasing contributions from high-angle plane-wave states around the periphery of the objective aperture. They found that examination of image contributions from different depths within a crystal shows an oscillatory behavior due to the beating between 1s and non-1s states. The oscillation period reduces with decreasing probe size, while the relative contribution from a specific depth increases. They point out that this signifies a change from a projection mode of imaging to a depth sensitive mode of imaging. They concluded that this new mode appears capable of solving three-dimensional atomic structures in future generation aberration-corrected STEM.

C. J. Rossouw et al. [93] have studied channelling effects in atomic resolution STEM. The Bloch wave theory for incoherent scattering of an incident plane wave proved succesful in prediting the fine detail in 2-D zone axis channelling patterns formed by ADF, BSE and characteristic X-ray detection in beam-rocking mode. By using a previously published example of polarity determination of GaAs by channelling contrast, they have compared experiments with simulations in order to illustrate the applicability of the theory. They also found that a modification of boundary conditions for a focused coherent probe allows lattice-resolution incoherent contrast based on ADF and EELS detection as well as X-ray emissions to be accounted for within a similar theoretical framework. The mixed dynamic form factors constitute an integral part of this theory. They have discussed simulations of lattice-resolution ADF and EELS with reference to various zone axis projections of GaAs. They have also discussed issues of single

versus double channelling conditions, and local versus non-local interactions in relation to X-ray, ADF and EELS.

New developments in electron lenses include corrector systems for spherical aberration. This provides a significantly increased resolution through a smaller electron probe size. O.L. Krivanek et al. [94] reported on the prospects for reaching sub-Å electron probes through aberration correction in the STEM. They have discussed the design, results and practical experience gained from a working 100 keV STEM C_s corrector. They have outlined the design of a second-generation quadrupole-octupole C_s corrector that pays particular attention to the influence of instabilities. Probe shapes calculated for the new corrector system indicate that it will be able to produce a probe smaller than 1 Å at 100 keV.

N. D. Browning et al. [95] pointed out that recent developments in STEM now make it routinely possible to obtain direct images and spectra from interface and defects structures with atomic spatial resolution. They describe the experimental conditions required to set-up and align a 200 kV STEM/TEM microscope to perform this analysis. The various imaging and analysis techniques have been illustrated with examples from interfaces in II-VI and III-V quantum dot system and dislocation cores in GaN.

While most developments for quantitative HAADF-STEM imaging are in the area of high-resolution, the work presented here is focused on low-resolution (no atomic resolution imaging) HAADF-STEM. Especially, the work presented here aims to extend the range of sample thicknesses useful for quantitative HAADF-STEM to well above 100

nm and to use calibration methods to measure nanoparticle volumes even when the sample orientation does not allow for atomic resolution imaging.

3. RESULTS AND DISCUSSIONS

The goal of this work is to measure thicknesses and volumes of nanoparticles. Necessary relative and absolute intensity calibrations are done, and their limitations are outlined. In this section I discuss the reliability of different methods of contrast calibrations. Important aspects of HAADF-STEM contrast are explained in this section, including interfacial features that are important in the understanding of contrast interpretation even for qualitative HAADF-STEM work. Some multislice simulations were performed and described here with special emphasis on limits of this method for thick samples. This work shows that calibrated contrast settings can be used for quantitative measurements of nanoparticle volumes.

3.1. Intensity Calibrations

3.1.1. HAADF-Detector Calibration

The HAADF-STEM detector offers a large range of contrast and brightness (CB) settings. Depending on the samples studied the typical HAADF-STEM user chooses a CB setting which provides the best contrast for the material studied without reaching detector (amplifier) saturation. However, this approach is not used here, as the detector signal will be quantitatively evaluated. The HAADF intensities are calibrated by measuring the HAADF detector intensities when the electron beam is directly (in imaging mode, and not in diffraction mode) scanned across the detector [96]. The sample is retracted when these calibrations are performed and the whole incident

electron probe is scanned across the detector. This procedure is repeated for different electron beam intensities, which are modified by changing (reducing) spot size, condenser aperture size, gun-lens setting, and extraction voltage in the transmission electron microscope. For each electron beam setting the intensity measured by the HAADF detector is compared with the intensity per second measured by the CCD camera for the same electron beam conditions (but in diffraction mode). The HAADF detector shows some variability (about 10%) of its sensitivity depending on where the electron beam hits the detector (Figure 7), and intensities were averaged over the HAADF detector for calibrations.

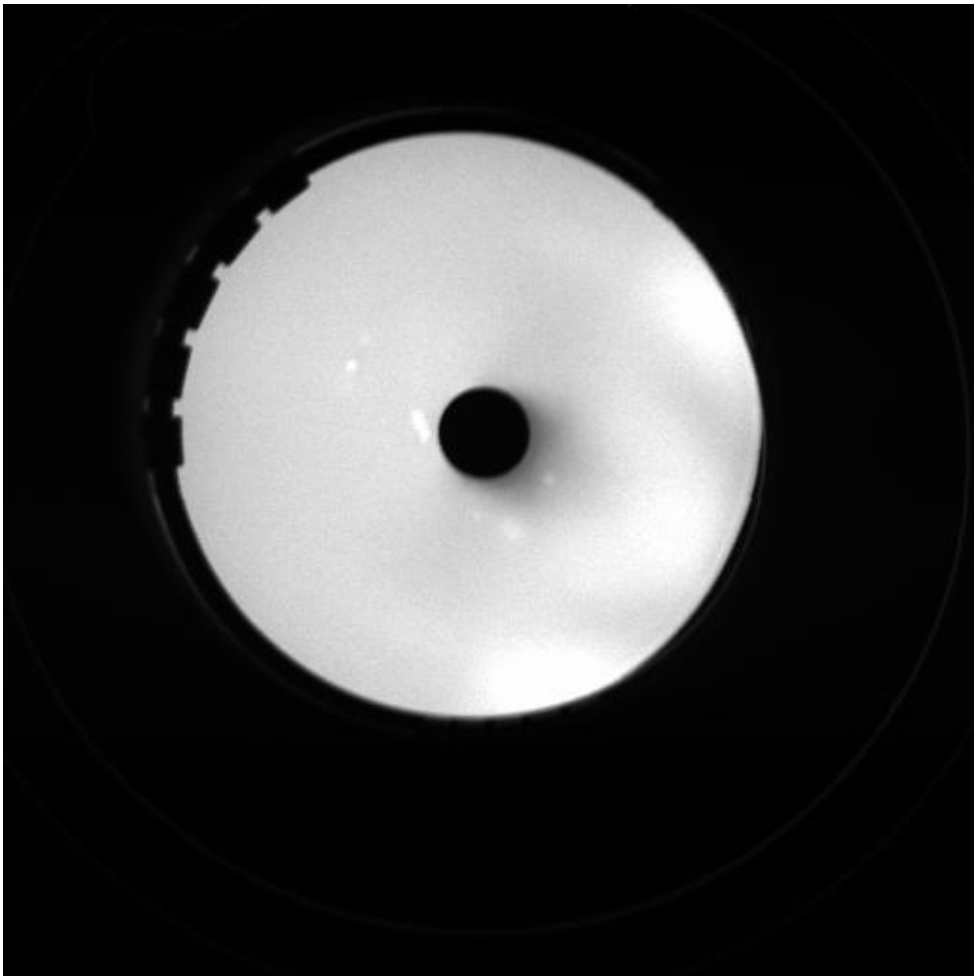

Figure 7: Electron image of the Fischione HAADF detector.

Figure 7 is the electron image of the Fischione HAADF detector in imaging mode of STEM (inner radius for HAADF detector: 53 mrad, outer radius: 230 mrad at 80 mm camera length of TECNAI F30). A specific contrast-brightness setting is chosen in this project (contrast = 12.5%, brightness = 46.875%). When taking an electron image of the HAADF detector and a CCD camera image of the incident beam for different illumination conditions, it was found in this work that the HAADF detector intensity scales with the linear CCD signal and can be best fitted as the following:

$$I_{HAADF} = AI_{CCD}^{B} \quad (4)$$

Where: I_{HAADF} is the intensity of the HAADF detector without background, I_{CCD} is the intensity (per second) of the CCD detector, *A* and *B* are constants.

Linear regression with standard deviation between the HAADF intensity and the CCD intensity is done by the Random Halves approach (Figure 8). The following figure summarizes the data obtained. The CCD intensity shown here is determined from the average intensity on each of the 1024x1024 pixels. For figure 8 the integrated intensity over the CCD camera is shown in units of 10^6 counts.

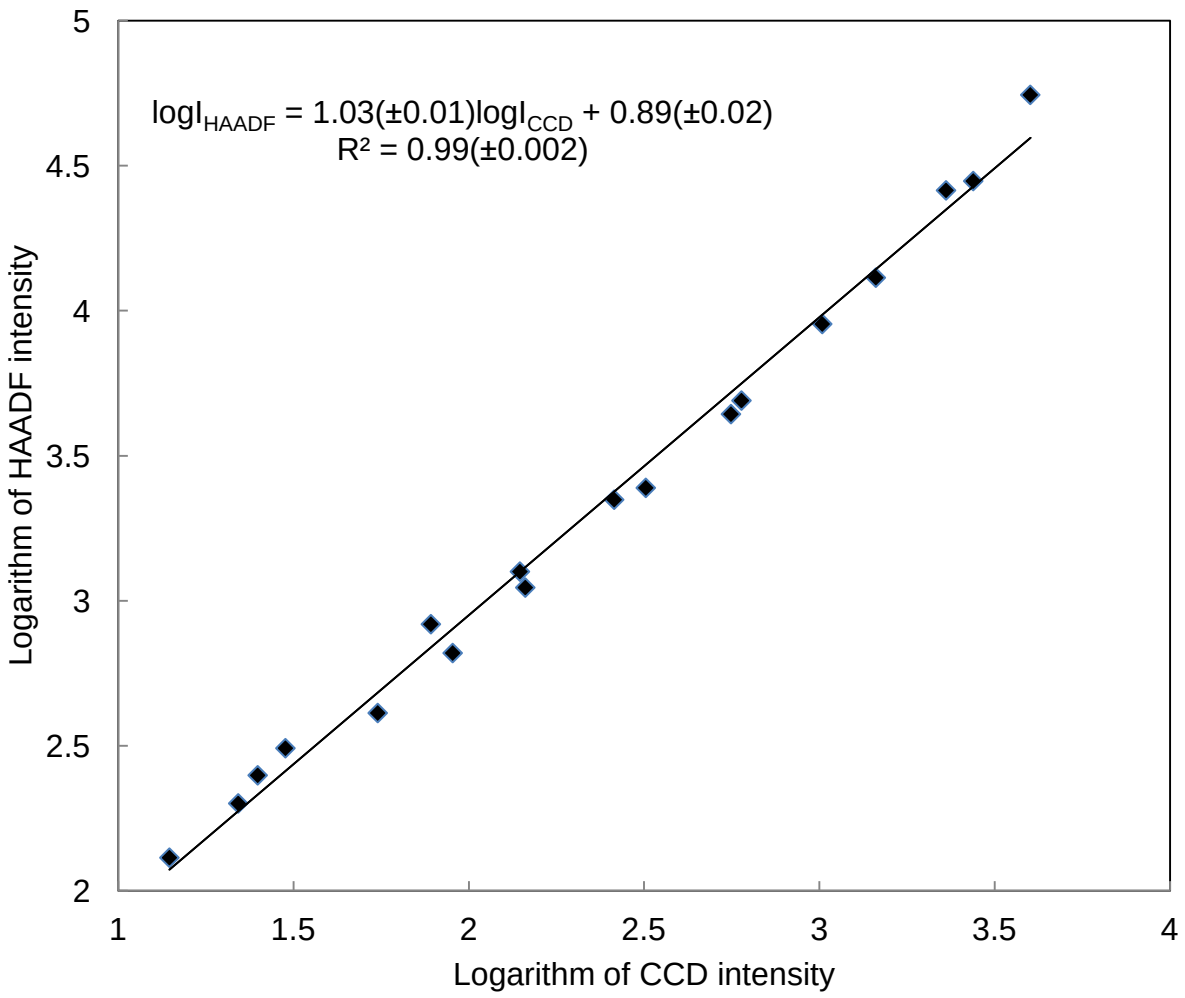

Figure 8: Intensity of the HAADF detector after background subtraction as a function of the CCD camera signal for different electron probes (the experimental error was determined by the Random Halves approach).

The relation between CCD and HAADF detector intensity can be stated as following:

$$logI_{HAADF} = BlogI_{CCD} + logA \quad (5)$$

By linear regression, “best-fit”, the slope, *B* = 1.03 (±0.01), y-intercept, *logA* = 0.89 (±0.02), and the correlation coefficient, r = 0.99 (±0.002) are determined i.e.

$$logI_{HAADF} = 1.03(\pm 0.01) logI_{CCD} + 0.89(\pm 0.02)$$

or,

$$I_{HAADF} = 7.8(\pm 1.0) I_{CCD}^{1.03(\pm 0.01)}$$

It can be noticed that the slope yields an almost linear response of the HAADF detector to the incident electron beam intensity as the parameter B is very close to 1 (but not exactly 1), *B* = 1.03 (±0.01). The correlation coefficient, r, is the measure of the reliability of this linear description. The values close to 1, r = 0.99 (±0.002), indicates excellent reliability. After this calibration of the detector signal to correctly account for non-linear effects, the fraction of electrons scattered onto the HAADF detector for each scan position in an experiment can be obtained. Before and after the measurement using HAADF-STEM for a sample a STEM image of the detector (in image mode, with the un-scattered incident beam) is acquired. This measurement is done twice to ensure that the electron beam intensity did not change “during the acquisition of HAADF-STEM” images. The data of the detector intensities are stored in binary format with 2-byte data depth for each pixel (intensities from 0 to 65535). This detector sensitivity measurement is done while the sample is retracted, and the detector intensity is averaged after background signal subtraction. The actual “data acquisition of the sample” is performed in the diffraction mode of the TEM. Again, quantitative intensities are stored in the same

binary format in addition to a tiff image with calibrated scale bar. For each pixel position the ratio between scattered electron intensity to incident electron intensity (as measured by scanning across the detector as described above) can be determined. However, this ratio needs to be corrected for the non-linear sensitivity of the HAADF-detector.

It should be emphasized here that the detector settings for contrast and brightness have to be kept fixed to the values used in calibrations. If other contract-brightness settings are used, a new detector calibration is therefore necessary.

3.1.2. Intensity-Composition Calibration

Multilayer systems provided by TriQuint Semiconductors in Apopka (FL) and FePt multilayer samples on a Si substrate prepared in the group of Dr. Coffey at UCF were used to compare HAADF intensities of neighboring layers with different compositions, assuming no thickness change across the interfaces. This yields relative intensities of layers for several single elements and some compounds, as shown in Figure 9.

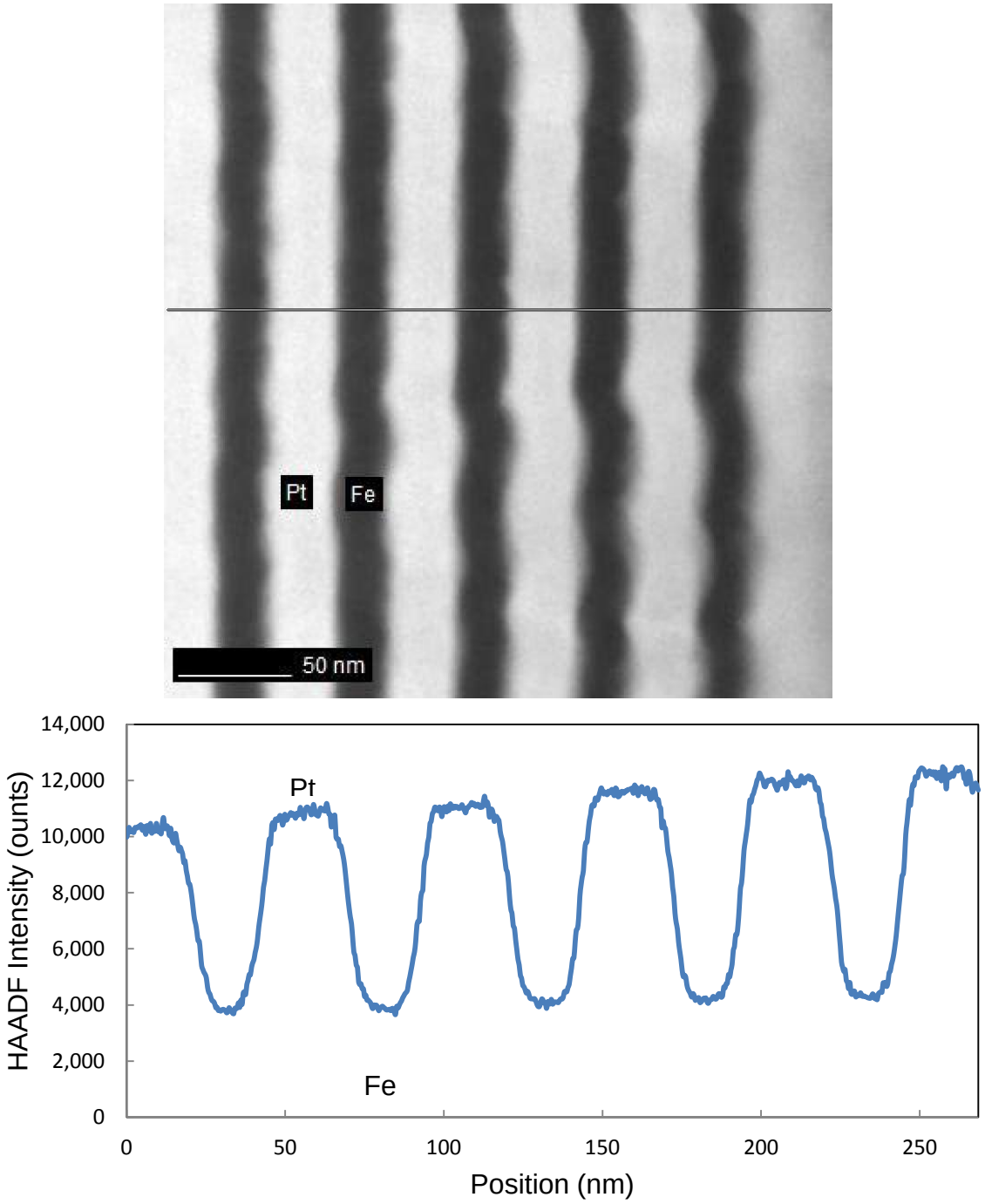

Figure 9: Top: HAADF-STEM micrograph of a Pt & Fe multilayer systems provided by Dr. Bo Yao used to compare HAADF intensities of neighboring layers, assuming no thickness change across the interface. This yields relative intensities of Pt (bright lines) with respect to Fe (dark lines).

3.1.3. CBED Measurement of Thickness

The upper right part of Figure 10 shows a FIB sample with a Si substrate at the bottom a SiO_2 layer, and Fe, Pt multilayers used for CBED verification of thicknesses determined by HAADF. The upper left of Figure 10 is a magnified bright-field TEM image, showing the location (at the tip of the beam stop) where the thickness is determined by CBED. The sample was provided by Dr. Bo Yao [97, 98].

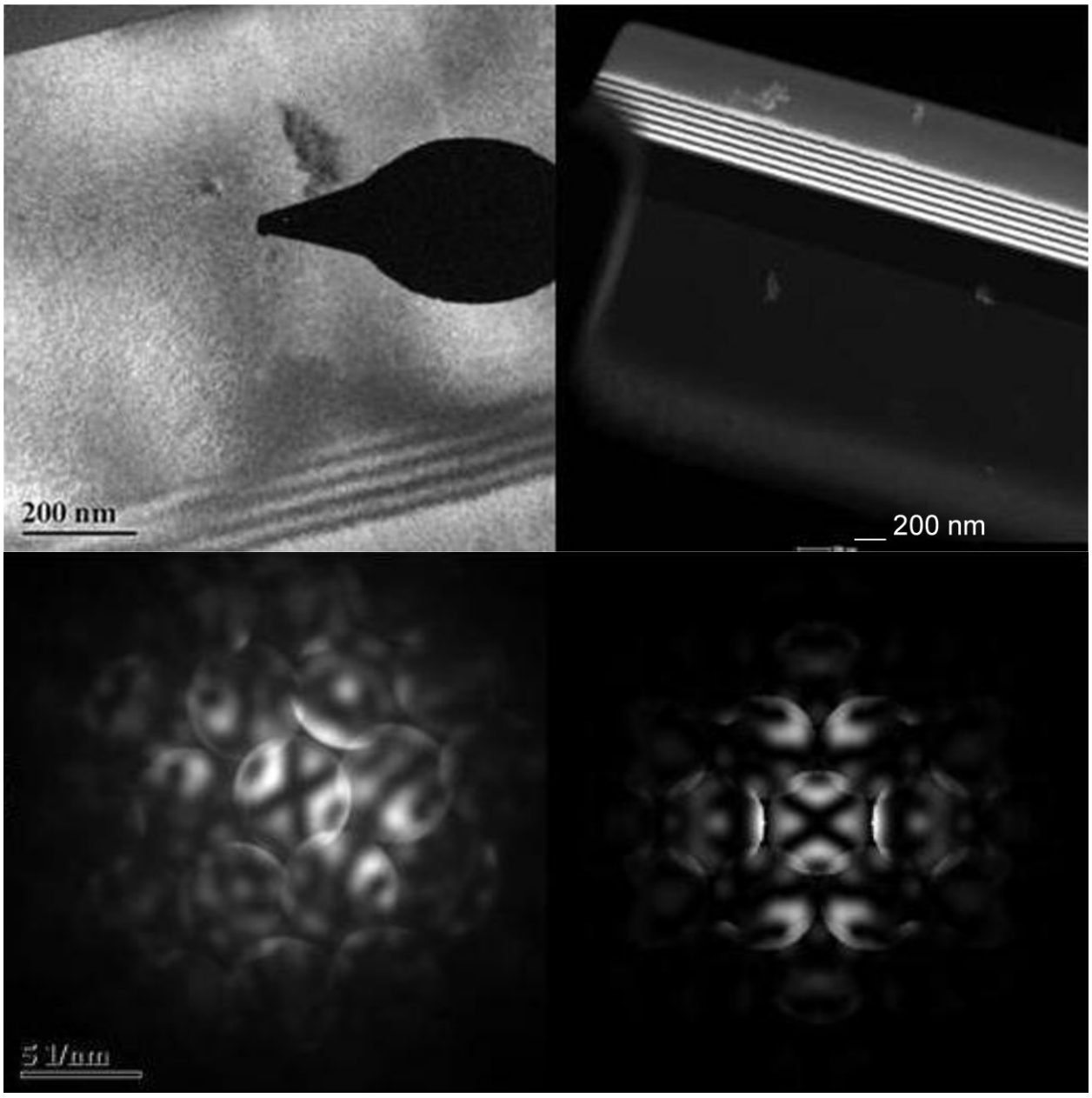

Figure 10: The thickness of silicon along <110> measured with CBED and used for calibration of the HAADF signal. See text for detailed explanations.

The lower left of Figure 10 is the experimental CBED pattern, and the lower right is the simulated CBED pattern with a thickness of t = (130±10) nm. The software used

for CBED simulations was developed by Zou et al. from UIUC [99]. The simulated CBED pattern that is closest to the experimental CBED pattern was used for thickness evaluation.

3.1.4. Intensity-Atomic Number (Z) Calibration

The experimental contrast calibration of intensity vs. atomic number is shown in Figure 11 [96]. With the average intensity on the detector for a specific spot size and condenser aperture size, the relative intensities (counts per nanometer) are transformed into the fraction ε of electrons scattered onto the HAADF detector for each nanometer of sample thickness for the respective material. The absolute scale of the scattered electrons per nm sample thickness was obtained from CBED measurements of the thickness of a Si single crystal as outlined in section 3.1.3.

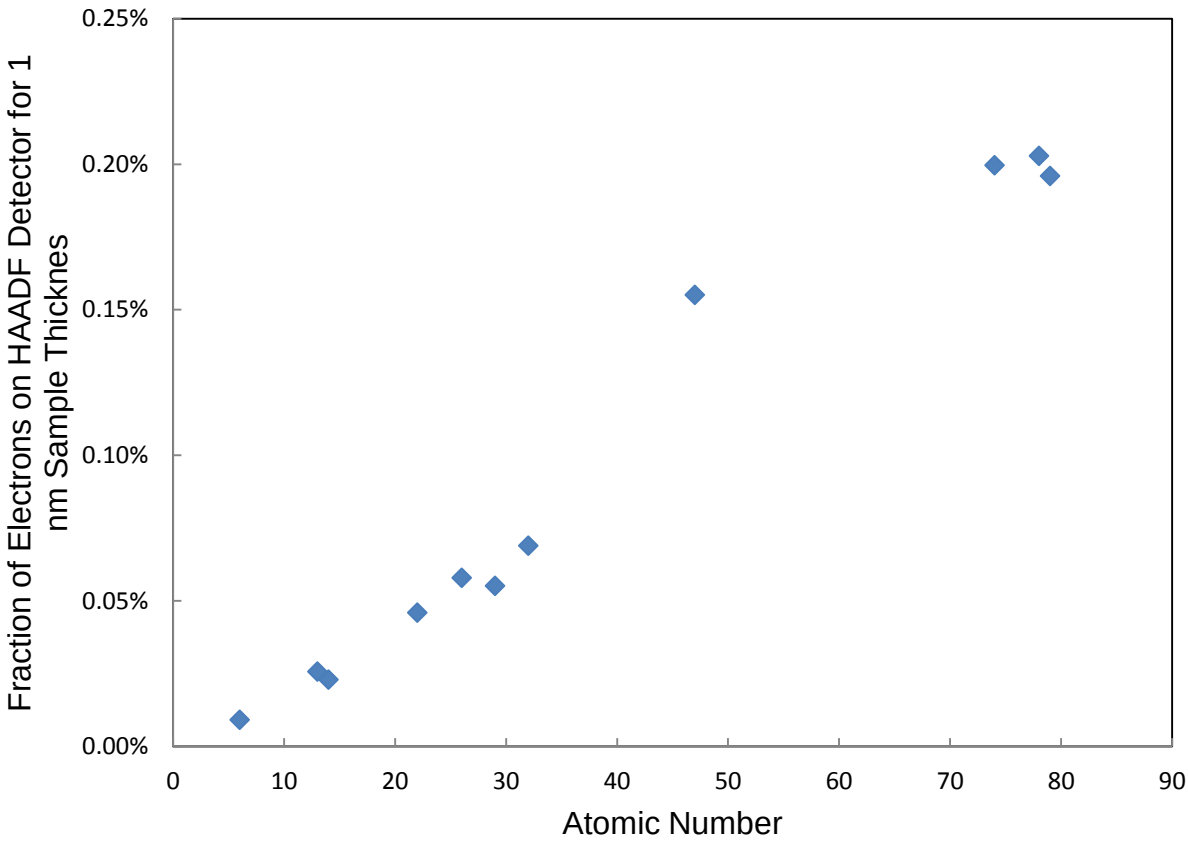

Figure 11: Fraction ε of electrons scattered onto the HAADF-STEM detector per nanometer of sample thickness for different pure elements.

Table 1: Data for both Figure 11 and Figure 12.

ε (nm^{-1})	ε (nm^{-1}), using data derived from [100]	element	Z	ρ, (g/cc)	W_{at}, (g/mol)	σ, (pm^2/at)	σ, (pm^2/at), [100]
0.010%	0.005-0.007%	Amorphous C	6	1.8-2.1	12.0	0.9	0.5-0.6
0.022%	0.015%	Al	13	2.7	27.0	3.7	2.3
0.024%	0.014%	Si	14	2.3	28.1	4.8	2.7
0.049%	0.036%	Ti	22	4.5	47.9	8.6	6.3
0.061%	0.077%	Fe	26	7.9	55.8	7.2	8.7
0.057%	0.085%	Cu	29	9.0	63.5	6.7	10.1
0.073%	0.057%	Ge	32	5.3	72.6	16.5	12.9
0.15%	0.163%	Ag	47	10.5	107.9	25.6	26.9
0.19%	0.394%	W	74	19.3	183.8	30.0	62.1
0.207%	0.457%	Pt	78	21.5	195.1	31.3	68.8
0.205%	0.441%	Au	79	19.3	197.0	34.7	70.6

Furthermore, by dividing this fraction per nanometer by the atomic density of a material, we can get the value for σ, the scattering cross-section (interaction coefficient) for the electrons scattered by an atom to the corresponding scattering angles of the HAADF detector,

$$\sigma = \frac{\varepsilon W_{at}}{N_A \rho} \tag{6}$$

where, ε is the fraction of intensity, W_{at} is the atomic mass, N_A is Avogadro's number, and ρ is the density.

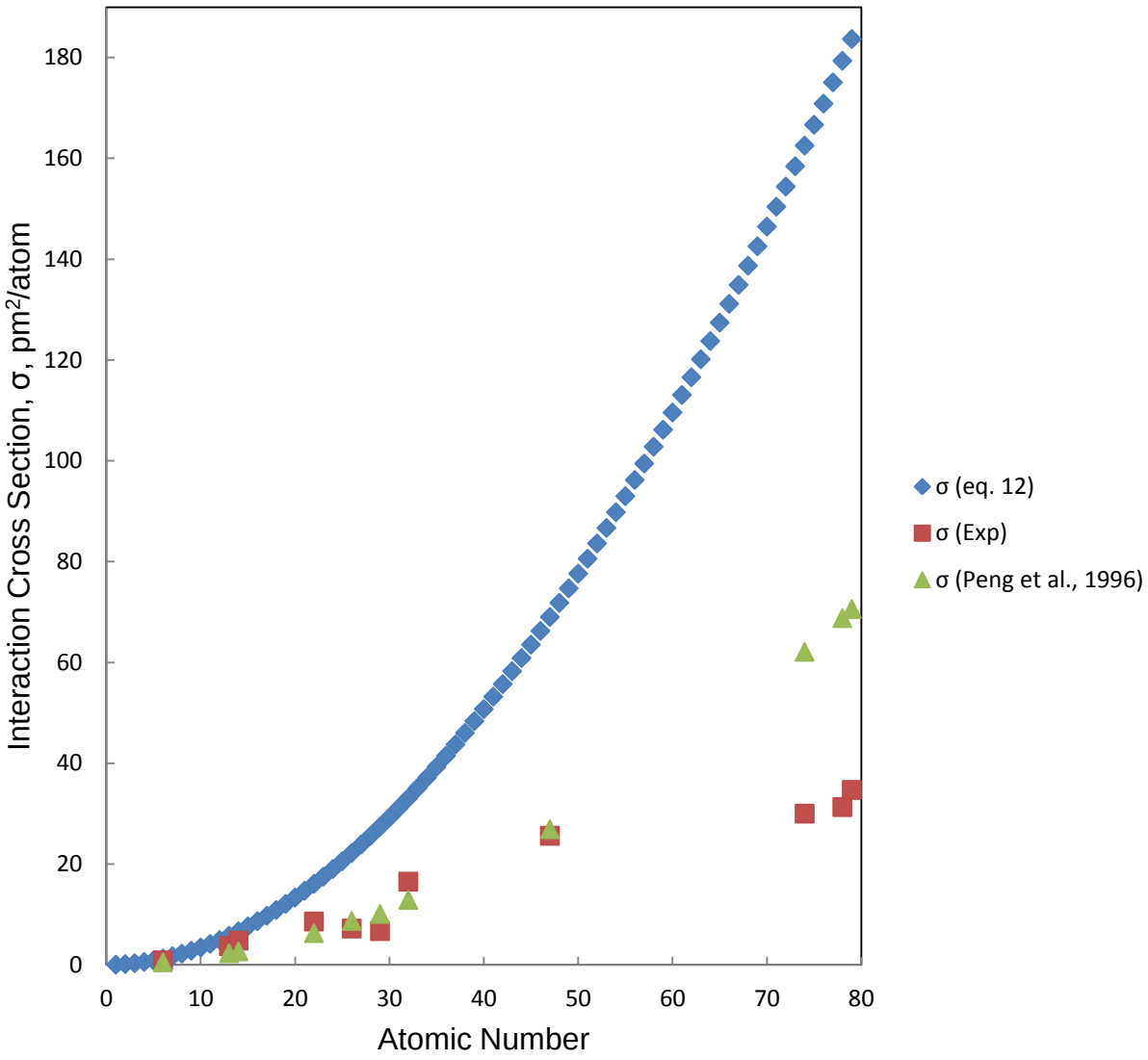

Figure 12: Interaction cross section for different pure elements. Exp data points are from experimental results. eq. 12 data points are from the prediction of equation 12. Peng et al., 1996 data points are from the derivation of Peng et al. paper [100]. .

Figure 12 confirms that the interaction cross section typically increases with an increase in the atomic number. However, the scattering signal does not follow pure Rutherford scattering proportional to Z^2, as the scattering signal for these scattering angles also is influenced by the electron contribution of each atom. The Exp data points are measured experimentally. The eq. 12 data points can be described by the following equation from dynamical elastic scattering theory, derived from Wentzel potential as described by Müller and Rose [101]:

$$U(\boldsymbol{r}) = -\frac{2\gamma Z}{a_H}\frac{\exp\left(-\frac{|\boldsymbol{r}|}{R}\right)}{|\boldsymbol{r}|} \tag{7}$$

where R is the shielding radius, $a_H = \frac{\hbar^2}{m_0 e^2}$ [1] denotes the Bohr radius and Z the atomic number. The parameter $\gamma = m/m_0$ is the relativistic correction.

The interaction cross section can be expressed by:

$$\sigma = \int |f(q)|^2 d^2q \tag{8}$$

where: the integral is over the detector, and

$$f(q) = \frac{2Z\left(1 + \frac{eV}{m_0 c^2}\right)}{a_{Bohr}(R^{-2} + q^2)} \tag{9}$$

where:

[1] Müller and Rose use equations without $(4\pi\varepsilon_0)^{-1}$ for interactions between charges, therefore a_H looks different than the Bohr radius in equation 11, however, $a_H = a_{Bohr}$.

$$R = \frac{a_{Bohr}}{Z^{1/3}} \tag{10}$$

$$a_{Bohr} = \frac{h^2 \varepsilon_0}{\pi m_0 e^2} \tag{11}$$

therefore,

$$\sigma = \frac{Z^2 \lambda^2}{\pi a_{Bohr}^2}(1 + \frac{eV}{m_0 c^2})^2 (\frac{1}{\frac{Z^{2/3}}{a_{Bohr}^2} + (\frac{2\pi}{\lambda})^2 4\Theta_{\min}^2} - \frac{1}{\frac{Z^{2/3}}{a_{Bohr}^2} + (\frac{2\pi}{\lambda})^2 4\Theta_{\max}^2}) \tag{12}$$

where σ is calculated interaction cross section, *Z* is atomic number, λ is wave length, a_{Bohr} is Bohr radius, eV is measured in electron volt, m_0 is rest mass, c is the speed of light, $2\Theta_{min}$ is the angle for scattering onto the inner radius of the detector, and $2\Theta_{max}$ is the angle for scattering onto the outer radius of the detector. Equation 12 yields nearly a Z^2 dependence of the interaction cross section. However, experimental data and use of realistic atomic potential as the one described by Peng et al. [100] yield significantly lower exponents for the atomic number dependence as described in equation 3. Using data from Peng et al. [100] a value of α=1.91±0.02 was found here. The experimental data indicate an even lower value of α=1.33±0.03.

The approach used by Peng et al. [100] describes the atomic scattering factor *f* as the sum of five Gaussian functions:

$$f\left(\frac{\sin(\theta)}{\lambda}\right) = \sum_{j=1}^{5} a_j e^{-b_j\left(\frac{\sin(\theta)}{\lambda}\right)^2} \tag{13}$$

where a_j and b_j are fitting parameters tabulated in [100] for each element and θ is the scattering angle in Braggs law (half the total scattering angle. After relativistic correction and integration over the detector angles used here, the scattering cross section σ has been determined for selected elements as shown with green triangles in Fig. 12. Note, that these cross sections are close to the experimental values for lower atomic numbers, while they deviate significantly for higher atomic numbers. One reason may be that I did not consider thermal diffuse scattering (TDS) in the determination of the scattering cross section. One reason not to consider TDS was the fact that these inelastic scattering events only cause small (sub eV) energy changes, and the electrons still hit the detector, as they get merely redistributed through TDS in the diffraction plane. Plasmon excitations are more effective to change the electron energy, but using the parameters for absorption given in Peng et al. [102] does not yield the absorptive behavior as determined for several elements in this work (see section 3.1.5).

Table 2: Experimental data of the electron fraction ε scattered on HAADF detector per nm sample thickness for compounds determined from various samples provided by TriQuint Semiconductors.

ε (nm^{-1})	Material
0.016%	SiO_2
0.021%	AlN
0.032%	$LiNbO_3$
0.047%	Al-Cu
0.015%	Ag_2Al
0.28%	$LiTaO_3$

3.1.5. Absolute Intensity Calibration

The calibration for the quantification of the atomic number-contrast (Z-contrast) method for the determination of the sample thickness can be done by wedge methods, using e.g. Ag_2Al platelets in an Al matrix [103], or by thickness calibrations using convergent-beam electron diffraction patterns [104] at specific sample locations. The wedge method using a pure Silicon (111) wafer [56] cleaved parallel to a second {111} plane has been used, and the HAADF-STEM micrographs of the wedge shaped Si sample are shown in Figure 13.

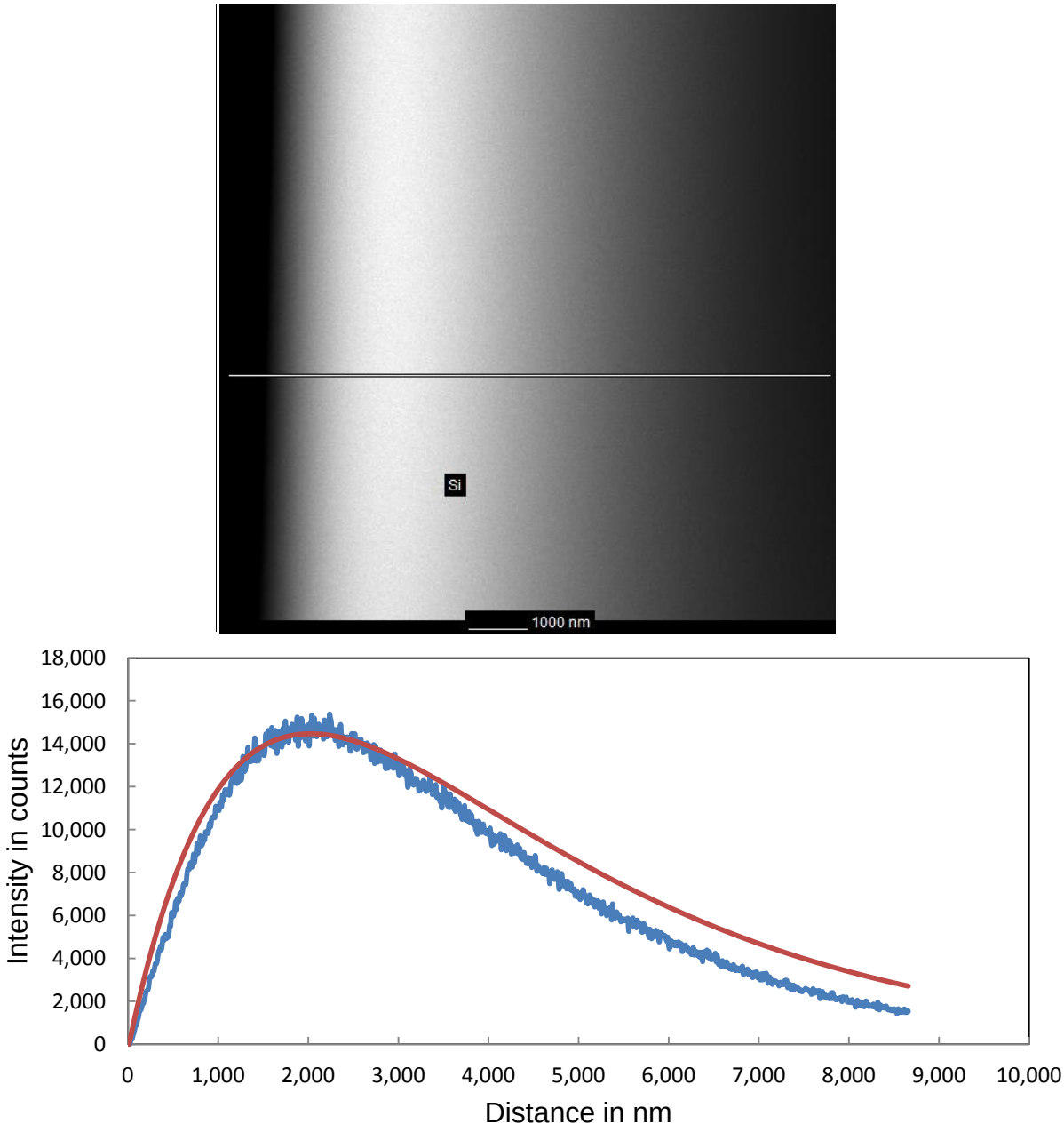

Figure 13: HAADF-STEM micrograph of a wedge-shaped pure Si (100) wafer cleaved parallel to {111} and viewed parallel to the [100] direction (Top). The incident beam intensity used was 5.7×10^4 counts, background signal is subtracted. Bottom: Line scan of intensity as a function of distance from the edge of the sample, The rough curve is from experiment data line scan from image on top of figure 13. The smooth curve is from the fitting intensity as a function of distance using equation 15 with K = 5.7×10^4 counts, F = 2.5×10^{-4} nm^{-1} and $\mu = 2.4 \times 10^{-4}$ nm^{-1}..

At the left side of the micrograph, the signal only reflects the background signal of the HAADF detector because the sample thicknesses are 0. The intensities are increasing as the sample thickness increases from left to right. The intensities reach maximum close to centers of the micrograph. Further increases of the thicknesses to the right result in the decrease of intensities because of absorption, and eventually go to 0.

The intensity increases are different for different orientations as the wedge-shaped sample is tilted. For the geometry of the sample used here the projected thickness *t* as a function of sample tilt α and distance d from the left edge is

$$t = d[\tan(\gamma + \alpha) - \tan\alpha] \tag{14}$$

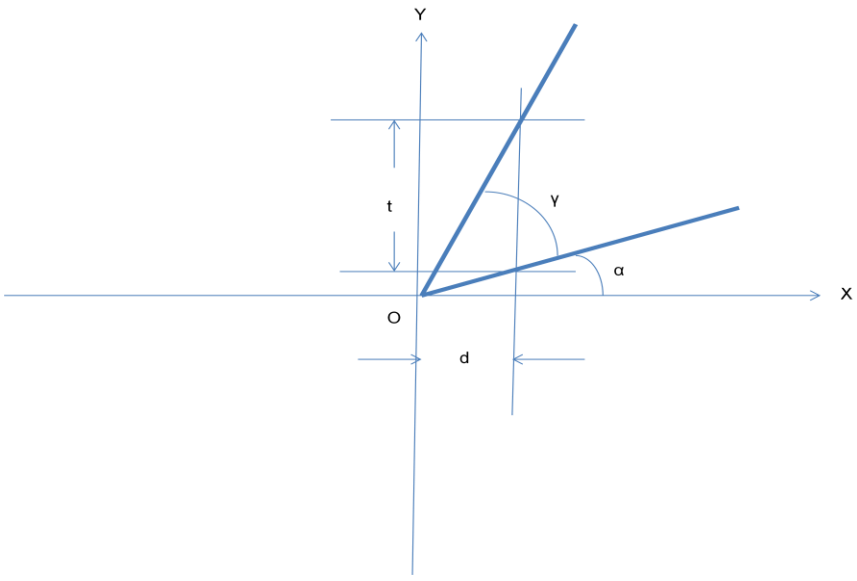

Figure 14: Schematic of tilting geometry. γ, the angle of the wedge shaped sample. α, the tilting angle of the lower surface of the sample.

where γ = 54.74° for the angle between (100) and (111). This yields a ratio *t/d* of 1.41 for the micrograph in Figure 13 with a sample tilt of 0°.

A simple approach can be used to describe the intensity as a function of sample position *d* from the edge (or thickness *t*) for this wedge-shaped Si sample based on the following principles:

1) For small sample thicknesses the HAADF-STEM intensity *I* increases linearly with sample thickness *t* described by $I=KFt$. Here, *F* is the fraction of electrons scattered per (nanometer) thickness as in the first column of table 1. This equation is equivalent to equation 3 above as given in the textbook by Williams and Carter [18], without specifics about the atomic number dependence of *F*.
2) However, for larger thicknesses equation 3 will fail, as the detector intensity could possibly exceed the incident beam intensity. It essentially assumes the constant incident beam intensity throughout the whole thickness of the sample. Therefore a modification has to be used which accounts for the reduction of the incident beam intensity (due to scattering) as the beam travels through a thicker sample: $I=K\,[1-\exp(-Ft)]$. For thin samples the intensity still increases linearly with thickness, however, for thicker samples the HAADF-detector intensity *I* does approach the value of the original incident intensity I_0, but never exceeds it.

3) A pre-factor *K* is used instead of the incident intensity I_0 as for thick samples the diffuse scattered intensity is distributed over the detector and over the central hole in the detector as well as beyond the outer radius of the detector. The ratio K/I_0 describes the fraction of all not-absorbed electrons after passing through a thick sample that hit the detector in the detector plane.
4) Additionally, we have to take care of absorption reducing the intensity with an exponential term $\exp(-\mu t)$. The whole thickness dependent HAADF-intensity can therefore be written as:

$$\frac{I}{I_0} = \frac{K}{I_0}(1 - e^{-Ft})e^{-\mu t} \tag{15}$$

The parameters *F* and μ in this equation can be determined using the following approach for this wedge shaped silicon sample: The distance from the edge is transformed into a sample thickness using equation 14. The maximum relative intensity $J_T = I_{max}/I_o$ and the value for the thickness *T* for this maximum intensity is determined. Additionally, the relative intensity J_{2T} at a thickness $2T$ is determined.

Using the ratio $L = (J_T)^2/J_{2T}$ the absorption term $\exp(-\mu t)$ can be eliminated, and the parameter *F* is given by

$$Ft = \ln \frac{1+L}{1-L} \tag{16}$$

Evaluating the 0^o case, a value of L=0.34±0.02 is determined. For d_{Max}=2.0x10^3 nm (T=2.83x10^3 nm) a value of (2.5±0.3)x10^{-4} nm^{-1} can be found for F. This is in close agreement with the value given in table 1 for silicon. The value for Si given in table 1 was determined using thickness calibrations with localized Convergent-Beam Electron Diffraction (CBED) measurements as outlined in chapter 3.1.3. The two calibration values for the contrast of Si are the same within the error bars of about 10%.

The thickness at the maximum intensity also yields the absorption coefficient μ:

$$\mu = \frac{F}{e^{Ft} - 1} \tag{17}$$

With this, an absorption coefficient μ = (2.4 ± 0.03)x10^{-4} nm^{-1} is determined from the measurement of the wedge-shaped Si sample. For the experimental conditions used the absorption coefficient of Si is about the same as the scattering strength F of silicon for scattering on the HAADF detector.

To verify the equation 15 proposed, several wedge shaped samples were prepared by FIB. A tungsten sample with γ = 20.6° was prepared by FIB. Figure 15 is a plane-view FIB micrograph of the sample just after removing it from the surface, as acquired in the FIB system with the gallium beam for imaging. The corresponding HAADF-STEM micrograph is shown in Figure 16.

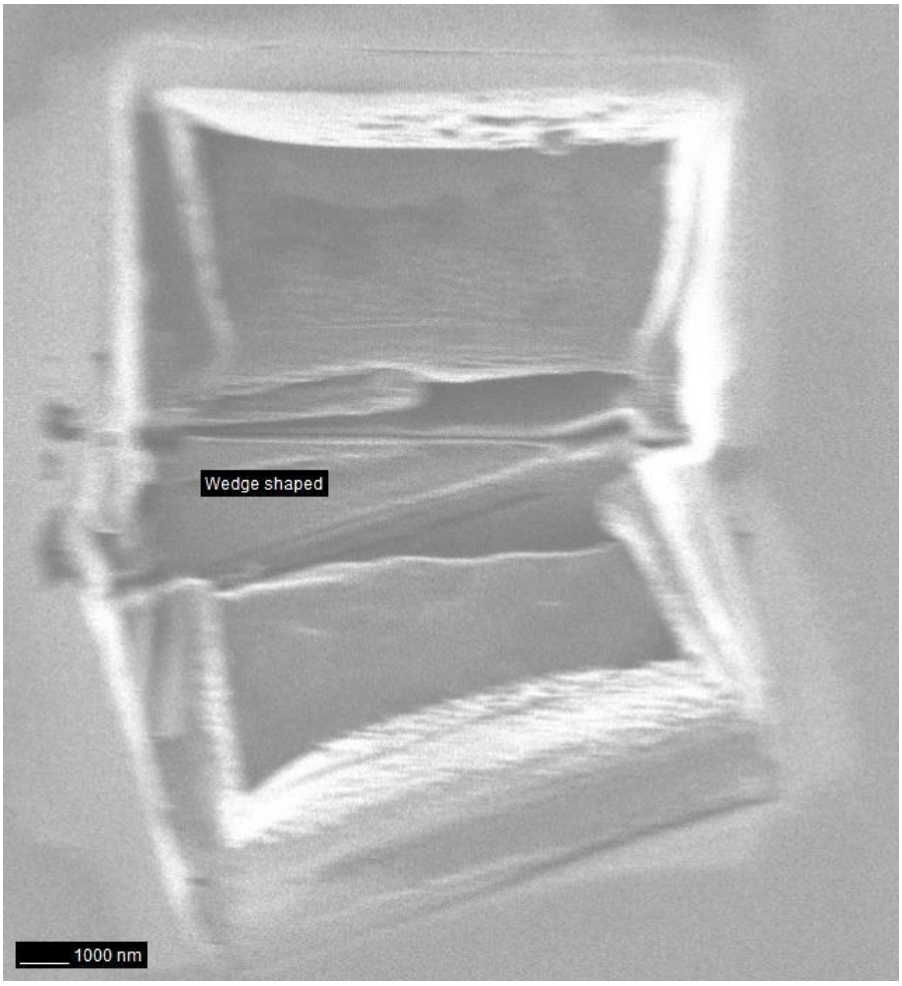

Figure 15: FIB micrograph of wedge shaped W (marked) showing the angle of the wedge shaped cut of γ = 20.6°.

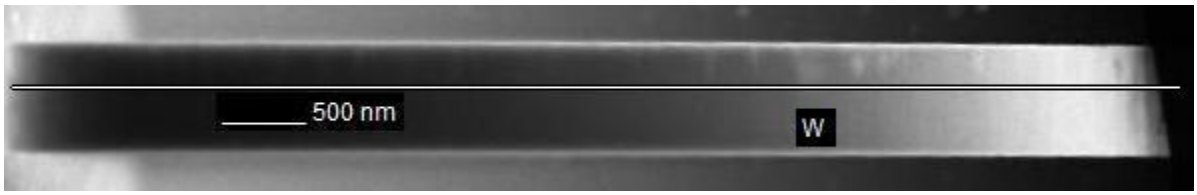

Figure 16: HAADF-STEM micrograph of wedge shaped sample with a tungsten layer. From right to left the thickness is increased. There are several other layers present, which are evaluated separately from the tungsten layer. There is an AlN layer above the W layer, a thin 100 nm Al layer below (darker) and below that SiO_2. The corresponding HAADF-STEM intensity profile (line scan) for W is shown in Figure 17.

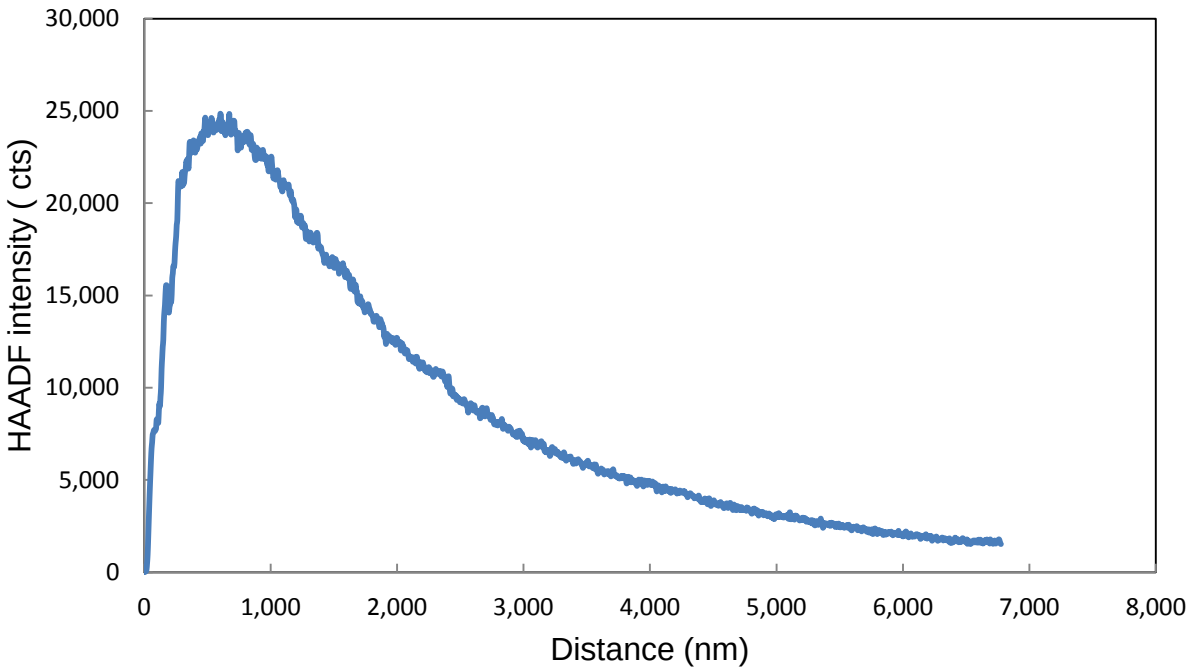

Figure 17: HAADF intensity profile of wedge shaped W vs. distance with background signal subtracted.

Using equation 14 to convert distance d to thickness t, the HAADF-STEM intensity profile of wedge shaped W vs. thickness t is shown in Figure 18. In equation 15, I_0 the incident beam intensity may have to be reduced to a constant K. If we define L = $I^2(t)/I(2t)$, and M = $I^2(2t)/I(4t)$, then $K^2 = L^2M/(2L-M)$, F = $(\ln((K+L)/(K-L)))/t$, $\mu = (\ln(2KL/(K+L)/I(t)))/t$. $I_0 = 8.1\text{x}10^4$ counts, K = $3.67\text{x}10^4$ counts, F = $1.14\text{x}10^{-2}$ nm^{-1}, $\mu = 1.37\text{x}10^{-3}$ nm^{-1}. From the FIB cutting angle of 20.6^o the each position (the 'Distance' in the x-axis of Fig. 17) can be translated in a sample thickness through multiplication with $\tan(20.6^o)$ as done for Fig. 18.

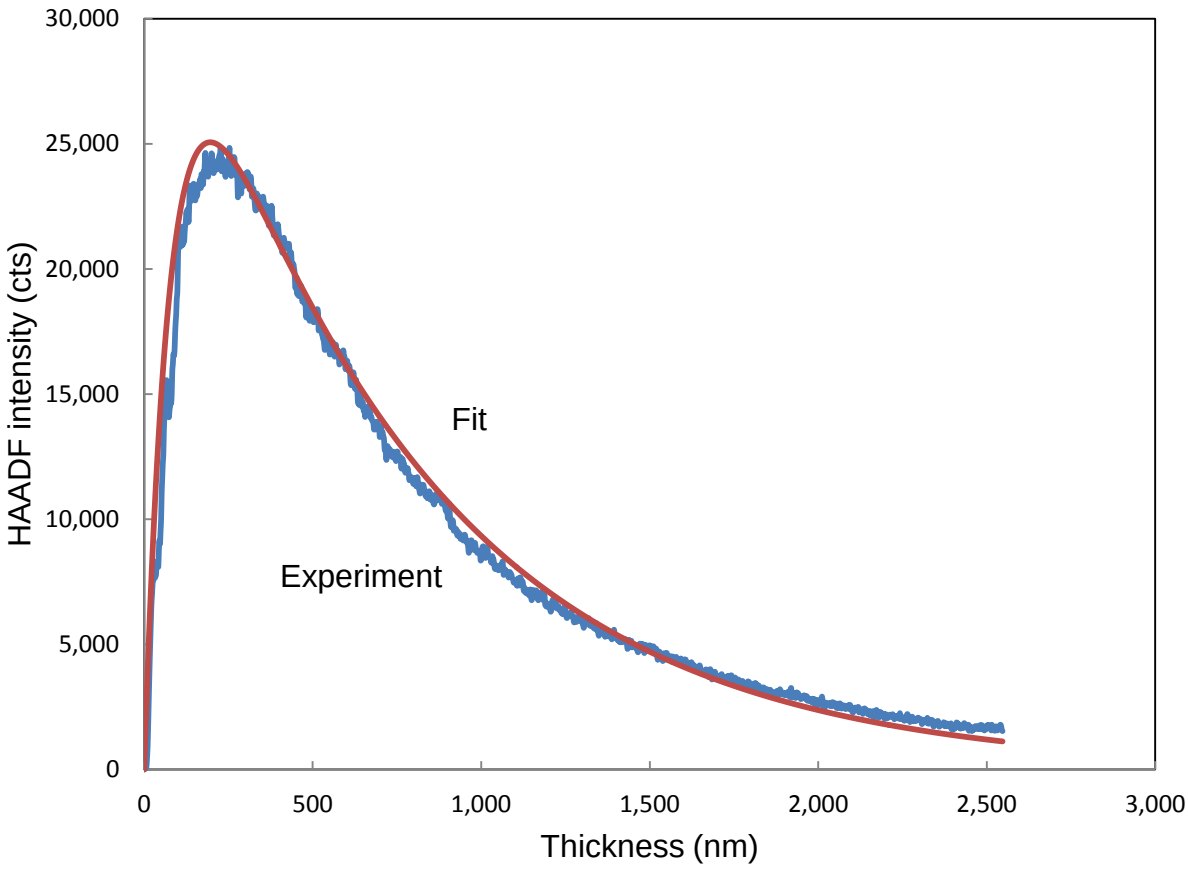

Figure 18: HAADF intensity of wedge shaped W vs. t for both experiment and fit with the parameters I_0 = 8.1x10^4 counts K = 3.67x10^4 counts, F = 1.14x10^{-2} nm^{-1}, μ = 1.37x10^{-3} nm^{-1}, initial slope ε = 3x10^{-3} nm^{-1}.

The model and the experimental curve are similar, but do not match perfectly. This could be explained by the fact that the angle α in equation 14 is assumed to be 0. Additionally, it is expected that the FIB cut is not producing the perfect wedge-shaped sample geometry.

One interesting feature in Figure 16 deserves discussion here: At the interfaces of the tungsten layers with the lower-density layers we can clearly see increased

intensities as bright lines. These lines indicate that at the edge of a high-density material, electrons get scattered from the high-density material into the neighboring low-density material (Si for the layer above W and Si for the layer below W in this case) where the absorption coefficient is smaller. Therefore, if the electron beam is focused at the edge of the high-density material (but within), a fraction of electrons scattered to high angles exists this material and traverses into the low-density material. These electrons suffer less absorption losses and reach the HAADF detector. This edge effect of high density versus low-density material is a typical feature for thick samples as they are prepared by FIB. Only for samples below about 100 nm thickness this effect is negligible and HAADF micrographs can be interpreted through direct atomic number contrast methods.

A wedge-shaped Fe-Pt multilayer system with $\gamma = 24.0°$ was prepared by FIB as shown in Figure 19. The corresponding HAADF-STEM micrograph is represented in Figure 20. The sample was provided by Dr. Bo Yao and consists of six Fe and six Pt layers on a SiO_2 layer on a Si substrate [97, 98].

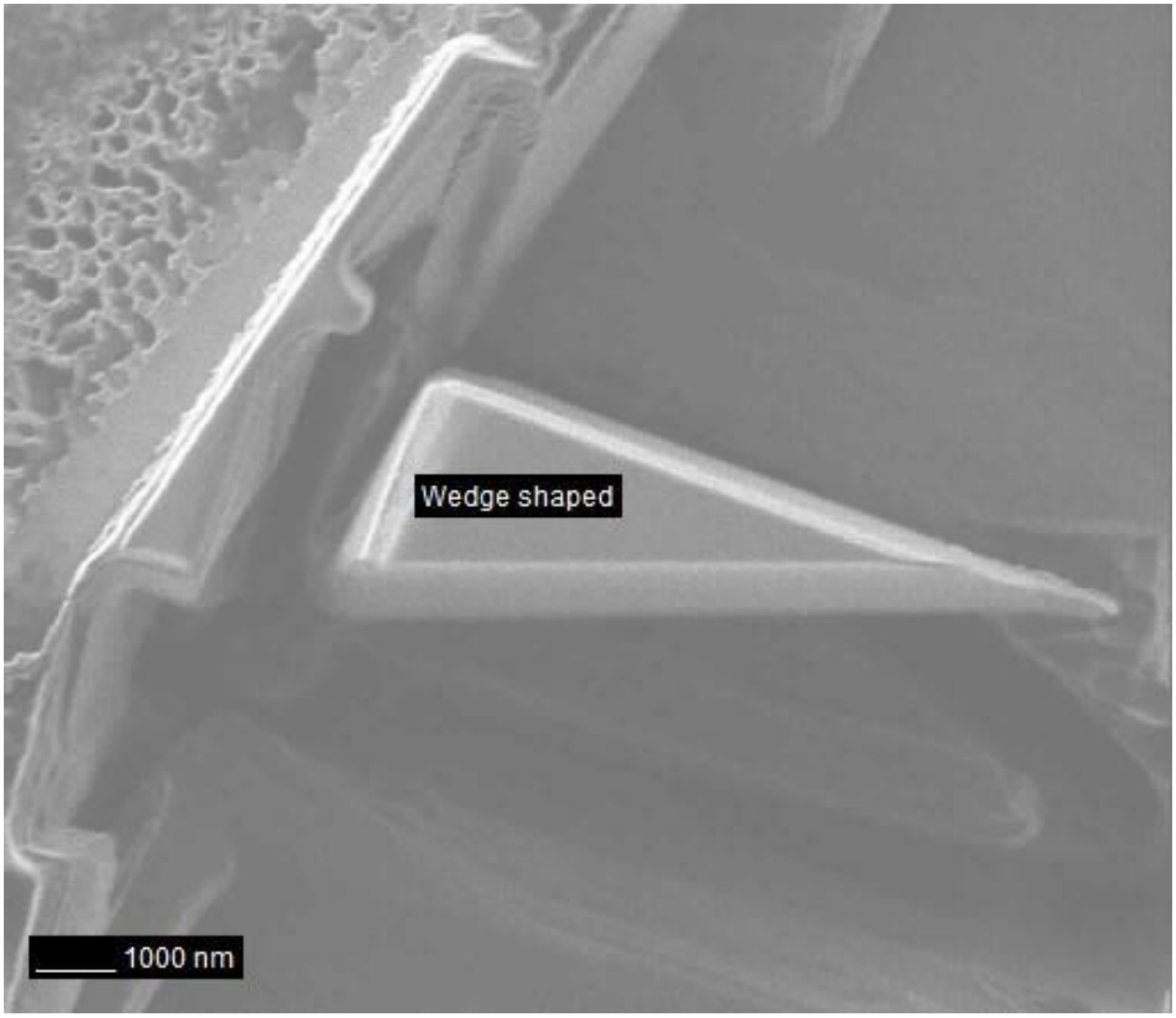

Figure 19: FIB micrograph of wedge shaped Pt showing the angle of the wedge shaped cut of γ = 24.0°.

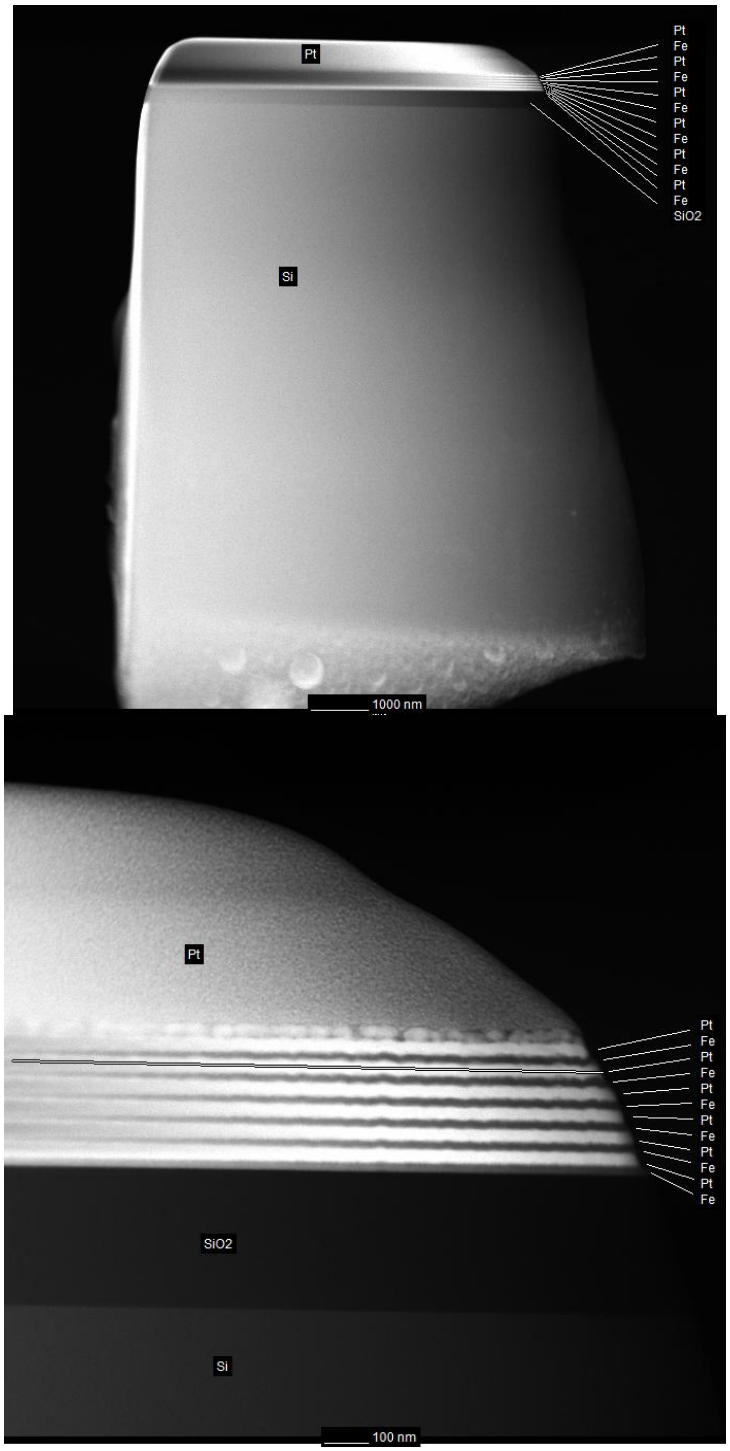

Figure 20: HAADF-STEM micrograph of wedge shaped Pt showing 6 Pt layers separated by 6 Fe layers on a SiO_2 layer on Si. From right to left (top), the thickness is increased. On the right, Pt layers are bright, and the 6 Fe layers are dark. The corresponding intensity profile (line scan) is shown in Figure 21. Higher magnification image is shown in botton. The layer below is SiO_2, and the substrate is Si.

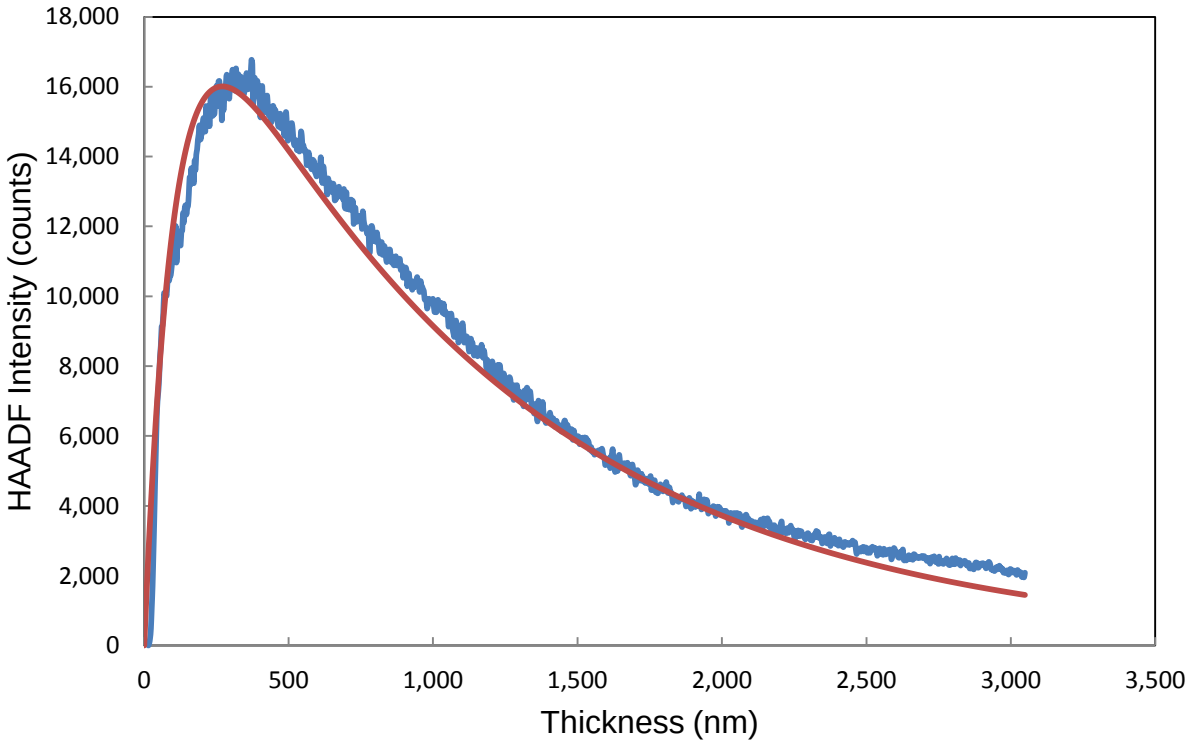

Figure 21: HAADF-STEM intensity vs thickness of wedge shaped sample for the Pt layer. The experimental curve (rough) is fitted (smooth) with $I_0 = 5.6 \times 10^4$ counts, K = 2.25×10^4 counts, F = 8.8×10^{-3} nm^{-1}, and $\mu = 9.0 \times 10^{-4}$ nm^{-1}, initial slope $\varepsilon = 3 \times 10^{-3}$ nm^{-1}.

In another attempt to check the validity of equation 15, a wedge shaped sample with a gold layer on $LiTaO_3$ with $\gamma = 22.9°$ was cut by FIB as shown in Figure 22. The corresponding HAADF-STEM micrograph of the cross section in Figure 23 shows that there was some heterogeneous gallium ion milling at the tip of the gold layer on the right side of Figure 23. Therefore, data for the thin gold part sample are not reliable in their conversion of position into sample thickness. At this edge the angle gamma may be different than the global angle of 22.9 degrees.

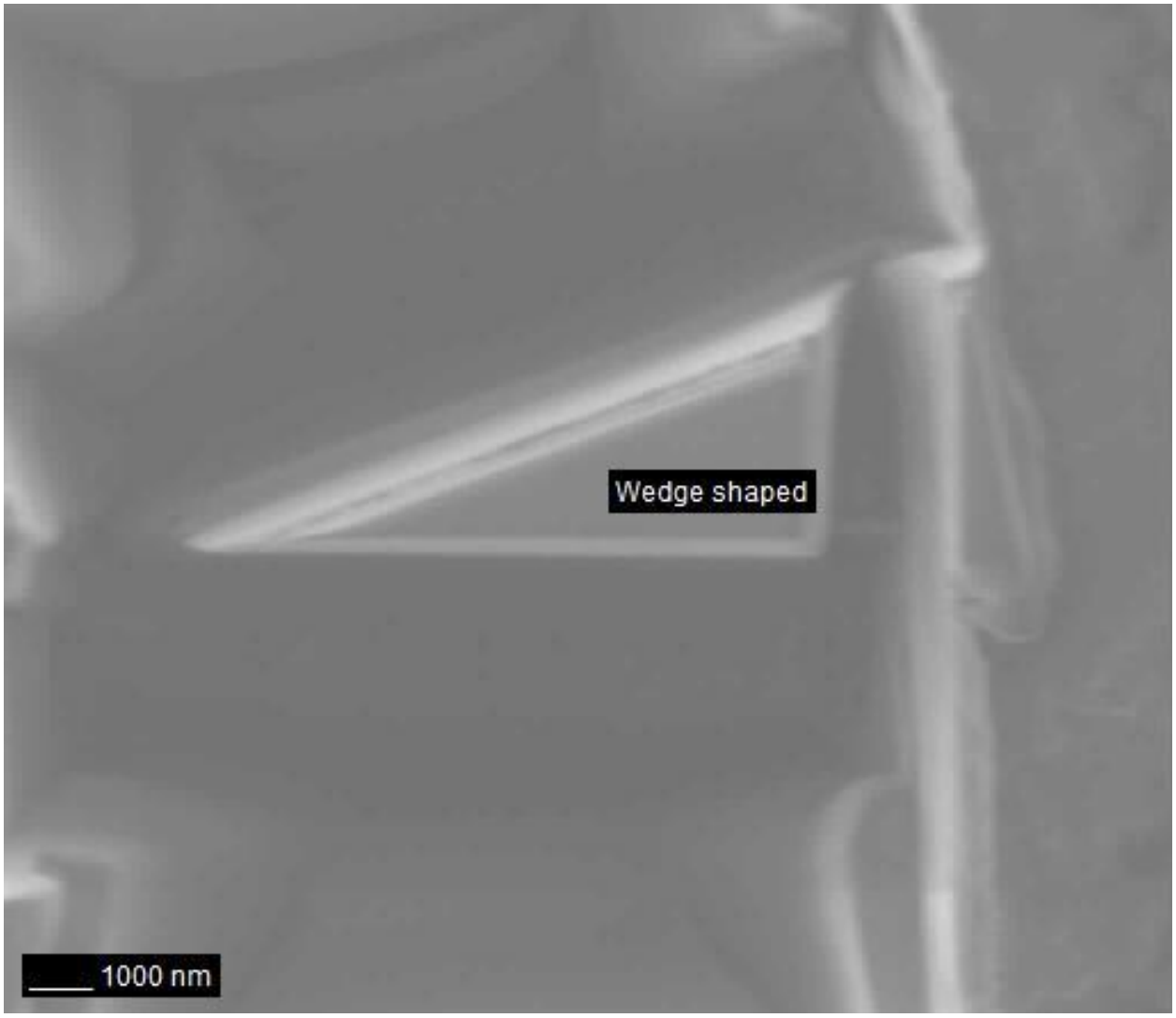

Figure 22: FIB micrograph of wedge shaped Au showing the angle of the wedge shaped cut of γ = 22.9°.

Figure 23: HAADF-STEM micrograph of wedge shaped Au. From left to right, the thickness increases. The corresponding intensity profile (line scan) is shown in Figure 24. The layer above Au is Pt from the FIB deposition process, and the substrate below is $LiTaO_3$.

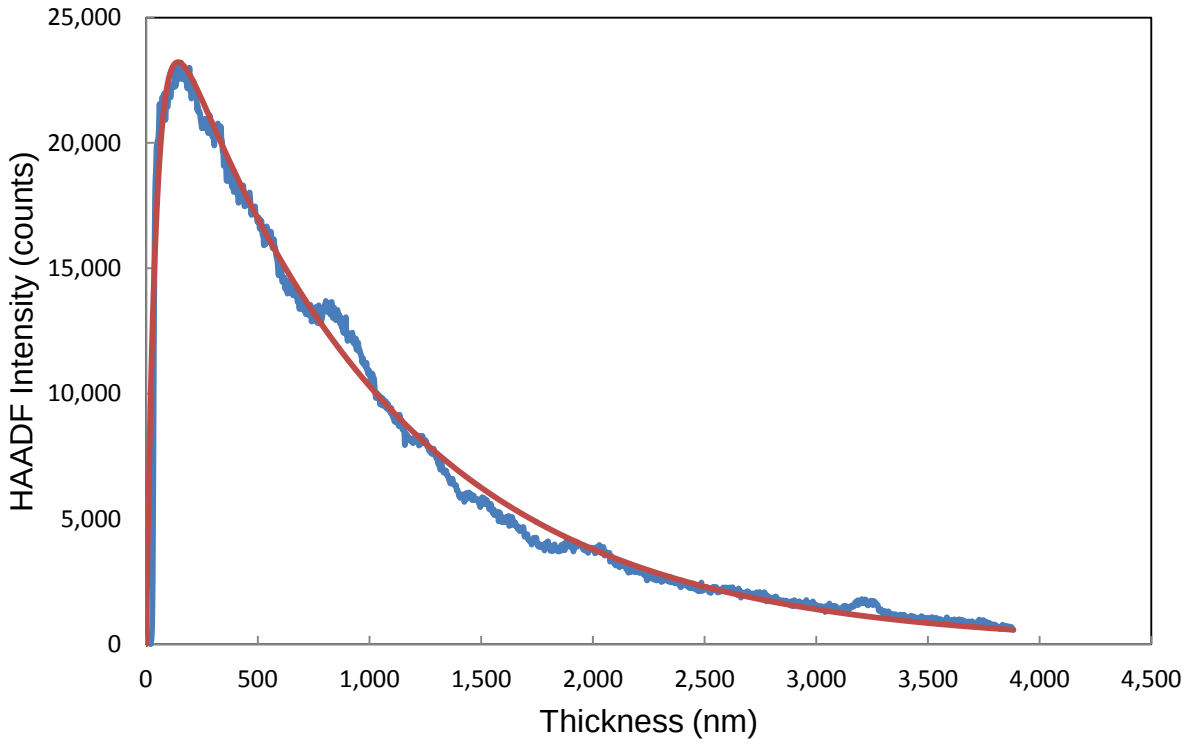

Figure 24: HAADF-STEM intensity vs thickness of wedge shaped sample for the Au layer. The rough experimental curve is fitted with $I_0 = 8.1 \times 10^4$ counts, $K = 2.8 \times 10^4$ counts, $F = 2.2 \times 10^{-2}$ nm^{-1}, and $\mu = 1.0 \times 10^{-3}$ nm^{-1}, initial slope $\varepsilon = 1 \times 10^{-3}$ nm^{-1}.

Furthermore, a wedge shaped sample of Cu on Si with γ = 23.7° was prepared as shown in the FIB micrograph of Figure 25. The corresponding HAADF-STEM micrograph is shown in Figure 26 with the Pt coating (in the FIB) on top of the Cu layer showing some penetration into the Cu layer as the copper layer is exhibits a rough surface.

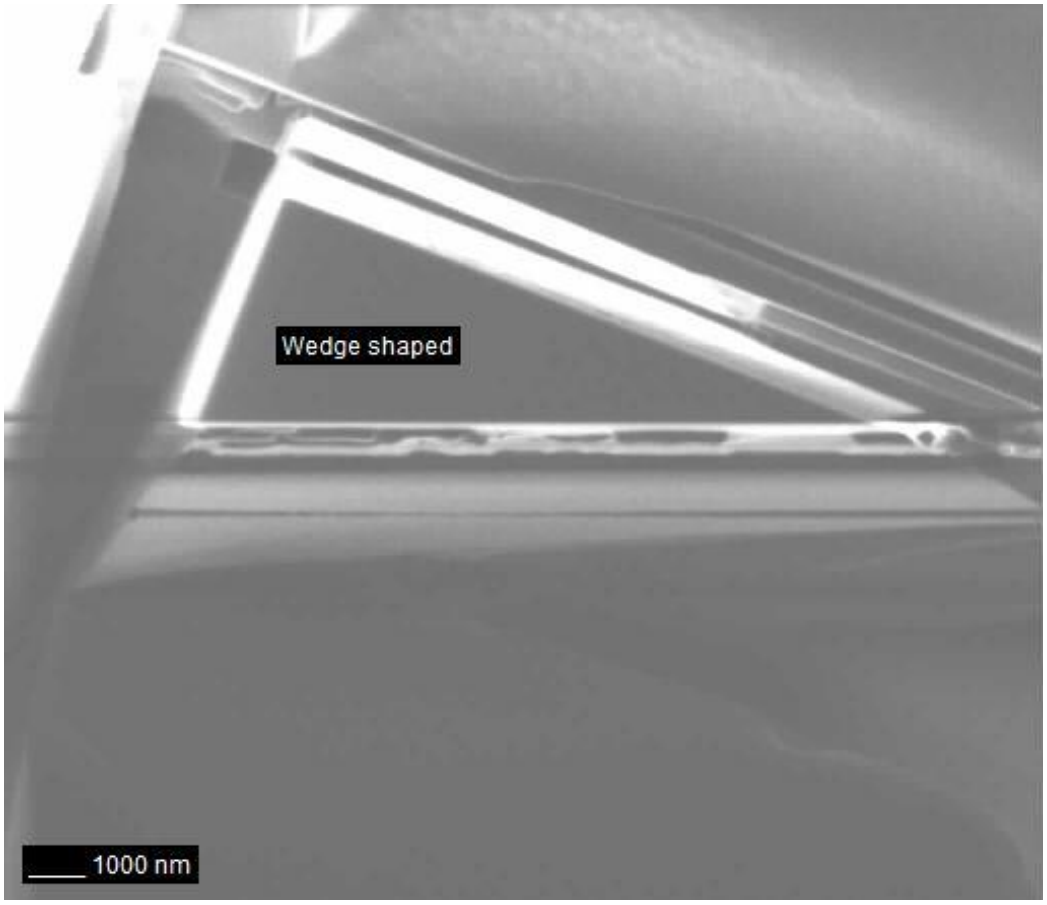

Figure 25：FIB micrograph of wedge shaped Cu showing the angle of the wedge shaped cut of γ = 23.7°.

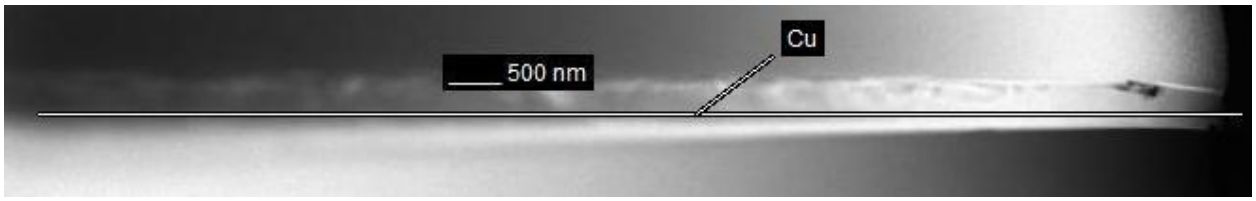

Figure 26: HAADF-STEM micrograph of wedge shaped Cu. From right to left, the thickness increases. The corresponding intensity profile (line scan) is shown in Figure 27.

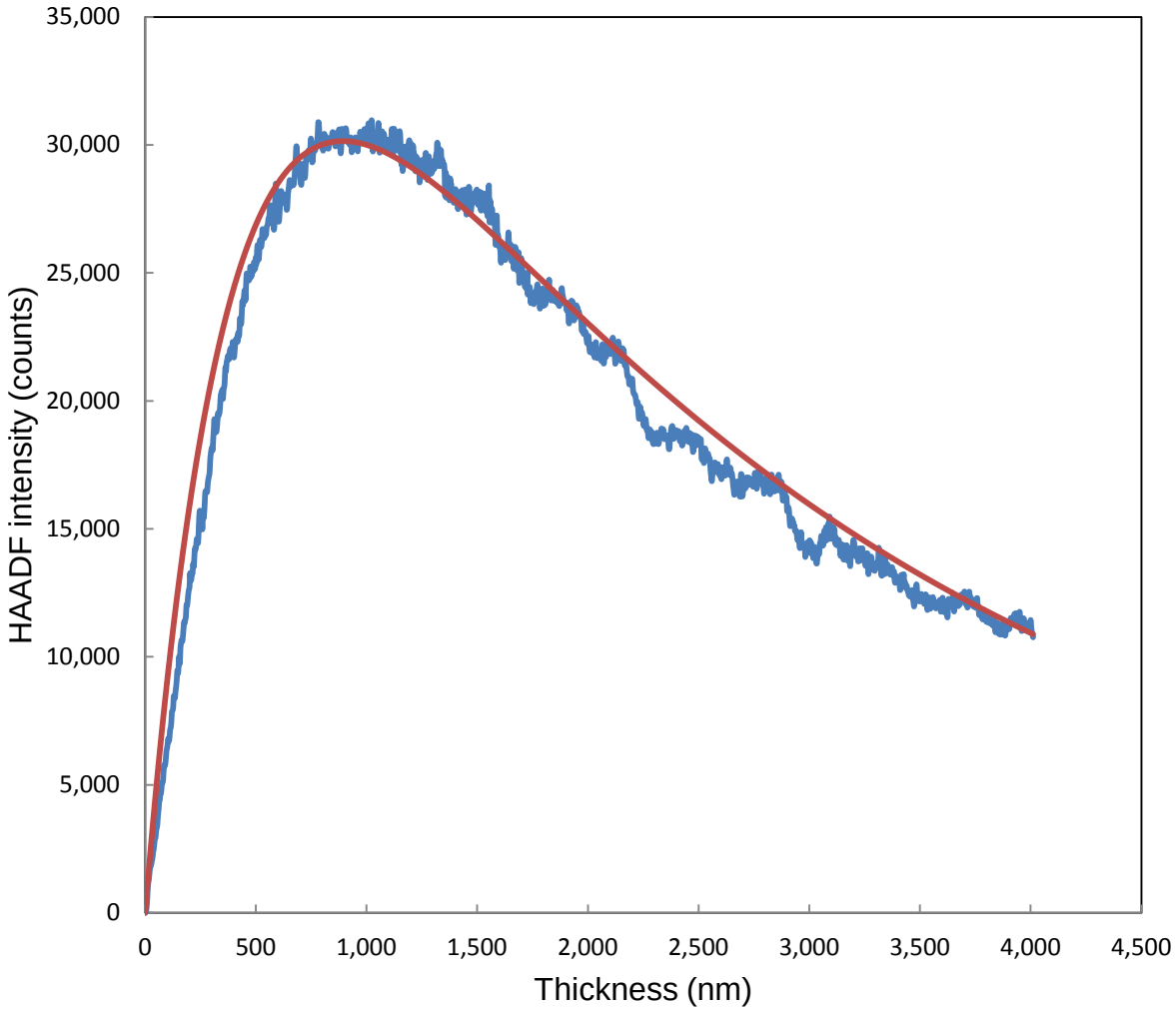

Figure 27: HAADF-STEM intensity vs thickness of wedge shaped Cu for both experiment and fitting with I_0 = 6.2x10^4 counts, K = 5.0x10^4 counts, F = 2.1x10^{-3} nm^{-1}, and μ = 3.8x10^{-4} nm^{-1}, initial slope ε = 1.1x10^{-3} nm^{-1}.

The following figures are focused on thin part of the samples so that initial slopes can be determined. Even the two thick samples with maximums are used to study the initial thin areas for ε determinations.

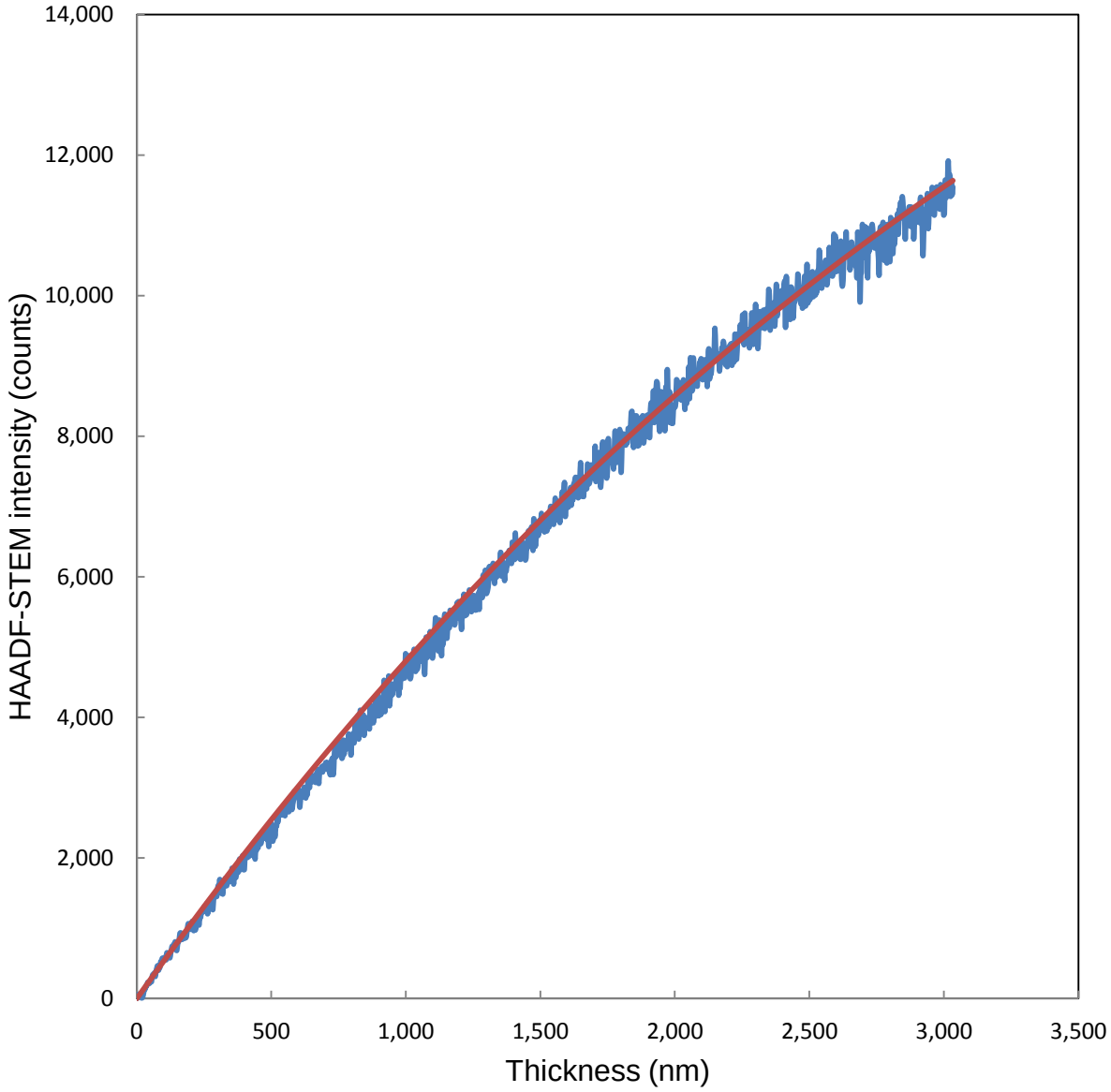

Figure 28: Si from PtFe sample, I_0 = 5.6x10^4 counts, fitting with K = 2.25x10^4 counts, and F = 2.4x10^{-4} nm^{-1}, initial ε = 1.0x10^{-4} nm^{-1}.

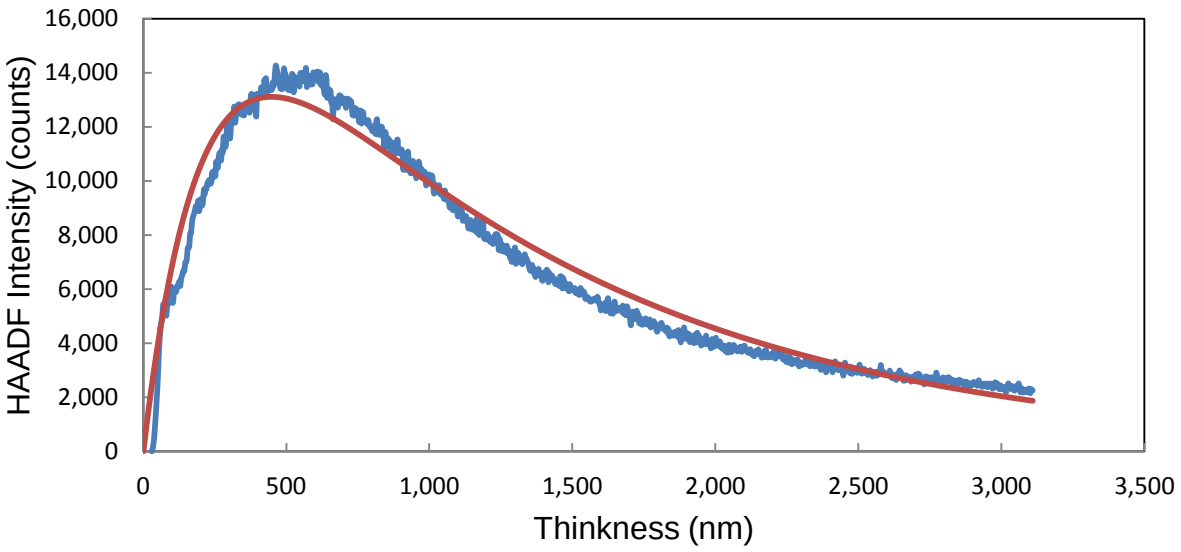

Figure 29: Fe from PtFe sample, I_0 = 5.6x10^4 counts, fitting with K = 2.25x10^4 counts, and F = 4x10^{-3} nm^{-1}, μ = 8x10^{-4} nm^{-1}, initial slope ε = 6.1x10^{-4} nm^{-1}.

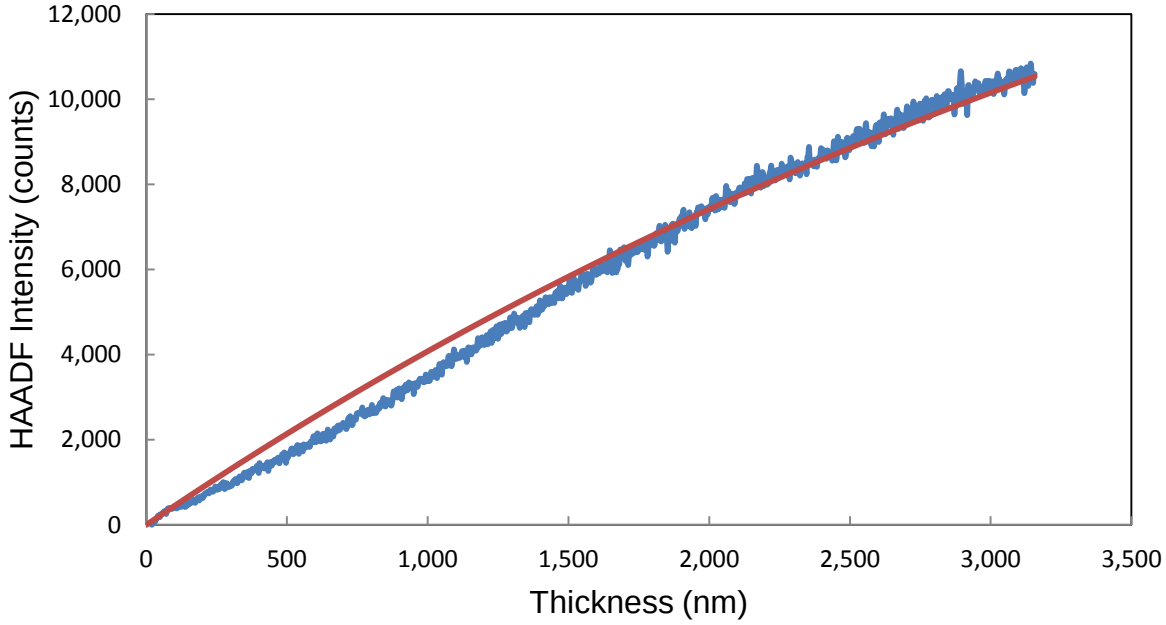

Figure 30: SiO_2 from PtFe sample, I_0 = 5.6x10^4 counts, fitting with K = 2.25x10^4 counts, F = 2x10^{-4} nm^{-1}, initial slope ε = 5x10^{-5} nm^{-1}.

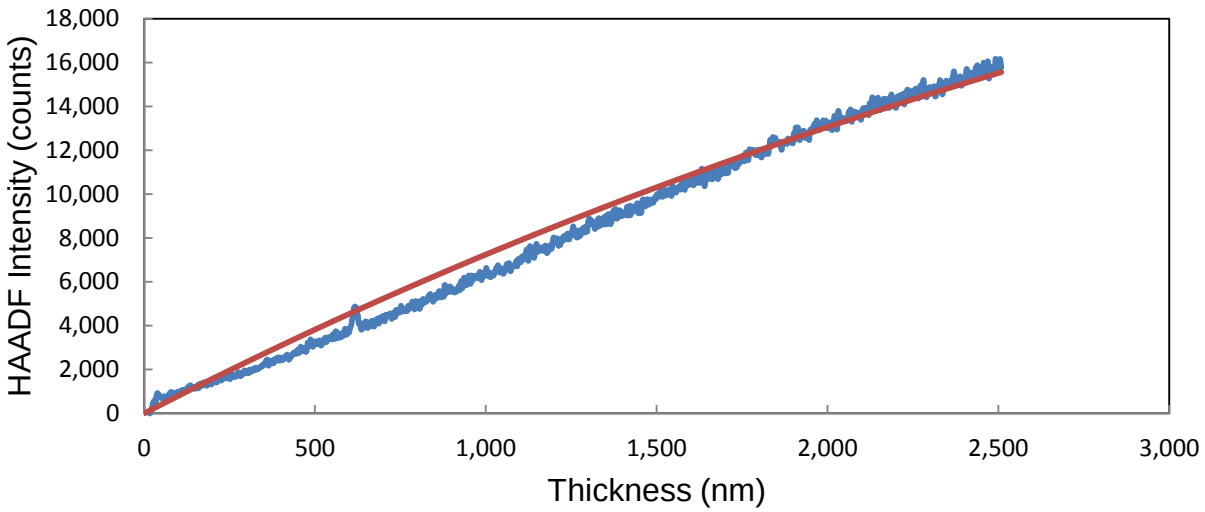

Figure 31: AlN from W sample, I_0 = 8.1x10^4 counts, fitting with K = 3.67x10^4 counts, and F = 2.2x10^{-4} nm^{-1}, initial ε = 6.0x10^{-5} nm^{-1}.

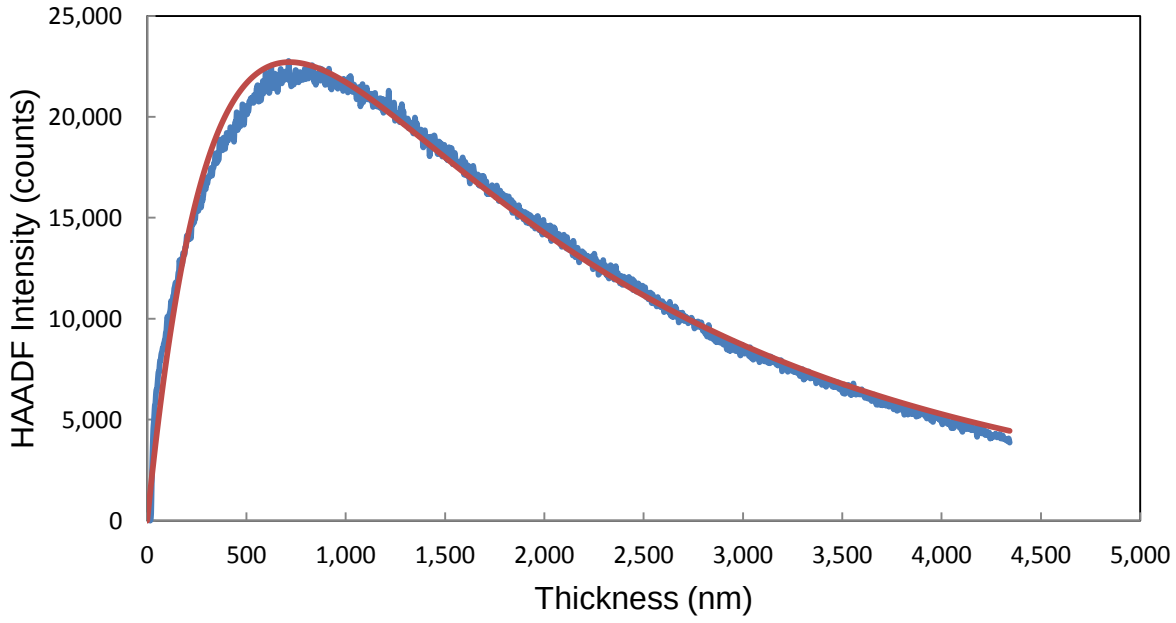

Figure 32: $LiTaO_3$ from Au sample, I_0 = 8.1x10^4 counts, fitting with K = 3.9x10^4 counts, and F = 2.5x10^{-3} nm^{-1}, μ = 5x10^{-4} nm^{-1}, initial ε = 6.0x10^{-4} nm^{-1}.

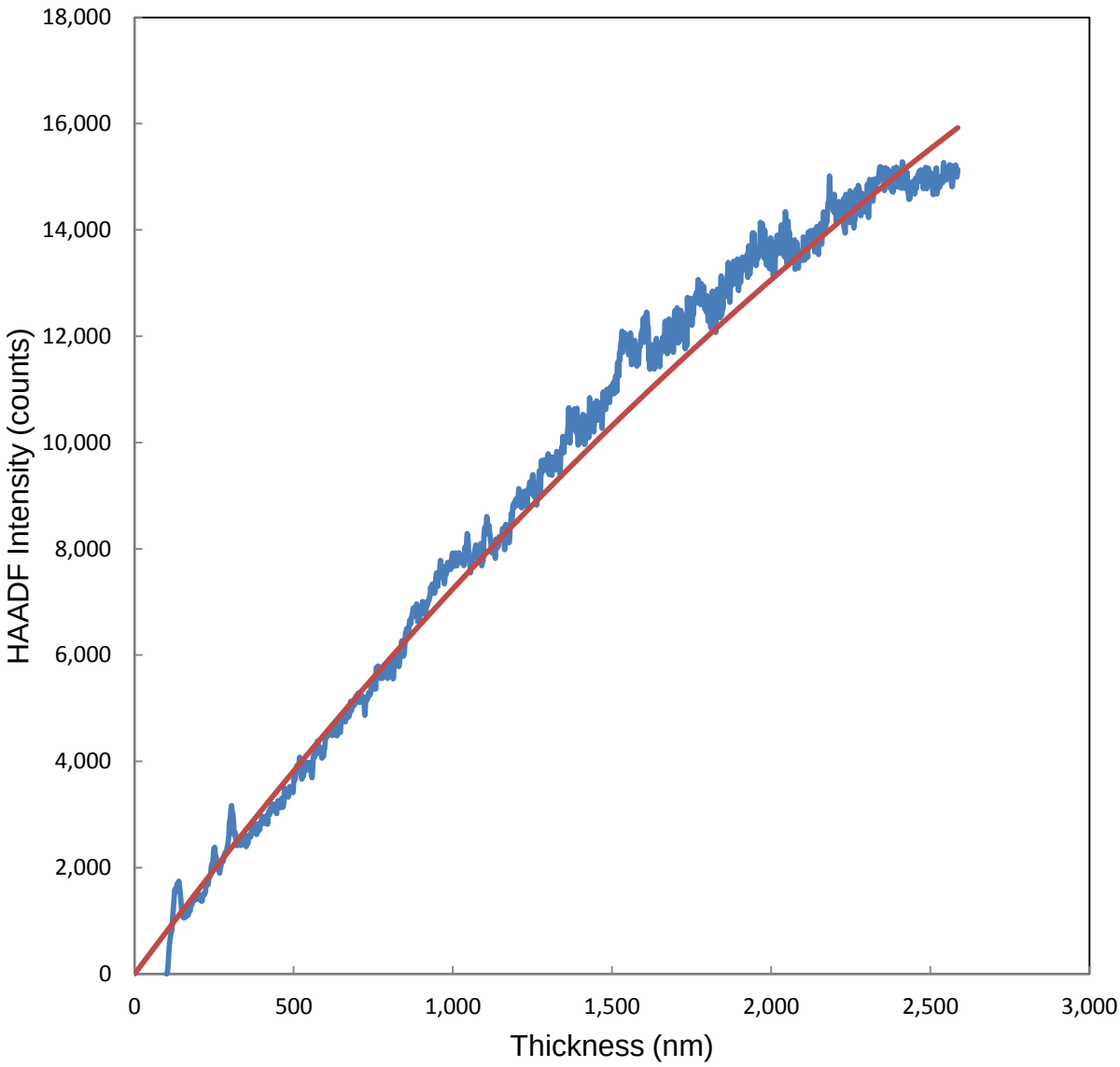

Figure 33: Al from W sample. I_0 = 8.1x10^4 counts, fitting with K = 3.67x10^4 counts, and F = 2.2x10^{-4} nm^{-1}, initial ε = 9.9x10^{-5} nm^{-1}.

For thin samples (up to 200 nm, for W, Pt, and Au up to 100 nm), the initial slopes, ε, are lower than the ε values listed in Table 1. For thick samples, fitting parameters include absorption parameters μ. Table 3 summarizes the fitting parameters for these wedge-shaped samples.

Table 3: Fitting parameters for wedge shaped samples.

Material	Z	K (Counts)	I_0 (Counts)	F (nm^{-1})	K/I_0	μ (nm^{-1})	ε (nm^{-1})
Al	13	$3.67x10^4$	$8.1x10^4$	$2.2x10^{-4}$	0.45		$9.9x10^{-5}$
Si	14	$2.25x10^4$	$5.6x10^4$	$2.5x10^{-4}$	0.40	$2.4x10^{-4}$	$1x10^{-4}$
Fe	26	$2.25x10^4$	$5.6x10^4$	$4x10^{-5}$	0.40	$8x10^{-4}$	$6.1x10^{-4}$
Cu	29	$5.0x10^4$	$6.2x10^4$	$2.1x10^{-4}$	0.81	$3.8x10^{-4}$	$1.1x10^{-3}$
W	74	$3.67x10^4$	$8.1x10^4$	$1.14x10^{-3}$	0.45	$1.37x10^{-3}$	$3x10^{-3}$
Pt	78	$2.25x10^4$	$5.6x10^4$	$8.8x10^{-4}$	0.40	$9.0x10^{-4}$	$3x10^{-3}$
Au	79	$2.8x10^4$	$8.1x10^4$	$2.2x10^{-2}$	0.35	$1x10^{-3}$	$1x10^{-3}$
SiO_2		$2.25x10^4$	$5.6x10^4$	$2x10^{-4}$	0.40		$5x10^{-5}$
AlN		$3.67x10^4$	$8.1x10^4$	$2.2x10^{-4}$	0.45		$6x10^{-5}$
$LiTaO_3$		$3.9x10^4$	$8.1x10^4$	$2.5x10^{-3}$	0.48	$5x10^{-4}$	$6x10^{-4}$

The initial measurements of sample thicknesses and the corresponding determination of values for ε were based on CBED data. While these data correctly yield the thickness of the crystalline Si, which has been used as a thickness reference for several other elements, the thickness of the crystalline Si does not represent the whole thickness of the sample, which is additionally influenced by surface amorphization in the Ga beam of the FIB system, as well as by Ga ion implantation (higher atomic number) at the surfaces. Therefore, the real thickness of the sample containing Si is underestimated. This results in too high values for epsilon, as the thickness is underestimated. This experimental error translates to all materials studied

in combination with Si as a thickness reference. The situation was avoided when wedge-shaped samples were studied here. The results indicate consistently lower values for epsilon, which are directly determined from the slope of the intensity increase if the HAADF detector as a function of increasing sample thickness. These values for the thickness calibration from wedge-shaped samples were used in the determination of nanoparticle volumes.

3.2. Measurements

3.2.1. Thickness/Volume of $Au_{0.5}Fe_{0.5}$ Nanoparticles on C Film

Au-Fe nanoparticles were studied with conventional TEM and HAADF STEM (Figure 34) in plane-view imaging. Usually, plane-view images only provide information on the lateral size and shape of nanoparticles. However, with the contrast calibrations we are now able to determine the height of each nanoparticle (and even the height distribution) from a single HAADF-STEM micrograph. The local thicknesses of nanoparticles (as shown in Figure 35) were measured yielding also the volume of each nanoparticle. The intensity/thickness ratio for the nanoparticles was calculated from the given composition $Au_{0.5}Fe_{0.5}$. Figure 35 shows the intensity across nanoparticles along the line scan.

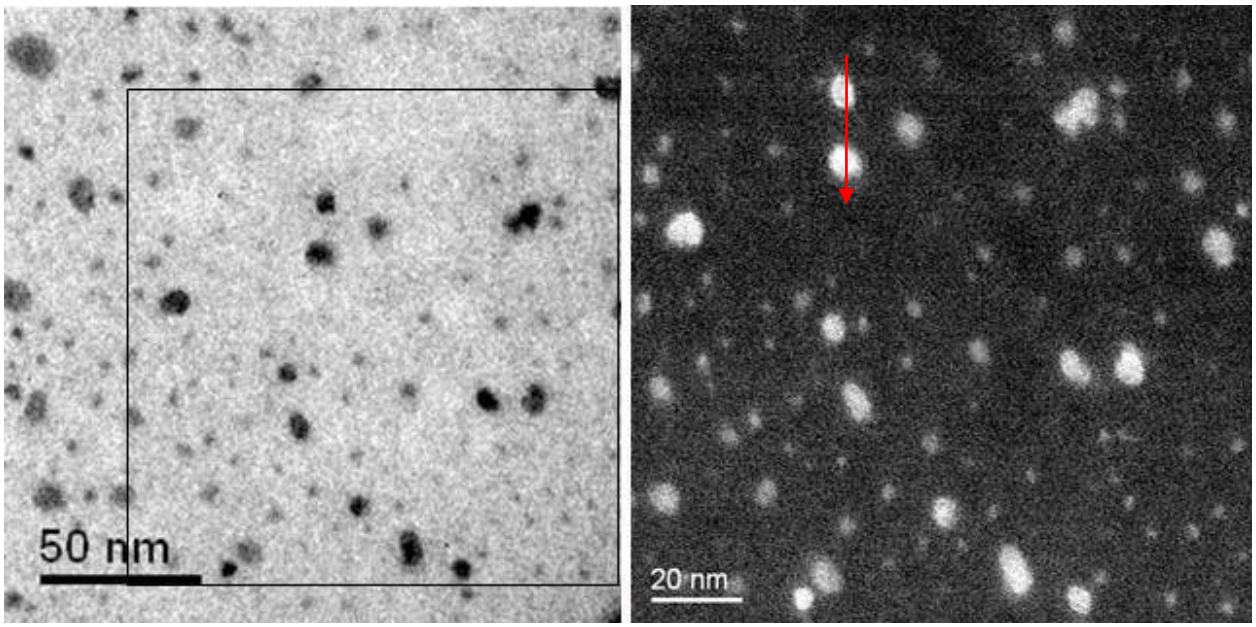

Figure 34: Conventional TEM (left) and STEM micrographs (right) of $Au_{0.5}Fe_{0.5}$ nanoparticles from a sample provided by Dr. Roldan of UCF's Physics Department [96]. The contrast of the STEM micrograph of the $Au_{0.5}Fe_{0.5}$ nanoparticles yields data on the thicknesses and volumes of individual nanoparticles (Figure 35).

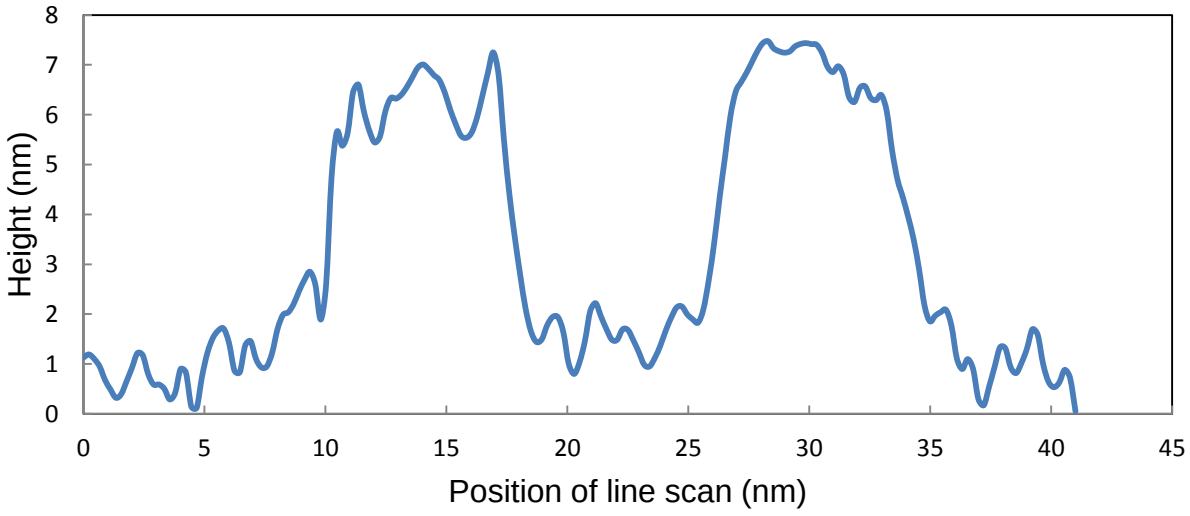

Figure 35: The heights of two nanoparticles along the linescan obtained from Figure 34 (right).

The total intensity for each particular nanoparticle has been measured by integrating the thickness over the area of the nanoparticle and by multiplying the result with 0.066 nm^2 (since 1 pixel at the magnification used has a lateral dimension of 0.257 nm). This yields a volume of (170±20) nm^3 for the nanoparticle in the top part of the line scan (Figure 34). For the second nanoparticle of this line scan, a volume of (260±20) nm^3 is measured. Similarly, volumes of other nanoparticles were determined. The average particle volume determined from all nanoparticles shown in Figure 34 is (66±20) nm^3. The corresponding particle size distributions for diameter, height, and volume are shown in Figure 36.

The HAADF-STEM measurements show that these Au-Fe nanoparticles have volumes of up to 300 nm^3. Nanoparticles with volumes as small as 30 nm^3 were clearly identified. They can be distinguished from HAADF signal variations caused by different carbon film thicknesses or polymeric residues at the surfaces of the Au-Fe nanoparticles. The measurement of the thicknesses of the nanoparticles is important as the change in the thickness as well as the overall size of nanoparticles may be responsible for changes in the catalytic properties [105], in luminescence-center-mediated excitation [106], or for other applications where particle sizes have a significant influence on properties. The statistics of the distribution of diameters, heights, and volumes is shown in Figure 36.

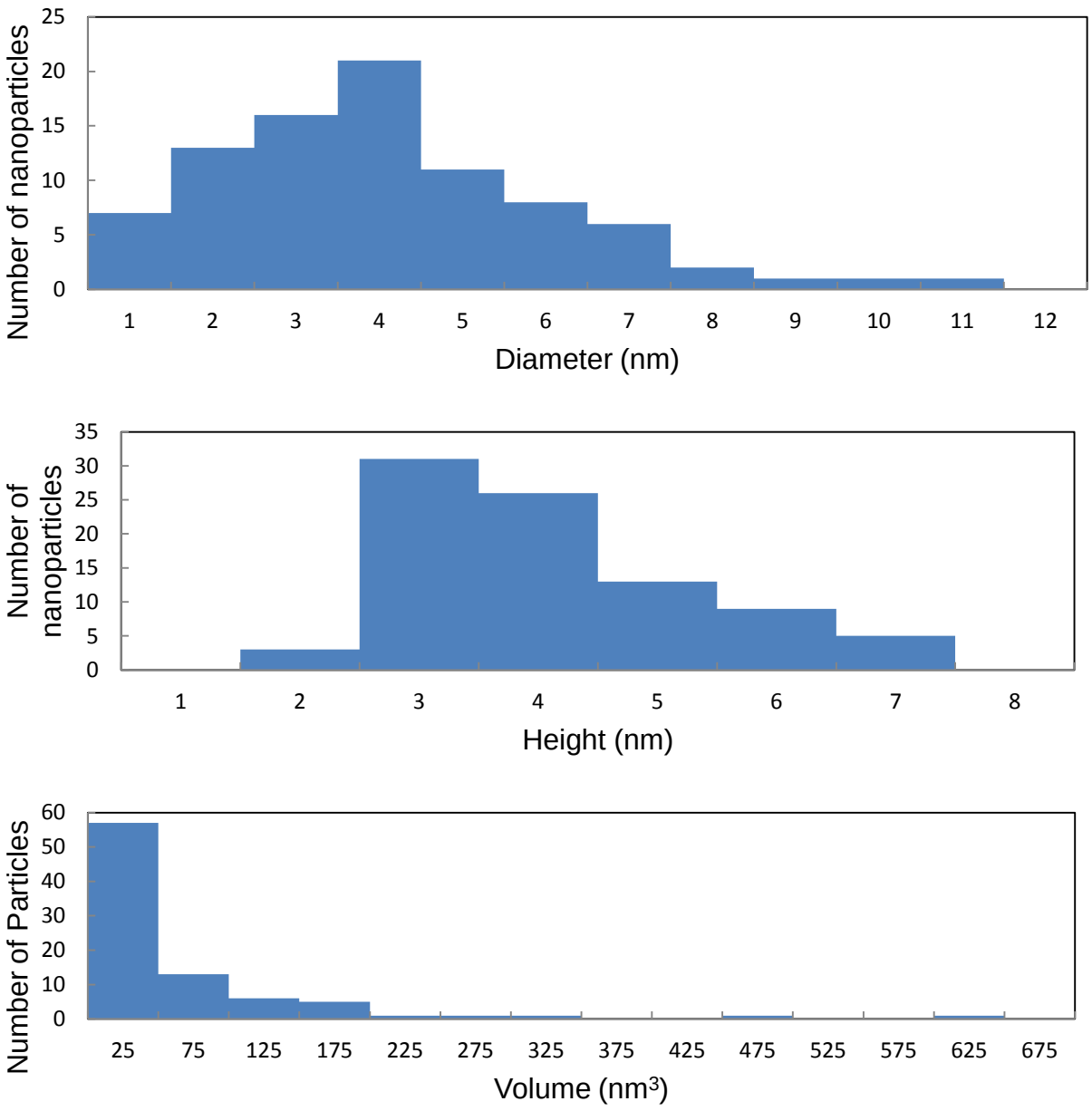

Figure 36: Distribution statistics of diameters, heights, and volumes of 87 $Au_{0.5}Fe_{0.5}$ nanoparticles shown in figure 34. Diameter distribution (top), Average 4.0 nm, Median 3.6 nm, Maximum 10.6 nm, Minimum 1.5 nm, Standard deviation 2.0 nm. Height distribution (middle), Average 4.1 nm, Median 3.7 nm, Maximum 7.0 nm, Minimum 2.3 nm, Standard deviation 1.4 nm. Volume (bottom) distribution, Average 66.4 nm^3, Median 24.0 nm^3, Maximum 633.0 nm^3, Minimum 4.0 nm^3, Standard deviation 100.6 nm^3.

3.2.2. The Porosities of Porous Si Samples Determined by HAADF

The following two figures (Figure 37 & Figure 38) are from samples provided by TriQuint Semiconductors. They contain several layers, including SiO_2 on top of a porous Si layer on top of a silicon single crystalline substrate [107].

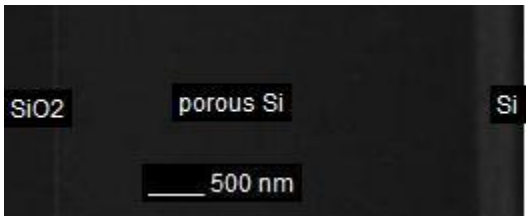

Figure 37: Micrograph of porous Si by HAADF (samples provided by TriQuint semiconductors).

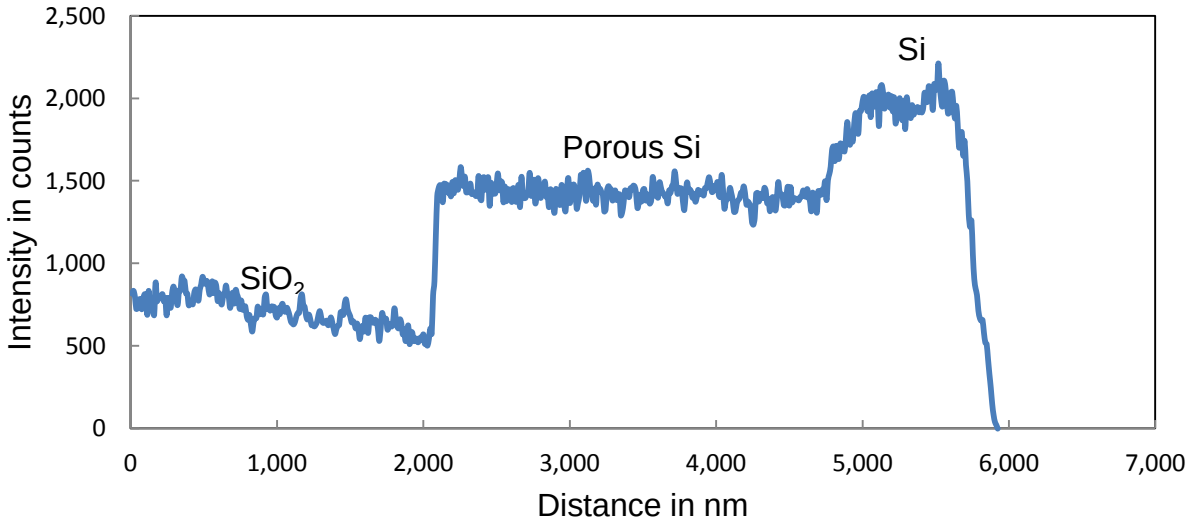

Figure 38: HAADF intensity along a line perpendicular to the interfaces in Figure 37

The background intensity is about $1.5x10^3$ counts/pixel, the Si intensity is about $2.0x10^3$ ($3.5x10^3$ – $1.5x10^3$) counts/pixel, and the intensity of porous Si is about $1.2x10^3$ ($2.7x10^3$ – $1.5x10^3$) counts/pixel. Therefore, the porosity of Si is about 40% (1 – $1.2x10^3$ / $2.0x10^3$). The absolute thickness at Si <110> / porous Si interface is about 224 nm, and the absolute thickness at SiO_2 / porous Si interface is about 201 nm. The thickness of the sample is decreased from SiO_2 to porous Si, and to Si <110>. However, the porosity is not changed in porous Si.

3.2.3. Composition Profile of Pt/Fe Nanomultilayers

A second quantitative method of data extraction from the HAADF STEM signal is described below. Here with known sample thickness the composition of a binary alloy can be determined from a single HAADF-STEM micrograph.

In order to determine compositions of a material with known TEM sample thickness, a [Pt(28 nm) / Fe(22 nm)] multilayered system was studied. After 10 minutes and 20 minutes of heat treatment at 350 °C, inter diffusion of Fe into the Pt layer and Pt diffusion into the Fe layer can be observed (Figure 39) [96-98]. The quantitative measurement of the compositions of the layers after these heat treatments is difficult with Energy-Dispersive X-ray (EDX) analysis (where secondary excitation near the electron beam significantly influences the measured Fe / Pt signal ratio. With electron energy loss spectroscopy (EELS) this secondary excitation signal can be avoided, however, the Pt M-edge, the only useful edge for quantification, is at very high energy losses with a very small signal. With HAADF-STEM the Pt and Fe contrast was

calibrated using as-deposited Pt-Fe multilayers as references. In these as-deposited samples inter diffusion is not occurring (Figure 39, left). The data evaluation as shown in the line scan in Figure 40 [108] shows that Pt diffuses into the Fe layer, while diffusion of Fe into the center of the Pt layer is limited.

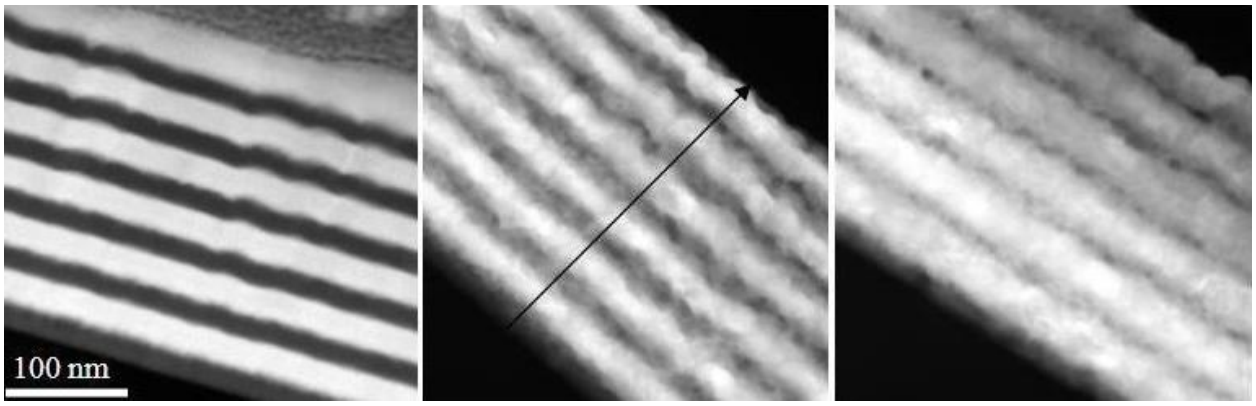

Figure 39: HAADF STEM micrographs of a multilayer system on Si and SiO_2 with six Pt (28 nm) and six Fe (22 nm) layers. Left: as deposited, center: after 10 minute heat treatment at 350 °C, right: after 20 minute heat treatment at 350 °C.

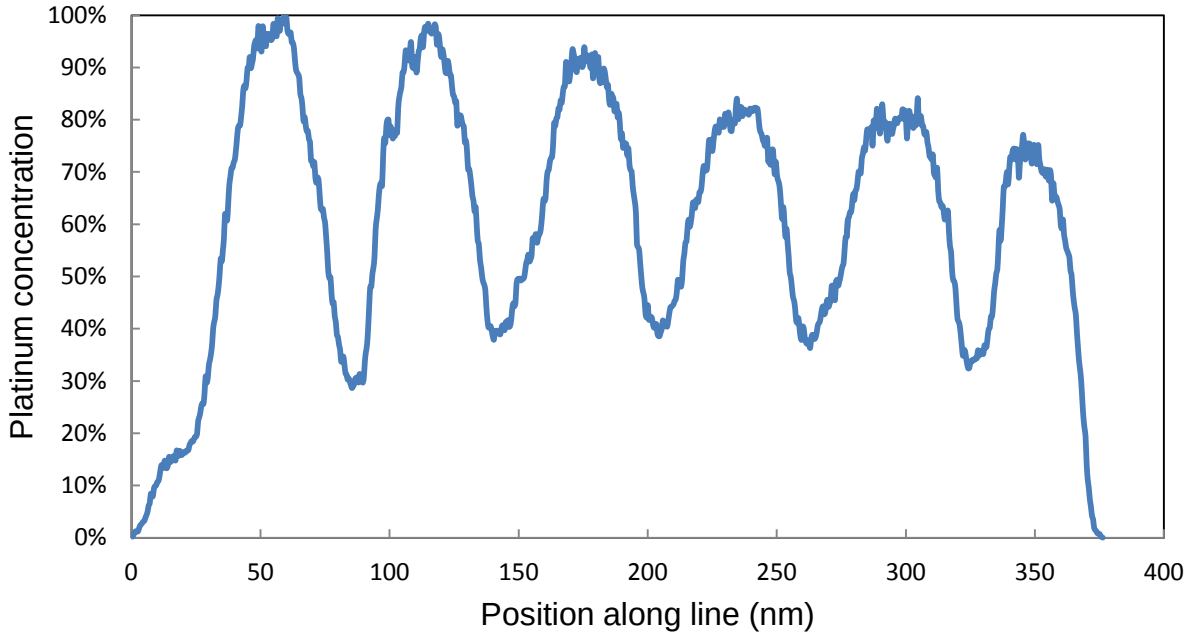

Figure 40: Line scan of the Pt composition across the layers after heat treatment at 350 °C for 10 min.

A similar study has been done by Kaiser et al. [109] involving inter-diffusion through diluted alloys, through $L1_2$-ordered alloys, and in the final $L1_0$-ordered film.

These heat treatments [109] were however done at significantly higher temperatures than those used by Dr. Bo Yao [97].

3.2.4. Volume of Pt and Ag Nanoparticles

Samples provided by the group of Dr. Roldan in Physics at UCF were studied with HAADF-STEM. These samples consisted of Pt nanoparticles on Si substrates. After FIB cutting of cross sections the sample was viewed edge-on or tilted in the TEM. A detailed discussion of sample preparation is given in Dr. Ono's papers [110-112]. The volume of each Pt nanoparticle was measured by HAADF. Typical TEM micrograph is shown in Figure 41. Statistics was presented in figure 42. The sample is tilted with respect to the surface of the Si crystal on which the nanoparticles are deposited. Therefore the distribution of nanoparticles on the cross-section becomes visible. However, this introduces also a strong change in background contrast, as the nanoparticles are lying between the tilted (in projection) surface of Si and the carbon coating that was applied before FIB cutting. The Si substrate introduces a higher HAADF-signal than the carbon coating. As more Si material in traversed by the electron beam in the lower part of the micrograph than at the top, the HAADF-intensity of the background signal decreases from bottom to top.

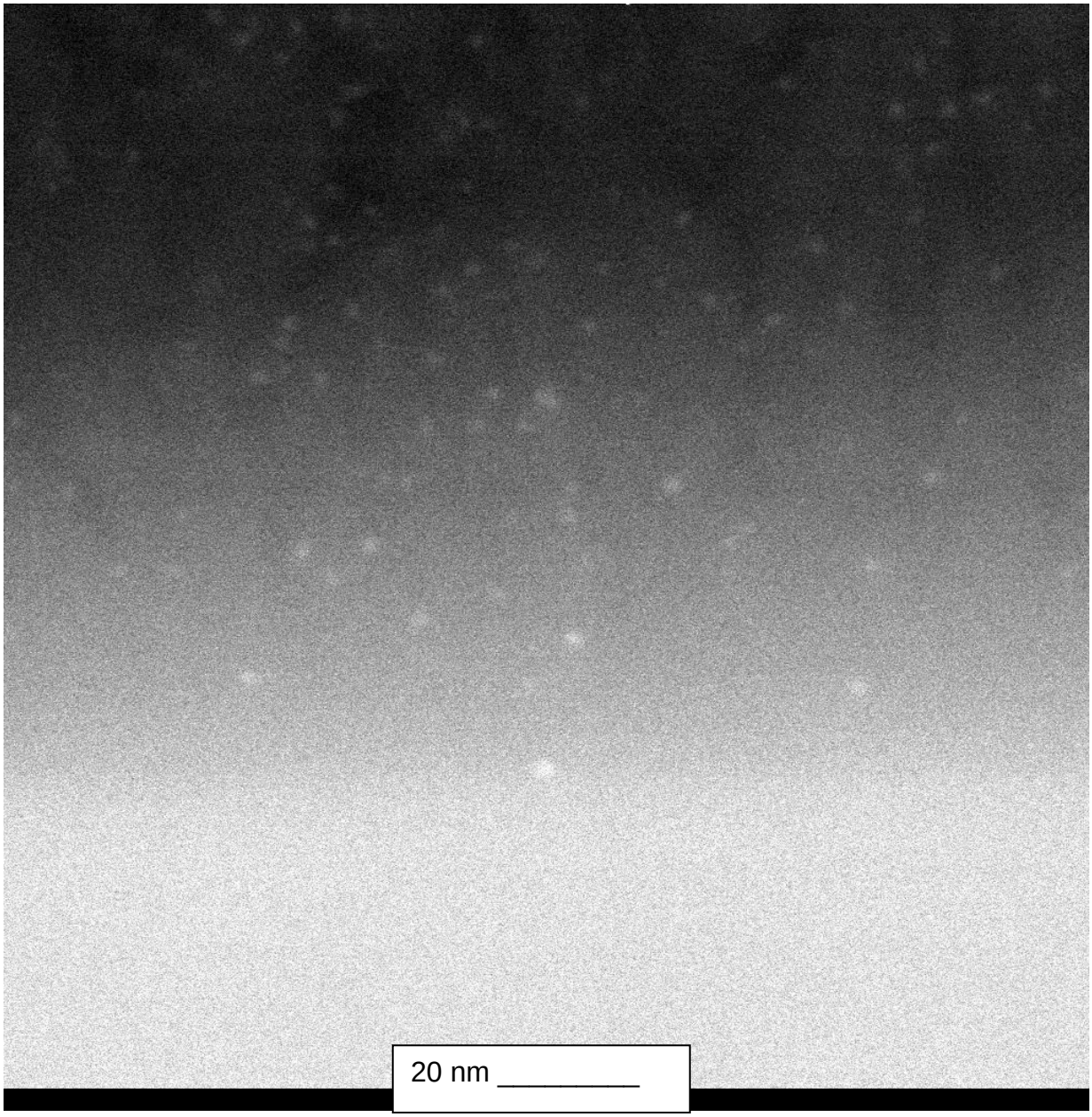

Figure 41: Pt nanopaticles of samples provided by Professor Roldan. The background contrast is not uniform as the sample is tilted.

In the micrographs of Figures 41 and 42 there are 66 pixels for 10 nm. The pixel size is therefore 0.15 nm / pixel. The limits in size to be analyzed is 1 pixel x 1 pixel area,

i.e. 0.15 nm x 0.15 nm = 0.023 nm^2. One HAADF-STEM detector count corresponds to a thickness of 0.014 nm for Pt. However, it has to be taken into account that the background noise level of the HAADF-detector is about $(1.5x10^3)^{½}$ counts. A signal noise of about ±40 counts in one pixel would correspond to a thickness error of ±0.34 nm for an incident beam intensity on the detector of $5.7x10^4$ counts / pixel, and 0.207% per nm thickness. Obviously, this is larger than the size of a Pt atom. With a pixel area of 0.023 nm^2 a volume error of ±0.008 nm^3 is determined as the minimum volume of Pt detectable for the contrast-brightness setting used here. This error in volume measurement is of the same size as the volume for a single Pt atom of about 0.016 nm^3, therefore single atom imaging (counting) is not possible with the contrast brightness setting used here.

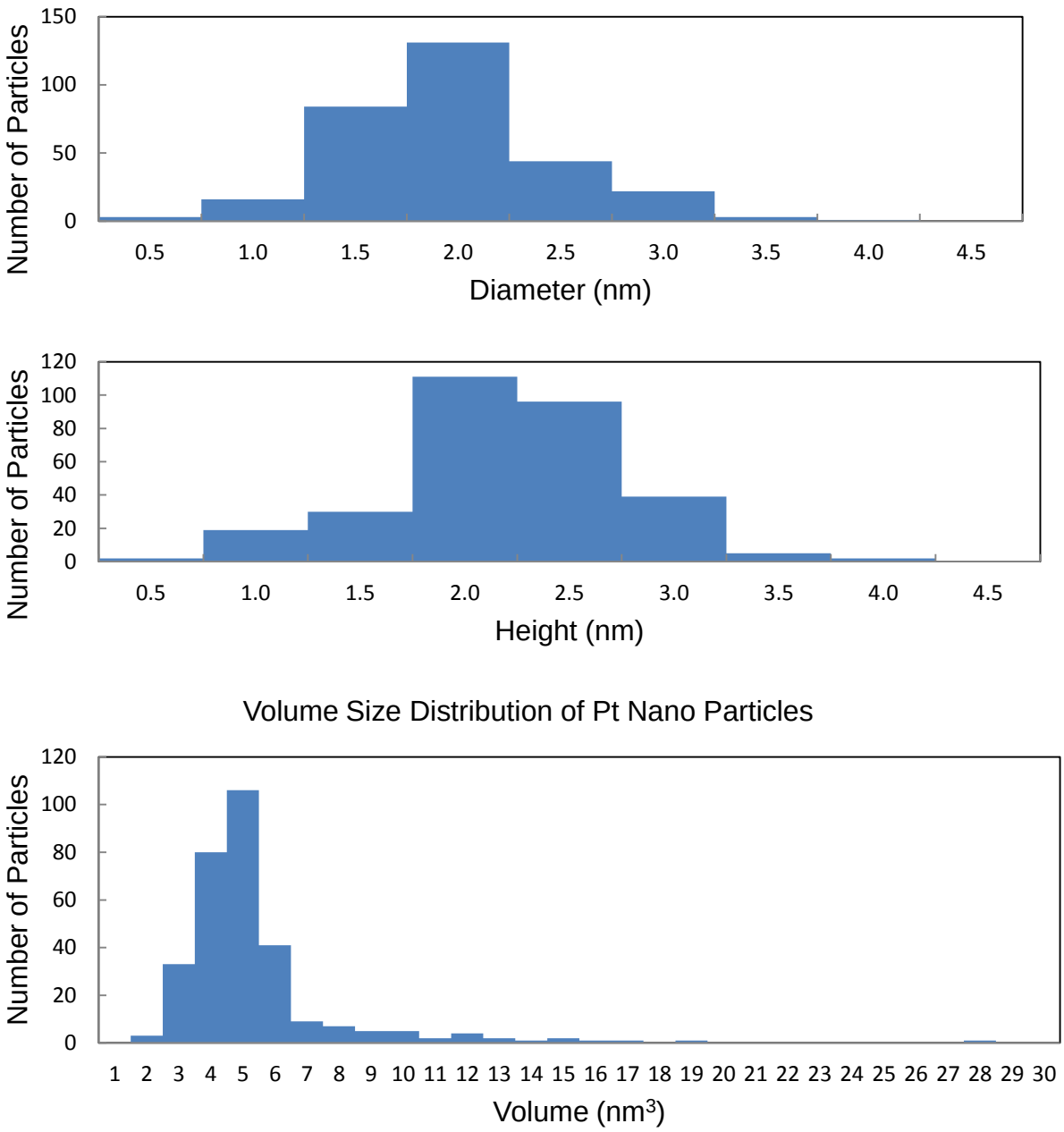

Figure 42: Distribution statistics of diameters, heights, and volumes of 304 Pt nanoparticles shown in figure 41. Diameter distribution (top), Average 2.0 nm, Median 2.0 nm, Maximum 4.0 nm, Minimum 0.5 nm, Standard deviation 0.5 nm. Height distribution (middle), Average 2.2 nm, Median 2.0 nm, Maximum 4.0 nm, Minimum 0.5 nm, Standard deviation 0.6 nm. Volume (bottom) distribution, Average 5.4 nm^3, Median 4.8 nm^3, Maximum 28.5 nm^3, Minimum 2.0 nm^3, Standard deviation 2.7 nm^3.

The average nanoparticle volume is 5.4 nm^3, median volume is 4.8 nm^3, the maximum volume found is 28.5 nm^3, the minimum volume found is 2.0 nm^3, the minimum volume of a nanoparticle that can be identified is 0.5 nm^3, the number of particles analized is 304, and the standard deviation is 2.7 nm^3. For the contrast calibration data (ε) from the wedge-shaped calibration standards are used, as the data from table 1 in this work underestimate the sample thickness as explained above.

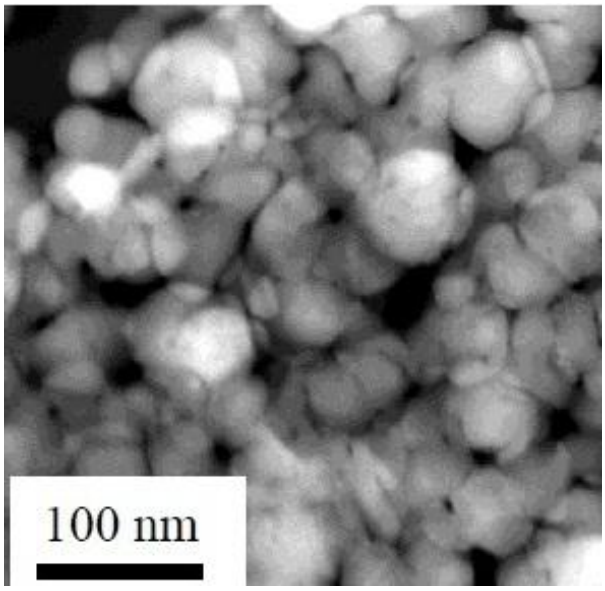

Figure 43: Plan view HAADF-STEM of Ag nanoparticles in a SU8 polymer prepared by 6 hours of electroless deposition using [Ag+] = 5.6 mM in the presence of gum arabic [108].

A second set of samples with silver nanoparticles on a surface was studied HAADF-STEM. In Figure 43 a “plan view HAADF-STEM image of” Ag particles on a SU8 polymer is shown. Silver was deposited in an electroless deposition process using Au nanoparticles as nucleation sites on the surface of the polymer. These samples were

provided by the group of Dr. Kuebler in Chemistry at UCF. The average thickness of the Ag layer is 45 nm with a standard deviation of 18 nm. This high value for the standard deviation reflects the granular structure of the Ag layer, which is composed of individual nanoscale grains. Some Ag grains are on top of each other while other areas of the polymer between Ag nanoparticles are not covered by silver. The average particle volume was determined to be $(6.5\pm9)x10^3$ nm^3, yielding an average particle diameter of 50 nm in all three dimensions While the lateral extension of each nanoparticle is clearly visible in TEM, the HAADF-STEM method allowed to determine the thickness of the Ag layer (and locally of individual Ag grains). The measured thicknesses after intensity calibration of the HAADF-STEM signal are consistent with cross sectional images.

3.2.5. Thickness as a Function of Sample Tilt

For a silicon sample thickness measurements by HAADF as a function of sample tilt in STEM are tested. The theoretic thickness is calculated and compared with experimental measurements. Figure 1 shows the HAADF images for different degrees of sample tilt.

Figure 44 shows the thickness both measured and calculated as a function of degree of tilt of silicon. Thickness (nm) stands for measured, and cal t (nm) stands for calculated theoretically / geometrically.

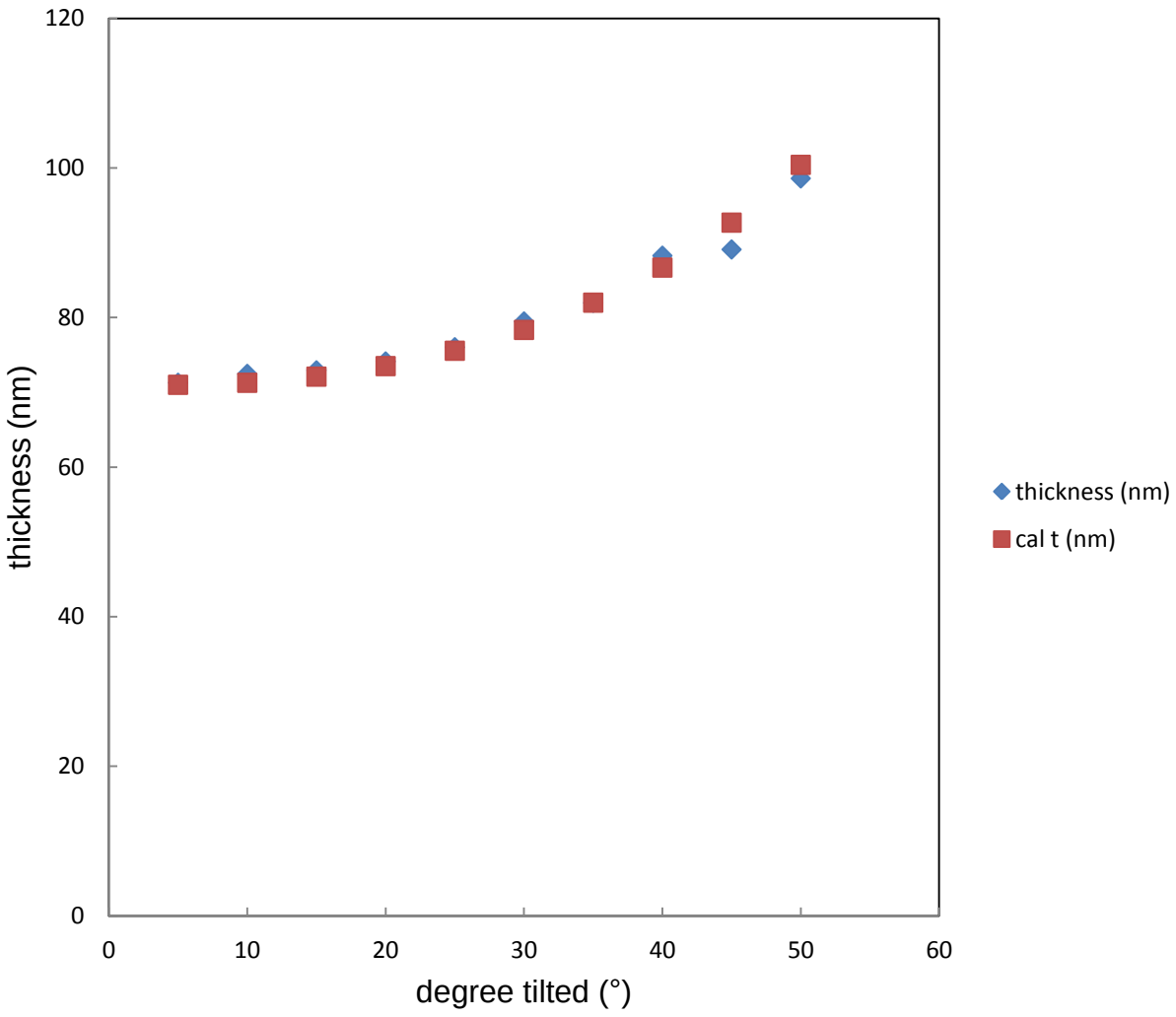

Figure 44: Thickness both measured by HAADF-STEM and calculated as a function of degree (°) of tilt. Center point is referenced.

Figure 45 shows the measurement errors as a ratio of calculated thickness to measured thickness as a function of degree of tilt of Silicon. Since the differences between calculated and measured values are within ±4%, the measurement method appears acceptable.

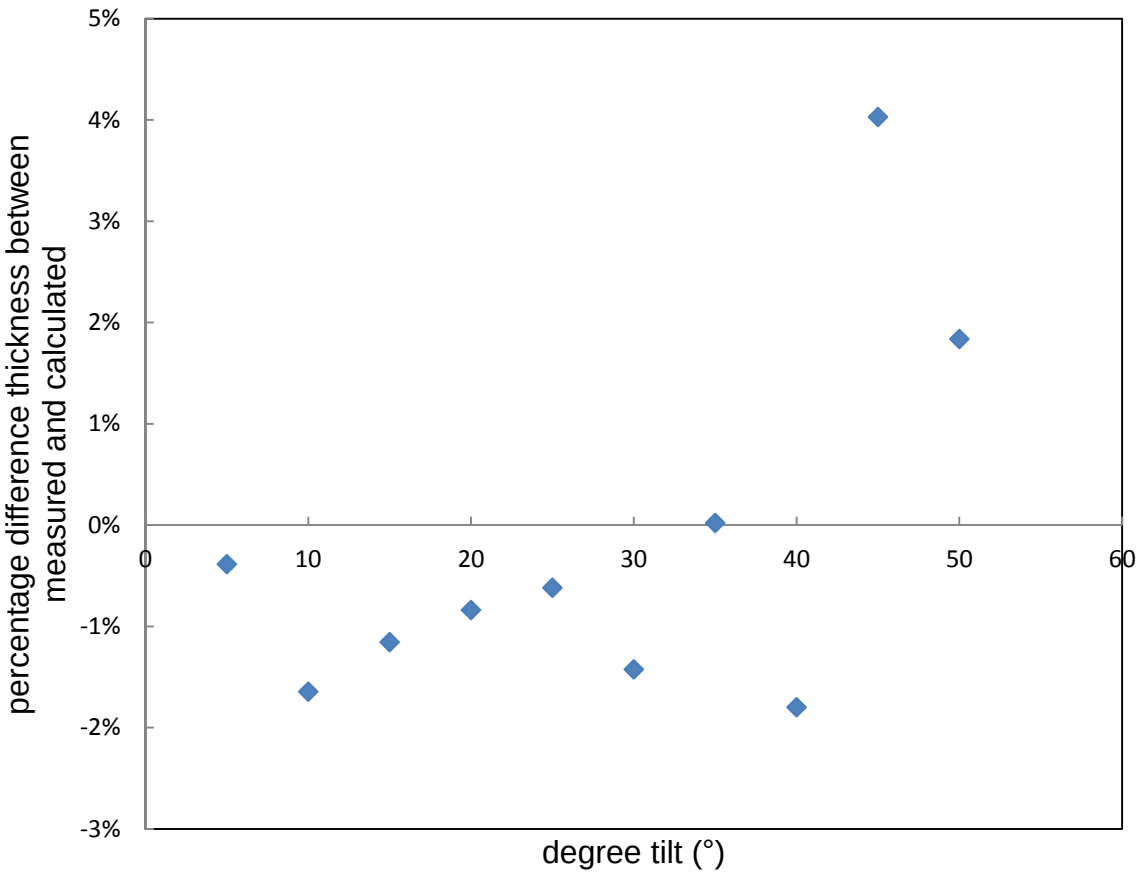

Figure 45: Error as a function of tilt.

3.3. Simulations

3.3.1. HAADF-STEM Intensity vs. Thickness Simulation

Simulation using the C code by Dr. Kirkland [53] is done for aluminum, silver, platinum, and gold, <100>. This is a “group of programs referred to as the TEMSIM package (for” conventional “and scanning Transmission Electron Microscope image SIMulation)”. The basic multislice simulation “steps are split into a small number of separate programs with the output of one program being used as the input for the next

program". The projected atomic potential of each "two dimensional slice through the specimen" is calculated in one program. These projected potentials are then used in the contrast simulation. The STEM probe parameters are as following: V_0 = 300 kV, C_s = 1.2 mm, df = 57 nm. The detector range used in the simulation is ranging from 56 mrad to 246 mrad. The following figures show the fraction of electrons scattered into this 56 mrad – 246 mrad angular intervals as a function of aluminum thickness. In the experiments a similar angular range from 53 mrad to 230 mrad was used for the 80 mm camera length set up at the Tecnai F30 microscope. In the following figures STDEV stands for standard deviation. The statistical variations of intensities are results from individual 24 points simulations along a line.

Figure 47 shows the intensity as a function of Al sample thickness. For the simulations a <100> orientation was used for the incident beam direction.

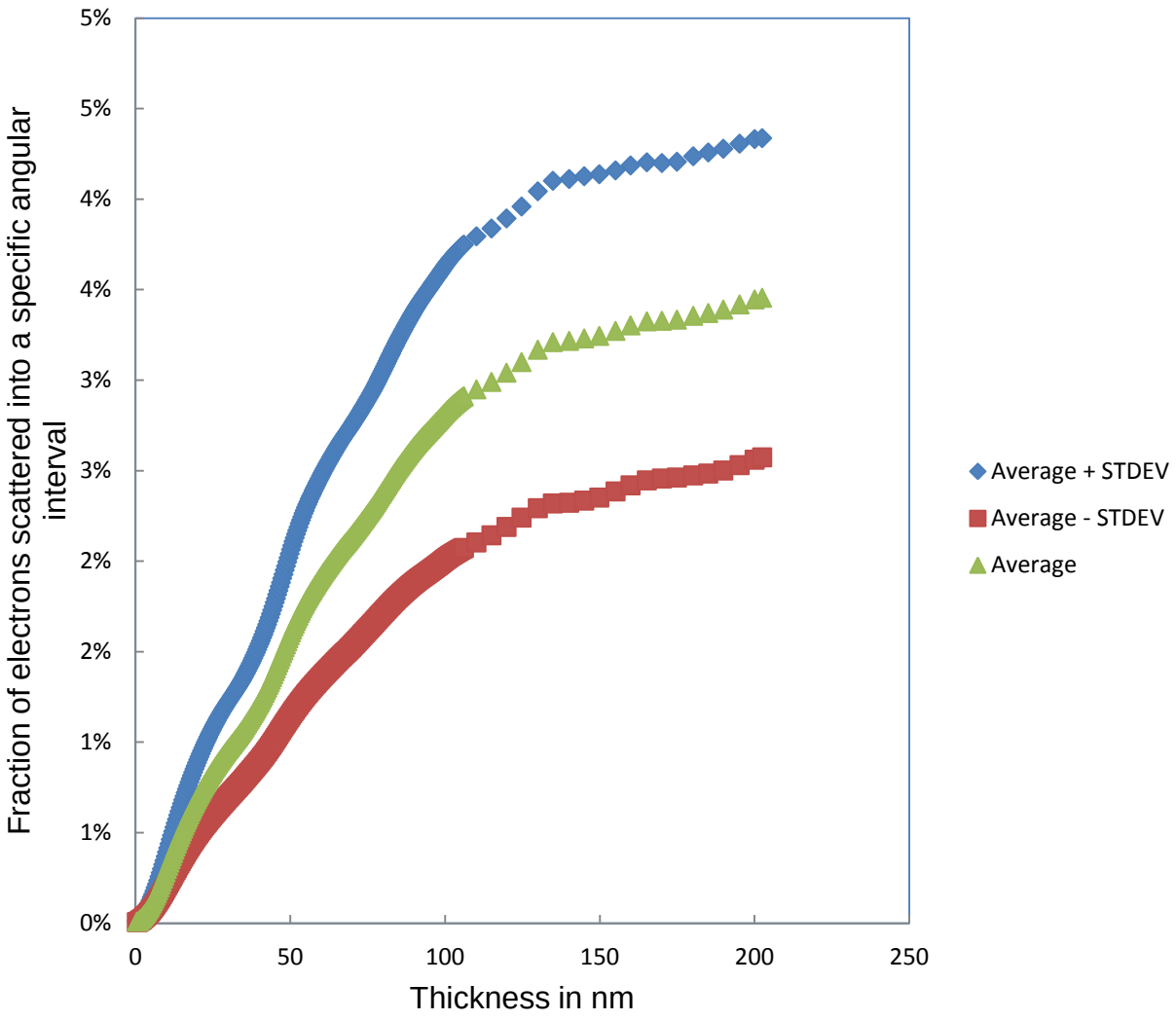

Figure 46: Simulated HAADF-STEM intensity vs. aluminium <100> thickness.

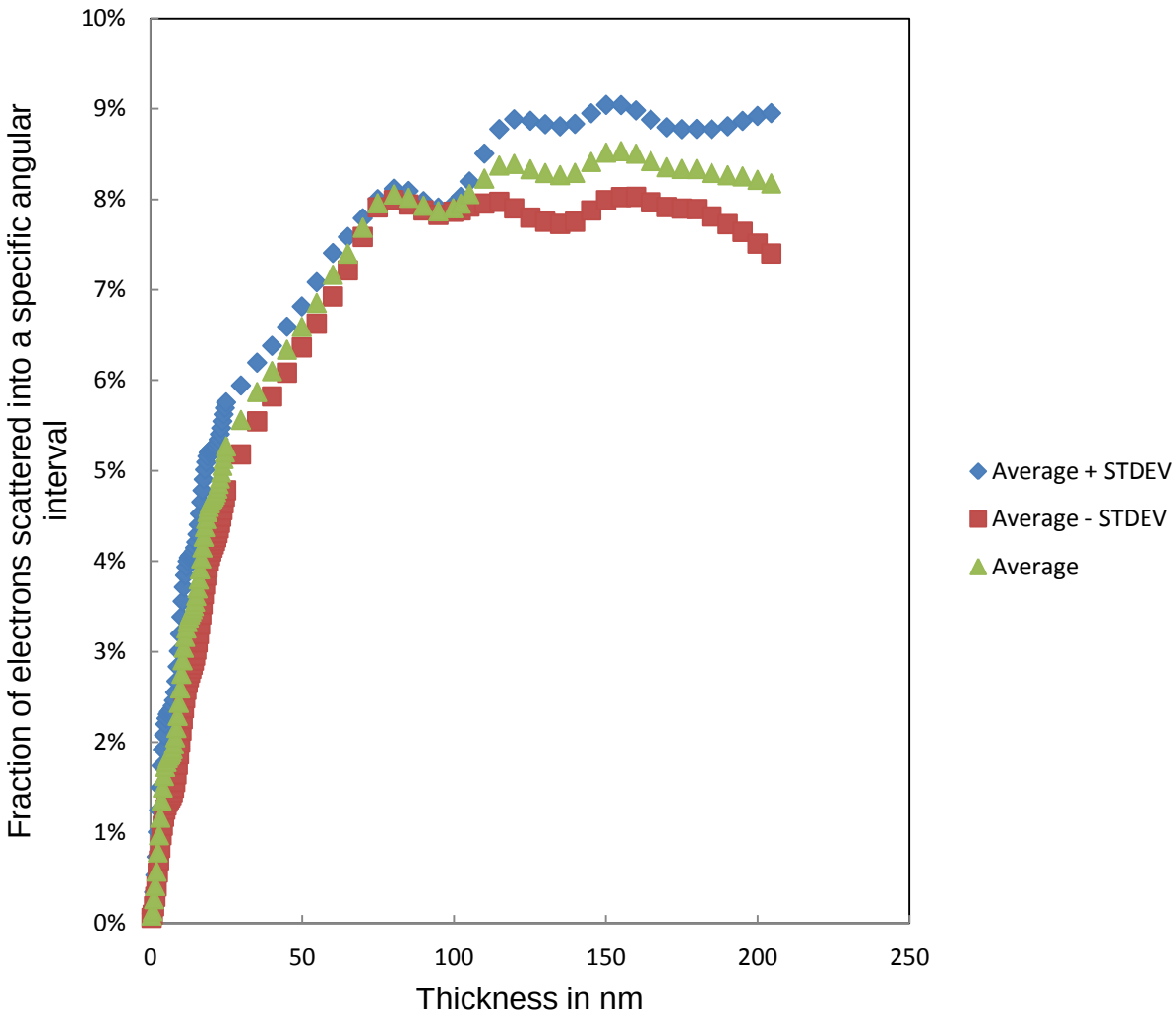

Figure 47: Simulated HAADF-STEM intensity vs. silver <100> thickness.

One important aspect of these simulations are different intensities at different beam positions for the same sample thickness as represented by the standard deviation. This is caused by different scattering contributions in case of on-column beam (high intensity) and off-column beam position (low intensity). Additionally, some weak modulations of the intensity with increasing sample thickness are seen, they are caused by dynamic (multiple) coherent scattering.

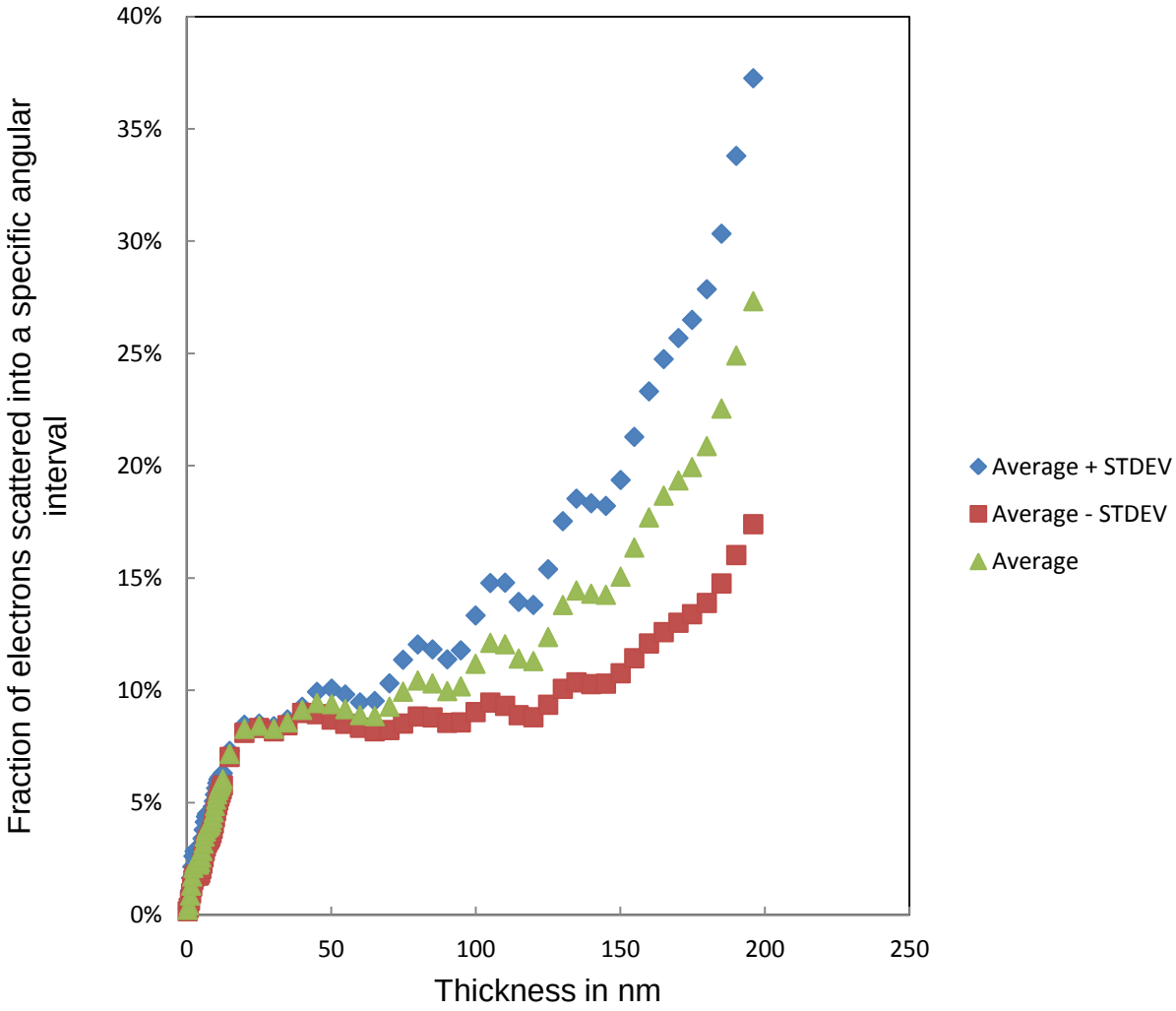

Figure 48: Simulated HAADF-STEM intensity vs. platinum <100> thickness.

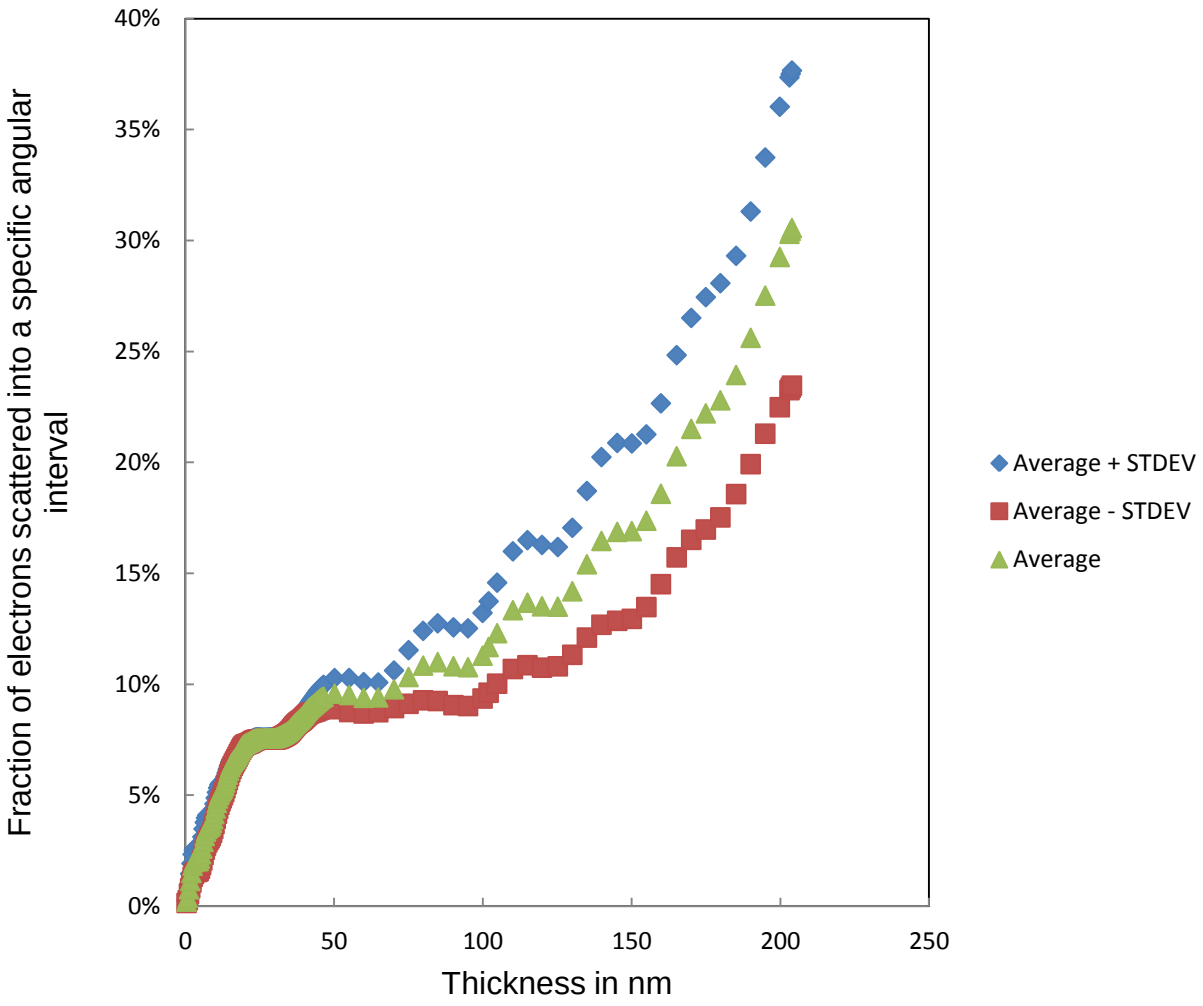

Figure 49: Simulated HAADF-STEM intensity vs. gold <100> thickness line 1 scan from position (0, 12) to (0, 5) in the projected crystal lattice. The vectors are the initial and final data points.

For Aluminum, the intensity is increased as thickness increasing. However, when sample gets thicker, the nonlinearity becomes obvious. This is especially more significant for silver. For Platinum, the simulations break down after 50 nm of thickness. For gold, the maximum is reached at about 70 nm.

3.3.2. 1-D Simulation

Normally, the simulated HAADF intensity statistics should be sampled on each pixel of the 2-D area of pixel map. However, this will come at the cost of a huge CPU time because the more data point the more calculations. A more efficient way is to simulate the HAADF intensity statistics sampled for pixels on a line scan instead of a whole sample area. However, effects on the simulated HAADF intensity statistics due to sampling on different line scan have to be evaluated. To answer this question, the simulated HAADF intensity statistics are done for three different line scan directions. Simulations using Dr. Kirkland's C code are done on gold, <100>. STEM probe parameters are as following: V_0 = 300 kV, C_s = 1.2 mm, df = 57 nm. The detector range is from 56 mrad to 246 mrad, compatible to the detector range used in the experiments. The following figures show the results for the fractions of electrons scattered into the 56 mrad - 246 mrad angular intervals as a function of thickness, where STDEV stands for standard deviation. The statistics are results from 24 points of a line scan along a (non-crystallographic) direction in the model crystal. The STDEV stands for standard deviation in statistics. To compare the independency of the line scans, three random line scan directions are used. To clarify the individual development of HAADF intensity as a function of sample thickness three separate figures are shown. These three figures represent different / independent line scans.

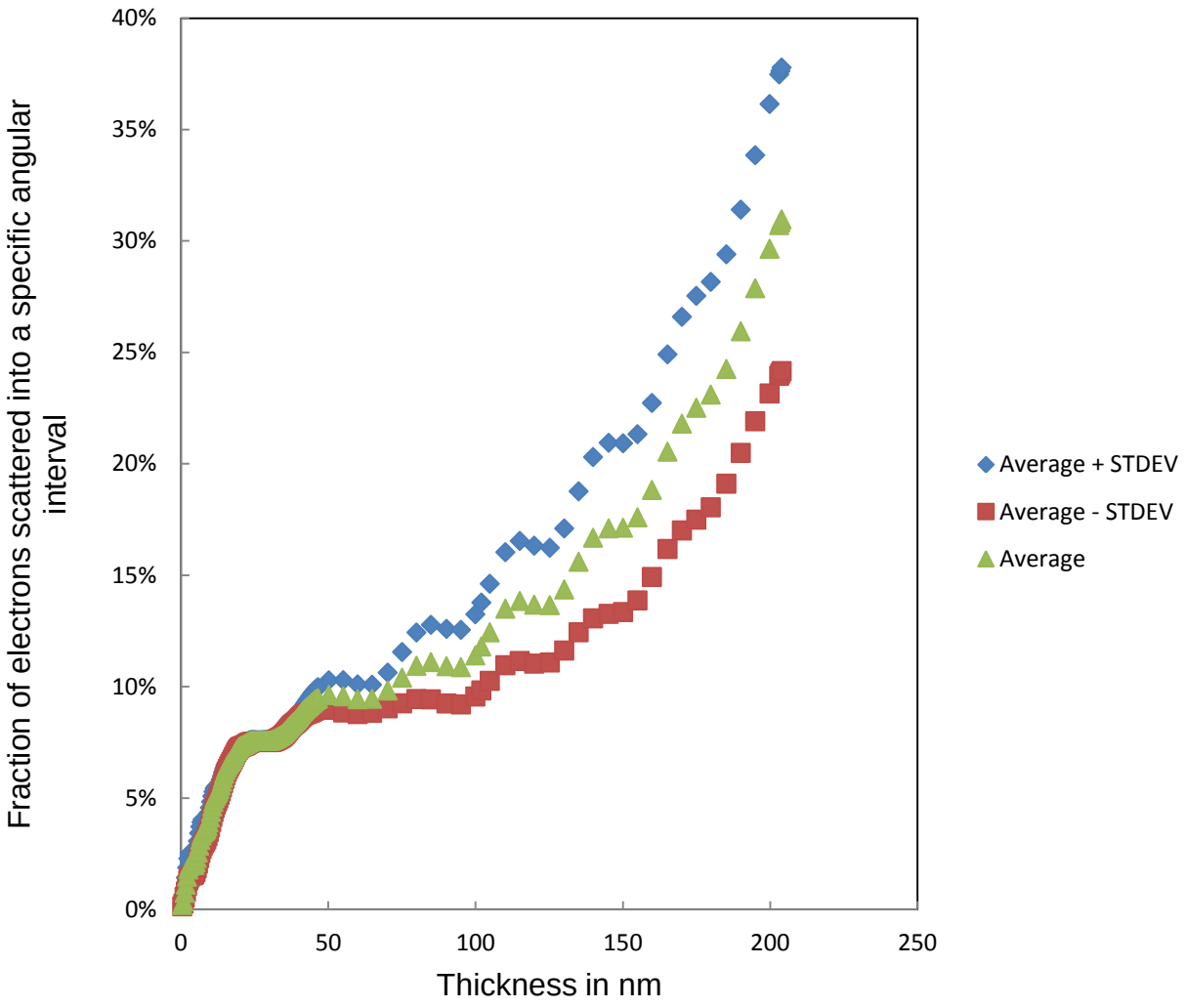

Figure 50: Simulated HAADF-STEM intensity vs. gold <100> thickness line 2 scan from (2, 19) to (3, 8).

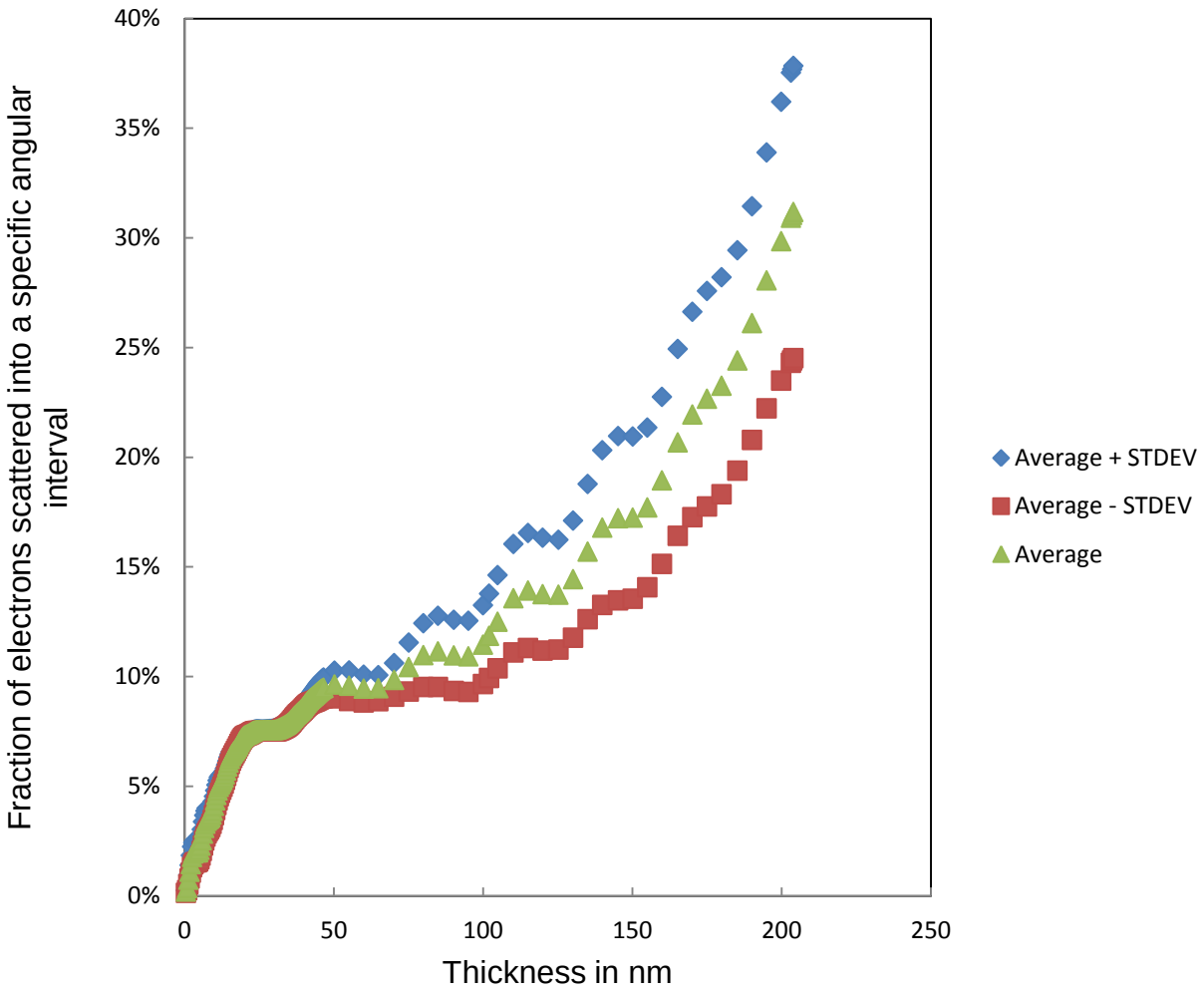

Figure 51: Simulated HAADF-STEM intensity vs. gold <100> thickness line 3 scan from (1, 11) to (6,1).

The following figures show the ratios of the simulated HAADF intensity between two different line scans.

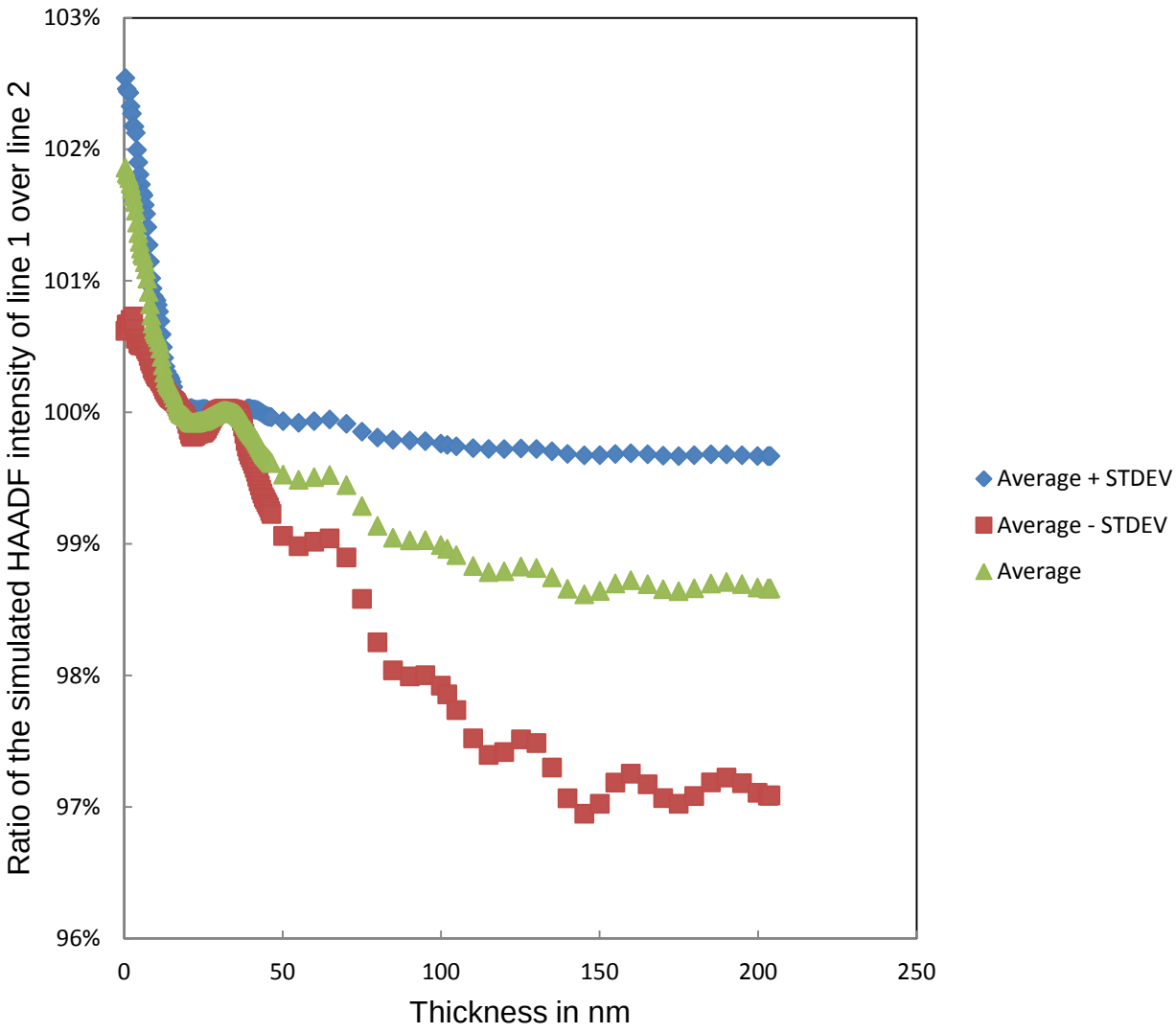

Figure 52: Intensity ratio of line 1 over line 2 for gold <100>.

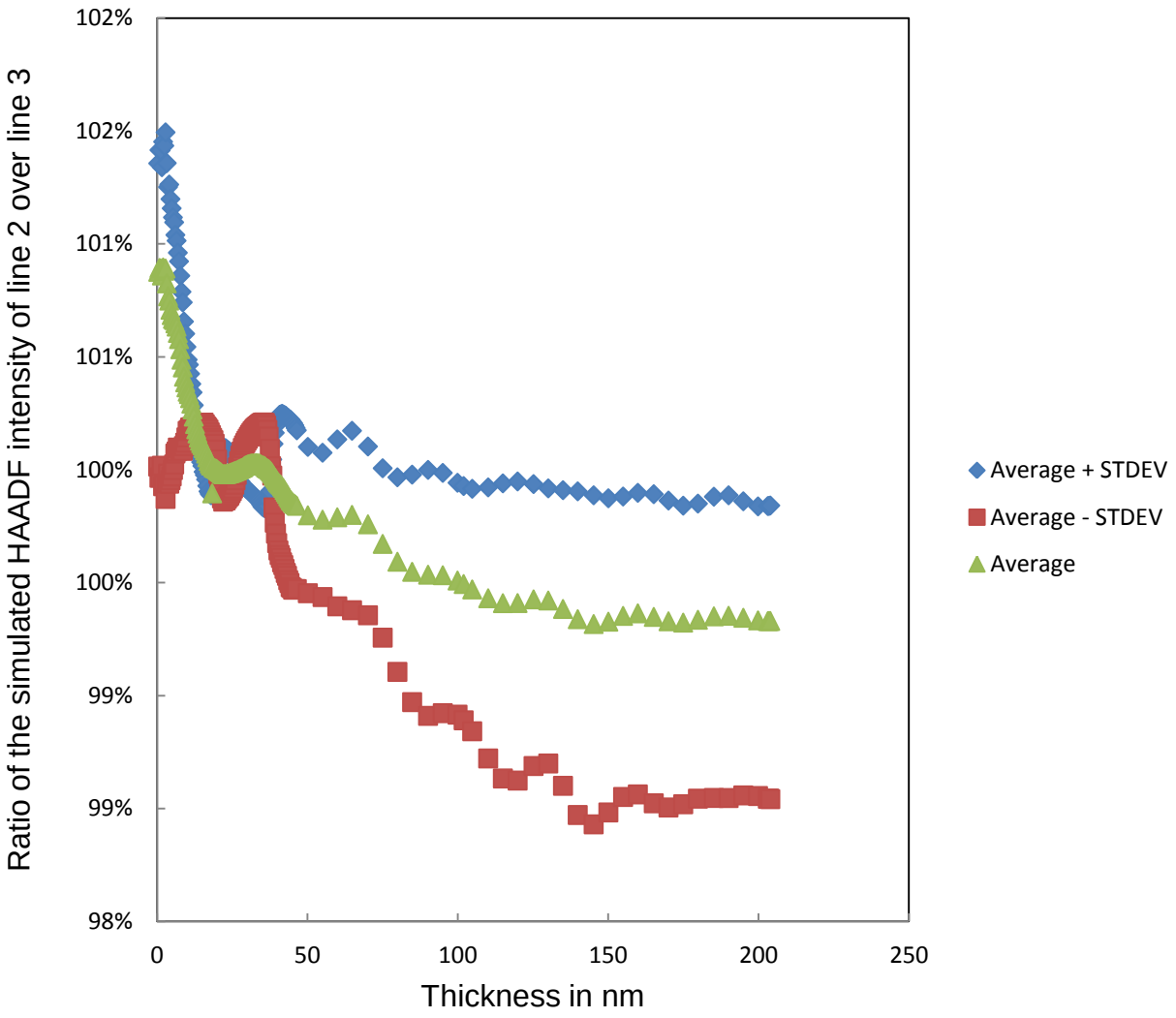

Figure 53: Intensity ratio of line 2 over line 3 for gold <100>.

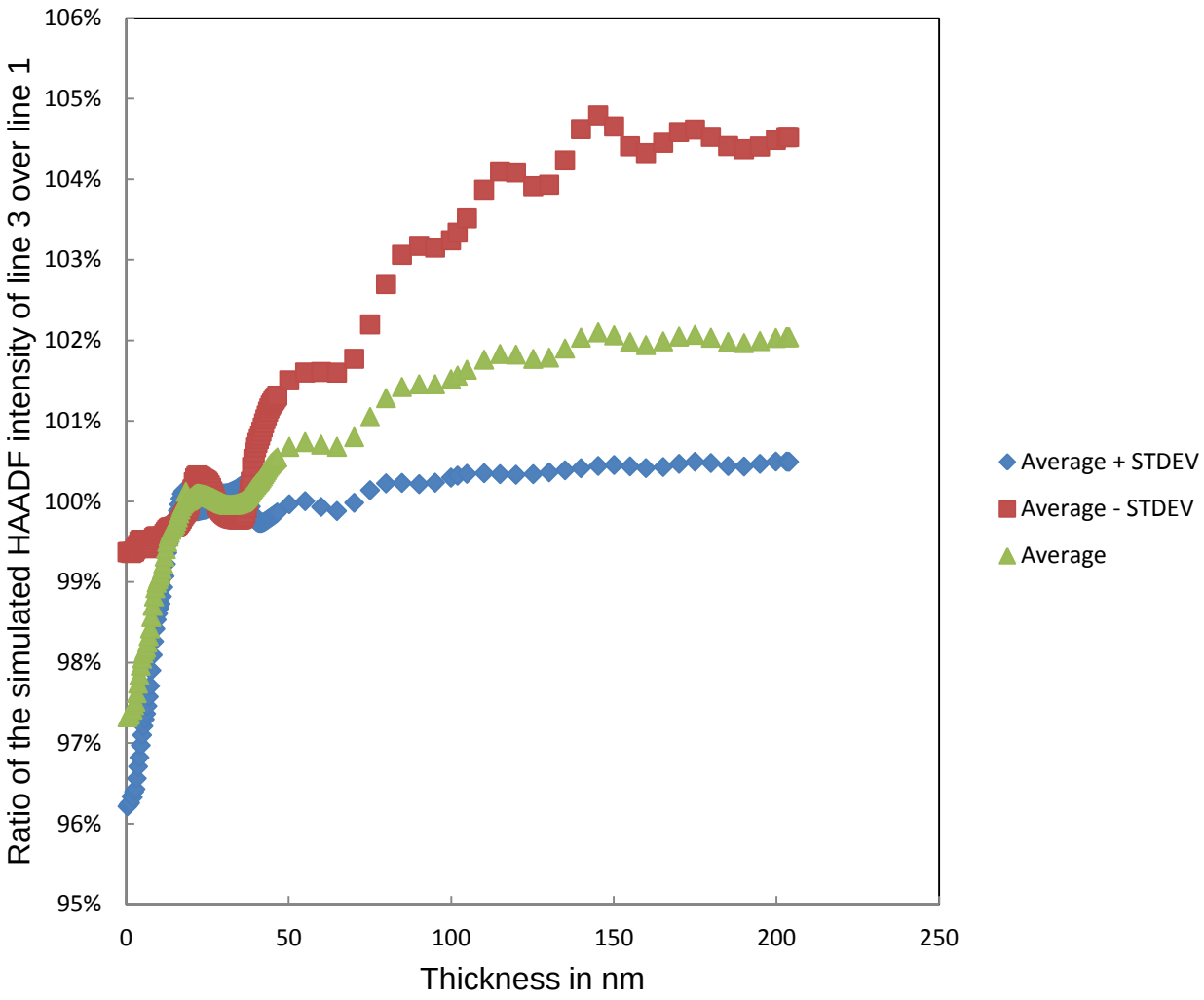

Figure 54: Intensity ratio of line 3 over line 1 for gold <100>.

From above figures, we see that the simulated HAADF intensity difference between different line scan is only a few + / - percentage. This error range is acceptable. I conclude that the simulated HAADF intensity statistics sampled on line scan is acceptable because the error is only a few +/- percentage between 1-D and 2-D data points.

3.3.3. Simulation of Orientation Dependence

The orientation dependence of HAADF intensity is studied. A single crystal of silicon <100> is used for comparative a CBED & HAADF study. The Figure 55 shows the position where both CBED & HAADF are evaluated.

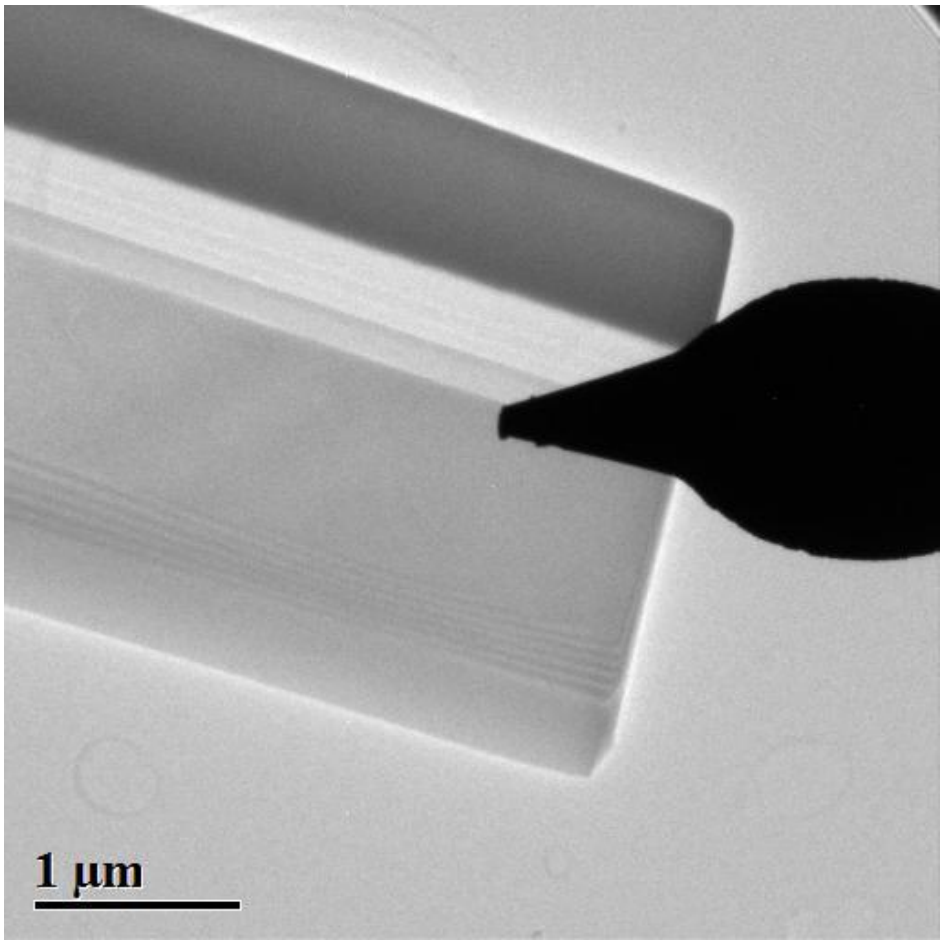

Figure 55: BF TEM micrograph of Si <100> showing the position where both CBED & HAADF were acquired. The corresponding HAADF image is shown in Figure 56.

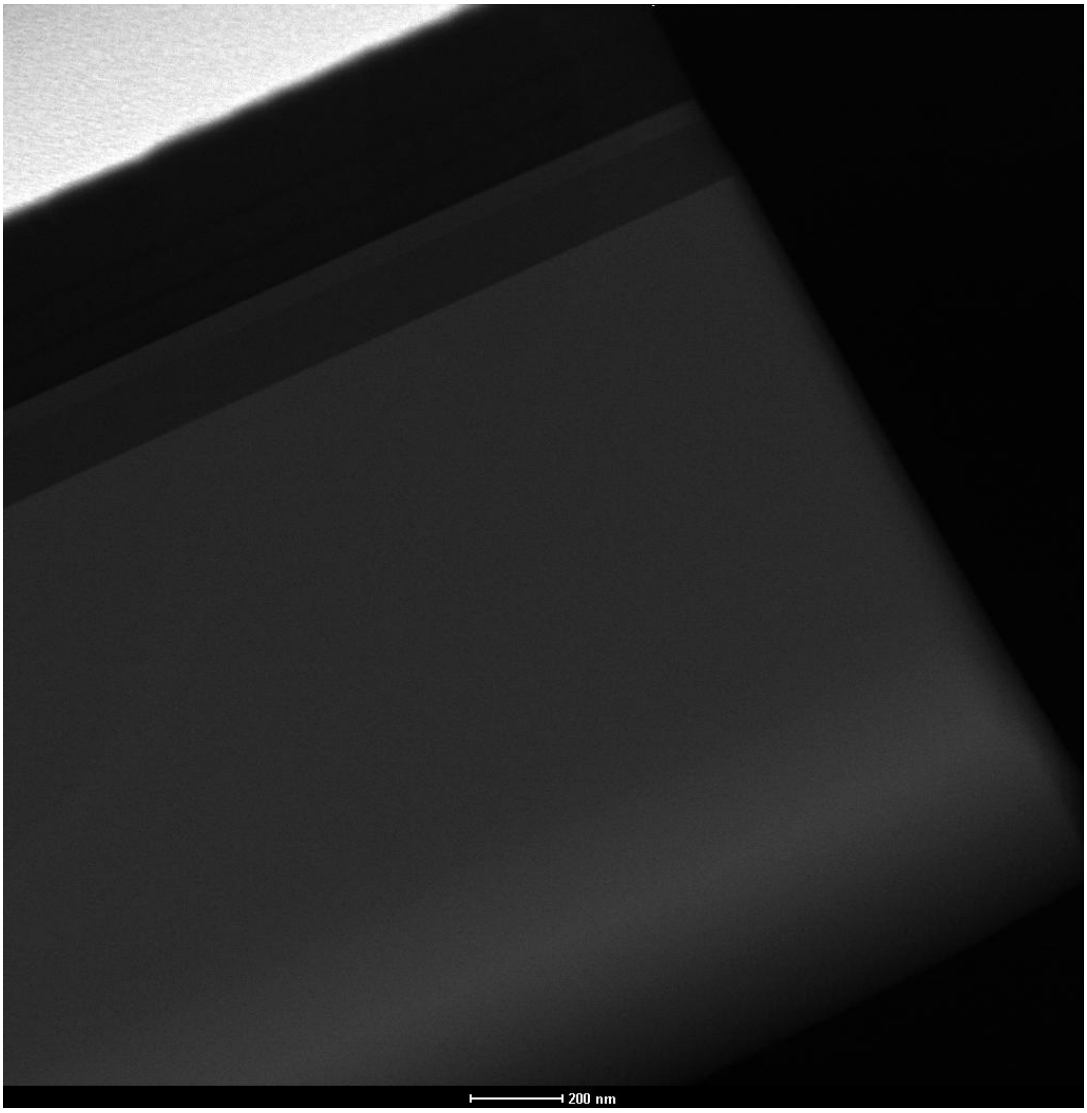

Figure 56: The corresponding HAADF image of the sample shown in Figure 55.

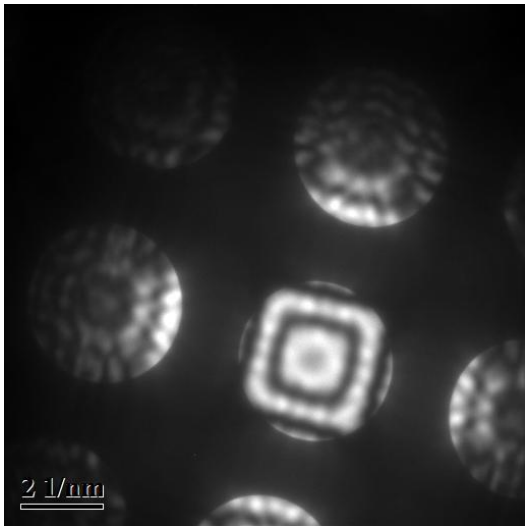

Figure 57: The corresponding experimental CBED of Si <100>.

Figure 58 is the CBED simulation using the UIUC's software [99] for a thickness of 245 nm.

Figure 58: Simulated CBED of Si <100>.

Previously, in Figure 10, <110> silicon was studied. A contrast of 0.023% / nm was used to determine the HAADF thickness. However, if 0.023% / nm is used in the <100> case, the thickness by determined from HAADF would be 146 nm which represents a huge deviation from the simulated CBED thickness of 245 nm. If the CBED match is reliable, the 0.023% / nm for <110> silicon has to be changed to 0.014% / nm for <100> silicon corresponding to a significant orientation dependence of the HAADF intensity. In the figures for high atomic number simulations an additional increase of intensity is found for larger thicknesses. This increase is not expected. Experimental data also do not support this effect seen in the simulations presented here, but when comparing the experimental data in Figure 13 with the results from this 100 oriented sample the match is much better than for the simulated data. Figure 13 is shown below again, but this time with the sample thickness in the x-axis and the fractions of electrons on the y-axis. The results for the intensity from figure 56 and the data on the thickness from figure 13 are included for comparison.

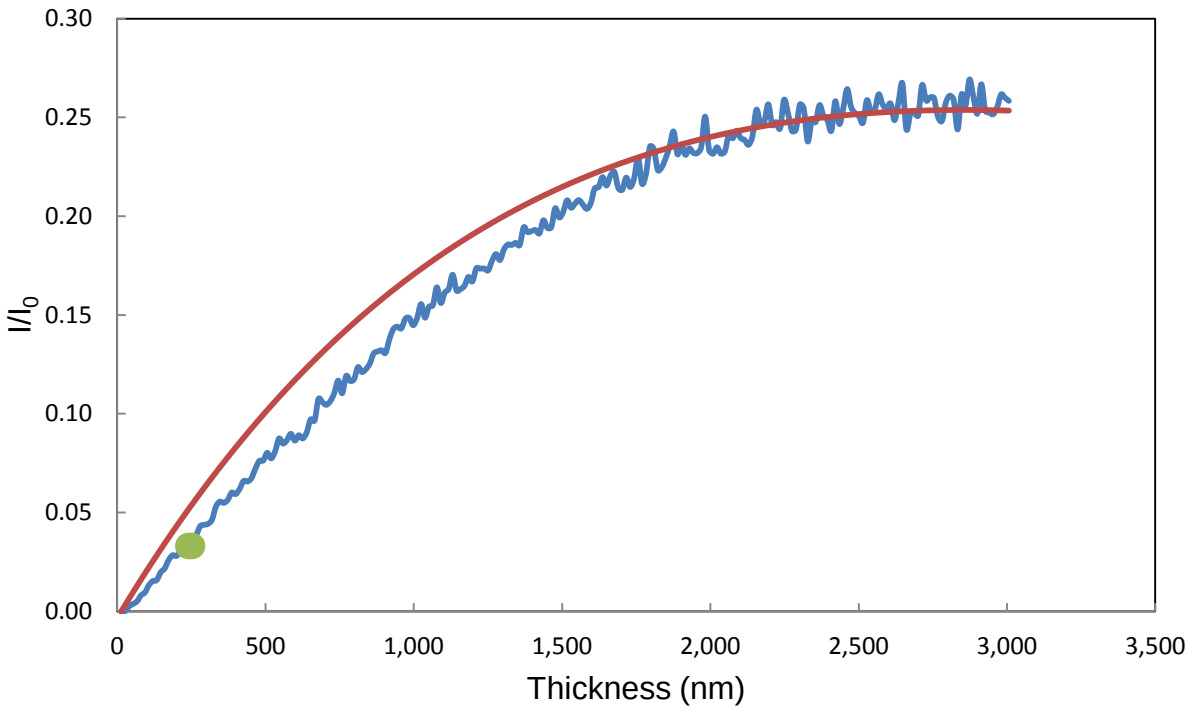

Figure 59: Intensity vs. thickness data from two different experiments and one model. The smooth curve represents equation 15 for Si, the green data point is from the CBED image of Figure 57, the corresponding HAADF micrograph of Figure 56. The rough curve is the result of the wedge-shaped Si sample shown in Figure 13.

The main reason for this artefact of a plateau in intensity and a later intensity incease in simulations is the sampling size used in the multislice simulation. The simulations were done for each beam position with a real-space area of 1.28 nm x 1.28 nm (256x256 pixels). This corresponds to a pixel size of 5 pm. The projected potential is first calculated with the same sampling size and the electron wave function as a function of position in the sampling area is subjected to a phase shift proportional to the projected potential. The resulting wave function is then Fourier transformed (yielding a diffraction pattern in reciprocal space). An additional phase shift (the propagator function) proportional to tan(2Θ) and proportional to the slice thickness is introduced for

this Fourier-transformed wave function. After this phase shift is introducted in Fourier space the electron wave function is back-Fourier transformed into real space and the next slice with its projected potential is used.

The pixel size in Fourier space is the inverse of the real-space dimension of the simulated area: 0.78 nm^{-1}. The Fourier pattern of 256x256 pixels is centered about 0 degree beam tilt, therefore the edge of the Fourier pattern starts at 128x0.78 nm^{-1} =100 nm^{-1}. With an electron wavelength of 2 pm the wave vector is 500 nm^{-1}, and the corresponding scattering angle 2Θ is 100 nm^{-1}/500 nm^{-1} = 200 mrad. Therefore, the maximum used range in the diffraction pattern is 282 mrad at the corners of the field. This range corresponds to the range for the outer radius of the electron diffraction pattern. Some part is not considered, another part is used, as shown in Figure 60.

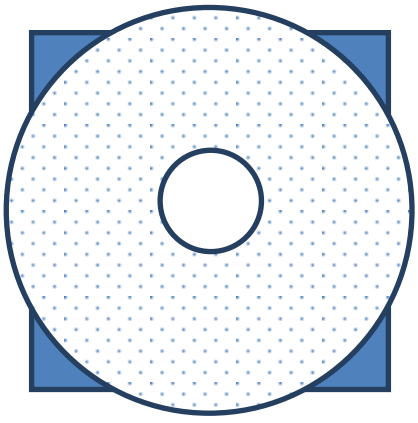

Figure 60: Schematic of detector range (dotted area) and the simulated area (solid background) in Fourier space.

This is not an ideal situation for simulating diffraction patterns and HAADF-STEM intensities. Choosing a smaller sampling size in real space would correspondingly increase the angular range for the Fourier space. This smaller real-space sampling size however would limit the beam diameter used in real space for the simulations. For large sample sizes over 100 nm the beam spread is about 0.45 nm ($\sqrt{thickness * wavelength}$) for the incident beam alone. Considering scattering anges of 200 mrad the spread is several 10 nm. Alternatively, a larger sampling area can be used with 512x512 or 1024x1024 pixels. This however would increase the time required for the simulations by a few orders of magnitude. The sampling size used here was chosen as a compromise between computational time needed for simulations and the size of the electron beam and the diffraction pattern.

As a consequence of this compromise HAADF-STEM intensities are not correctly predicted for large sample thicknesses and high atomic numbers. In these cases the periodic boundary conditions in the real-space and Fourier-space patterns introduce artefacts equivalent to mirroring at the edges of the simulated fields. This is obviously less relevant for thin samples and low atomic numbers where only a tiny fraction of the electron wavefunction reaches an edge of the simulated field in real- or Fourier-space. This corresponds to weak scattering to high angles in a thin sample. However, if the sample is thick a high percentage of electrons get scattered beyond 200 mrad. This is no problem in an experiment, but it poses problems for a simulation relying on Fourier theorems which require periodic boundary conditions.

Another issue with the simulations is the use of non-relevant absorption parameters. Absorption is in classical terms defined as a reduction of Bragg intensities by inelastic scattering events: thermal diffuse scattering for reduced scattering into Bragg reflections, and plasmon excitations for forward scattering and reduction of the undiffracted and diffracted intensities. While absorptive parameters have been calculated [102], our experimental data for absorptive parameters do not match calculated ones. Experimental absorption data are significantly lower, especially for high atomic numbers, than absorption data derived from literature [102]. The relevant data from Peng et al. for the absorption are obtained for forward inelastic scattering by excitation of plasmons (in their notation used in [102], this is a1+a2+a3+a4+a5), while the high angle parameters given in [102] only represent the redistribution of Bragg intensities into locations between Bragg reflections.

4. CONCLUSIONS

Based on the work done so far, the following conclusions can be reached. For thin samples the HAADF-STEM contrast should follow a simple approach described by Heidenreich [113] with $I \propto t\rho Z^{\alpha}$, where *t* is the sample thickness, *ρ* is the atomic density, *Z* is the atomic number, and *α* is a parameter between 1 and 2. However, with incorporation of the atomic densities the data from Figure 11 reveal that this simple approach cannot be used for all elements. There is no simple relationship between atomic number and HAADF-STEM contrast which can be described by only one parameter α. This work shows that the situation is much better when we consider the interaction cross section instead of the intensity as a function of thickness. One issue for the intensity as a function of thickness is the difference in atoms per volume for different materials. The effect of differing atomic densities can be avoided if one considers the interaction cross section σ. This work also shows that there are significant differences in the interaction cross sections between those obtained from experiments done here and those from potentials found in the literature [100]. Especially for high atomic number materials, experimental data for σ are smaller than calculated values from models [100]. This can be in part explained by inelastic scattering contributions that are not adequately described in the models used to determine σ.

Another important conclusion of this work is that CBED patterns of FIB-processed samples cannot be used to determine sample thicknesses. Gallium ion

implantation at the sample surfaces and the formation of amorphous layers on the sample surfaces due to breaking of bonds in the ion beam are leading to an underestimation of the sample thickness. These amorphous layers do not influence the part of the CBED pattern that is relevant to the thickness determination. CBED methods however are still well suited for the calibration of the HAADF-STEM contrast if amorphization is minimized, for example with Ar-ion milling or electro polishing. A better method to determine the HAADF-STEM contrast is the preparation of wedge-shaped samples. These samples provide a slope of the detector intensity versus sample thickness, and the amorphous layers can simply be accounted for by an offset in the signal.

Thus, quantitative HAADF-STEM calculations of thicknesses or compositions require intensity calibration for each element and each compound separately. The results of contrast simulation yield scattering intensities that are consistent with the experimental results. The HAADF STEM signal shows only limited dynamic scattering effects and orientation effects and is mainly determined by incoherent scattering. The volumes of nanoparticles were determined for samples with known composition from a single HAADF-STEM micrograph without tilting of the sample. This method is especially useful for the measurement of volumes of nanoparticles with non-spherical shape. For binary alloys with known TEM sample thickness, the composition can be determined from a single HAADF-STEM micrograph.

A new method for the quantification of the HAADF-STEM signal is employed. The HAADF signal is calibrated with regard to the signal acquired for the electron beam impinging on the CCD camera. The HAADF detector shows a nearly linear response to the electron intensity. Volumes of nanoparticles are determined instead of diameters as this yields much more reliable data for the number of atoms in a nanoparticle and for the surface area. The method presented here is an efficient way to determine nanoparticle sizes. The limitations are that the nanoparticle composition has to be known. Otherwise the binary compositions can be determined given a known thickness. There is some orientation dependence of the HAADF-STEM signal observed, this dependence can be determined for each material. This orientation dependence is more significant for beam directions near a highly symmetrical crystallographic direction especially for materials with higher atomic number. No real 3-D information can be obtained without tilt series. However, this method allows people to determine the volume and the thickness of nanoparticles from a single micrograph. The HAADF-STEM technique is furthermore limited by the lateral resolution of the microscope. The method presented here can be used for microscopes with limited resolution (no atomic resolution) yielding data on the volume without imaging of atomic columns. Even if the resolution is limited to several angstroms, this method can give reliable particle sizes for nanoparticles of less than 2 nm, as the signal solely relies on the integrated intensity over each nanoparticle. Combined with EDS, STEM, and EELS, HAADF-STEM is a powerful tool to directly measure thicknesses, volumes, porosities, or compositions of nanomaterials quantitatively.

For thin samples electron channeling reduces the HAADF-signal in the case of perfect zone-axis orientations. This effect differs from zone axis to zone axis, but as shown here it can introduce an error of up to 40%. Therefore, zone axis orientations should be avoided in the thickness analysis with HAADF-STEM. For thicker samples however, this zone axis effect of electron channeling should disappear again as the scattered electrons are highly tilted with respect to the zone axis (several 10 to 100 mrad).

If samples are not oriented with the electron beam parallel to a low-indexed zone axis quantitative thickness measurements are possible with HAADF-STEM if a calibration standard is available. This calibration standard can be used once. As long as the detector settings (or the detector) are not changed, the calibration values can be used repeatedly to obtain thickness information. The simple approach by Heidenreich [113] where the intensity increases linearly with sample thickness is useful if the total scattered intensity is only a few % of the incident electron intensity. However, for larger sample thicknesses we have to take into account that the scattered intensity is limited to the intensity available through the incident electron beam, and we have to consider absorption as outlined in equation 15.

Simulations show that coherent multiple scattering effects are present, but they only influence the measured value of the thickness by a few percent. The overall accuracy of this method for thickness determination is about 10% if off-zone axis conditions are used. It should be noted here that the conditions for reducing coherent

multiple scattering effects require a small camera length setting and a well-centered HAADF detector. The electron beam can be shifted with the help of deflectors with respect to the center of the HAADF detector. We used the smallest available camera length (80 mm) at the Tecnai F30 transmission electron microscope to minimize coherent multiple scattering effects. The consequence of small camera length is however a very weak signal especially for small nanoparticles.

One important aspect of this work is the study of the HAADF-STEM signal for thick samples, i.e., samples that are far too thick for high-resolution (atomic resolution) imaging. Many samples prepared by FIB are too thick for high-resolution TEM, especially if heavy elements are present in high concentrations. I studied several samples in this work that were several microns thick. Those samples are usually considered useless for TEM. However, here I intentionally looked at samples this thick to identify relevant scattering parameters. With wedge-shaped multilayer systems I was able to reliably determine the contrast as a function of sample thickness. With increasing thickness the detector receives an increasing electron flux, which reaches a maximum and decreases with further increase in thickness. This signal behavior as a function of sample thickness can be fitted in all cases studied here with a three-parameter equation, which accounts for the elastic scattering cross section of each element, the absorption of electrons in the sample (multiple inelastic scattering events), and for the limited size of the HAADF detector in the diffraction plane.

This study shows an interesting aspect of the HAADF-STEM contrast at interfaces of materials with different density. When the electron beam is placed at the interface of a high density material to a low-density material in a thick sample, an increase of HAADF-STEM signal is observed. This increase can be explained by initial scattering events in the high density material (mostly elastic scattering), which changes the trajectory of electrons as they get scattered to high angles. Near the interface to a low-density material some electrons that are scattered to high angles, will cross over to the low-density material. There, these electrons will experience less additional scattering and less absorption than in the high-density material. Therefore, more electrons will reach the HAADF-STEM detector than in the center of the high-density material. This effect occurs for sample thicknesses that are greater than the sample thickness where the maximum of HAADF detector intensity occurs. A schematic of this effect is shown in Figure 61. For the beam position just inside the high-density material as shown in Figure 61 more electrons reach the detector than for a beam position well inside the highly absorbing high-density material.

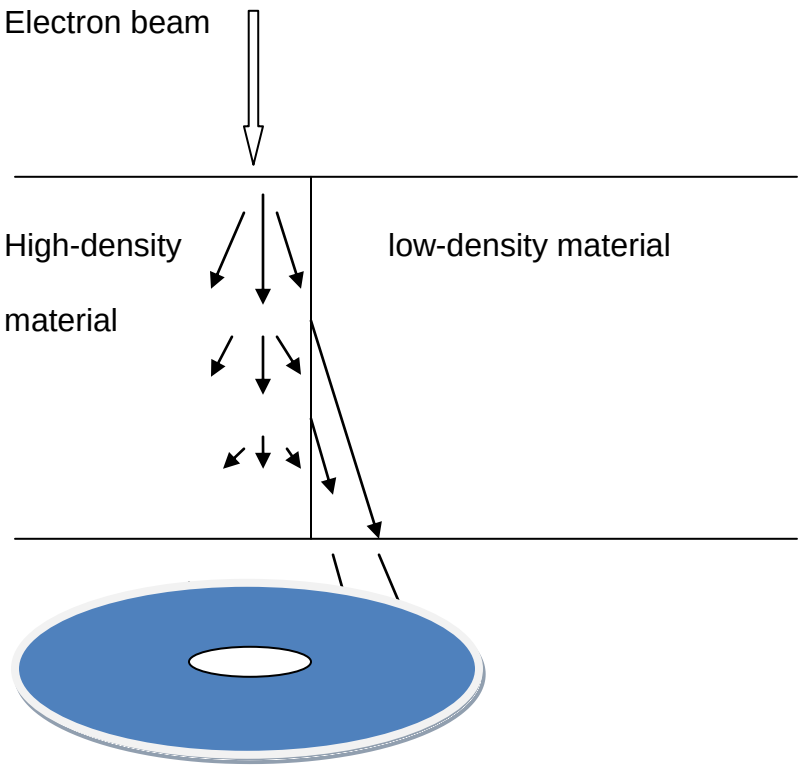

Figure 61: Schematic view of HAADF for a thick sample at the interface between a high- and low-density material.

Typical particle size distributions show the fractions of nanoparticles in certain diameter intervals. The measurement of volumes provides the fractions in certain volume intervals. If a volume measurement is done for a nanoparticle with the method

presented here a typical error of 15% has to be considered. This relative error $\Delta V/V$ translates into a relative error in diameter D of $\Delta D/D = \Delta V/3V$ (from $6\pi V=D^3$). When spherical particles are studied the relative error for individual particle diameter measurements is only about 5% when volume data from HAADF-STEM are transformed into diameter data.

In the approach described in this work a contrast and brightness setting was used which requires a non-saturated HAADF-STEM detector when the electron beam is scanned across the detector in imaging mode for absolute intensity calibration. Considering the experiments and calibrations done in this project, an alternative can be proposed here, which disregards that the detector is saturated when the beam is scanned across it. Intensities are calibrated using directly the CCD camera to determine the absolute intensity of the incident electron probe. For calibration of the detector the incident electron beam is significantly reduced (by reducing the extraction voltage of the field-emission electron source and by purposely misaligning gun tilt and gun shift) and scanned across the HAADF-detector in imaging mode and acquiring a CCD micrograph of the central diffraction disk (the sample if retracted) to measure the absolute electron beam intensity.

A more sensitive setting for contrast and brightness allows for a better signal to noise ratio, and it makes imaging of small nanoparticles much easier compared to the case of the contrast 12.5% setting used as described above. The contrast brightness setting used here was a compromise to obtain an almost linear response of the detector

up to the case when the whole incident beam hits the detector. The limited dynamic range of the detector therefore required a relatively low contrast (low sensitivity). With a higher contrast setting of the detector small nanoparticles with low signal could be analyzed more accurately. This could be accomplished by using low-intensity calibrations of the HAADF detector with the CCD camera, and measuring the incident beam only with the CCD camera.

REFERENCES

[1] G. Kostorz, R. Erni and H. Heinrich, “Experimental investigations of microstructures”, in: “Thermodynamics, Microstructures and Plasticity”, Edrs.: A. Finel, D. Mazière, M. Veron, Nato Science Series II, Kluwer Academic Publ., Dordrecht, Netherlands, (2003) 439-464.

[2] Y. Wang, C. Ma, X. Sun and H. Li, “Preparation of nanocrystalline metal oxide powers with the surfactant-mediated method”, Inorg. Chem. Commu., 5 (2002) 751-755.

[3] M. Niederberger and G. Garnweitner, “Organic reaction pathways in the nonaqueous synthesis of metal oxides nanoparticles”, Chem. Eur. J., 12 (2006) 7282-7302.

[4] M. Rajamathi and R. Seshadri, “Oxide and chalcogenide nanoparticles from hydrothermal reaction”, Current Opinion in Solid State and Material Science, 6 (2002) 337-345.

[5] B. Yuan, Q. Chen and M. Wang, “Crystallization and properties of Li-AI-B-Ti-Zn-silicate system glass-ceramic Fibres”, J. Materials Sci., 24 (1989) 4488-4494.

[6] Z. Wang, L. Zhu, H. Zhan, J. Xu, H. Fang, B. Yuan and Q. Chen, “Study of far-IR transmitting Te-Se-X system glasses: Some fundamental problems about application”, J. Chin. Ceram. Soc., 22 [3] (1994) 211-218.

[7] G. Möbus and S. Nufer, “Nanobeam propagation and imaging in a FEGTEM/STEM”, Ultramicroscopy, 96 (2003) 285–298.

[8] P. Mohan, B. Yuan, T. Patterson, V. Desai and Y. Sohn, “Degradation of yttria-stabilized zirconia thermal barrier coatings by vanadium pentoxide, phosphorous pentoxide, and sodium sulfate”, J. Am. Ceram. Soc., 90 [11] (2007) 3601–3607.

[9] E. Perez, A. Ewh, J. Liu, B. Yuan, D. Keiser Jr. and Y. Sohn, “Phase constituents of Al-rich U–Mo–Al alloys examined by transmission electron microscopy”, J. Nuclear Materials, 394 (2009) 160–165.

[10] P. Mohan, B. Yuan, T. Patterson, V. Desai and Y. Sohn, “Degradation of yttria stabilized zirconia thermal barrier coatings by molten CMAS (CaO-MgO-Al_2O_3-SiO_2) deposits”, Materials Science Forum, 595-598 (2008) 207-212.

[11] Y. Fan, Y. Wang, J. Lou, S. Xu, L. Zhang, L. An and H. Heinrich, “Formation of silicon-doped boron nitride bamboo structures via pyrolysis of a polymeric precursor”, J. Am. Ceram. Soc., 89 (2006) 740-742.

[12] S. Bandyopadhyay, S. K. Samadrala, A. Bhowmick and S. Gupta, chapter “Applications of Atomic force Microscope (AFM) in the Field of Nanomaterials and Nanocomposites”, Edited by S. Seal, in series “Nanostructure Science and Technology”, series editor: D. Lockwood, for a book entitled “Functional Nanostructures” (Editor: S. Seal) Springer Science and Business Media, LLC, New York (2007) 504-568.

[13] S. Van Aert, K. Batenburg, M. Rossell, R. Erni and G. Van Tendeloo, “Three-dimensional atomic imaging of crystalline nanoparticles”, Nature, 470 [7334] (2011) 374-377.

[14] S. Van Aert, J. Verbeeck, R. Erni, S. Bals, M. Luysberg, D. Van Dyck and G. Van

Tendeloo, “Quantitative atomic resolution mapping using high-angle annular dark field scanning transmission electron microscopy”, Ultramicroscopy, 109 (2009) 1236-1244.

[15] R. Ristau, F. Hofer, K. Barmak, K. Coffey and J. Howard, “An EFTEM and conical dark field investigation of co-sputtered CoPt+yttria stabilized zirconia thin films”, Micron, 29 [1] (1998) 33-41.

[16] L. Coast-Smith, R. Brydson, P. Tsakiropoulos, F. Hofer, W. Grogger, D. Dunford and C. Ward-Close, “Characterization of thick film Ti/Al nanolaminates”, Micron, 29 [1] (1998) 17-31.

[17] M. Terheggen, H. Heinrich, G. Kostorz, A. Romeo, D. Baetzner, A. Tiwari, A. Bosio and N. Romeo, “Structural and chemical interface characterization of CdTe solar cells by transmission electron microscopy”, Thin Solid Films, 431-432 (2003) 262-266.

[18] D. Williams and C. Carter, “Transmission Electron Microscopy”, ISBN: 0-306-45324-X, 1996. Publisher Springer.

[19] P. Wang, A. Blelch, U. Falke and P. Goodhew, “Geometric aspects of lattice contrast visibility in nanocrystalline materials using HAADF STEM” Ultramicroscopy, 106 (2006) 277–283.

[20] K. Ishizuka, “A practical approach for STEM image simulation based on the FFT multislice method”, Ultramicroscopy, 90 (2002) 71–83.

[21] T. Morimura and M. Hasaka, “Bloch-wave-based STEM image simulation with layer-by-layer representation”, Ultramicroscopy, 109 (2009) 1203–1209.

[22] T. Yamazaki, M. Kawasaki, K. Watanabe, I. Hashimoto and M. Shiojiri, “Effect of small crystal tilt on atomic-resolution high-angle annular dark field STEM imaging”, Ultramicroscopy, 92 (2002) 181–189.

[23] T. Yamazaki,*, K. Watanabe, N. Nakanishi and I. Hashimoto, “Role of surface amorphous film in high-resolution high-angle annular dark field STEM imaging”, Ultramicroscopy, 99 (2004) 125–135.

[24] K. Watanabe, E. Asano, T. Yamazaki, Y. Kikuchi and I. Hashimoto,” Symmetries in BF and HAADF STEM image calculations”, Ultramicroscopy, 102 (2004) 13–21.

[25] S. Bals, B. Kabius, M. Haider, V. Radmilovic and C. Kisielowski, “Annular dark field imaging in a TEM”, Solid State Communications, 130 (2004) 675–680.

[26] J. Cowley, V. Merkulov and J. Lannin, “Imaging of light-atom nanocrystals with a thin annular detector in STEM”, Ultramicroscopy, 65 (1996) 61-70.

[27] H. Xu, R. Twesten, L. Menard, A. Frenkel, R. Nuzzo, D. Johnson and J. Yang, “Outlook of application of aberration corrected-electron microscopy in the ligand-protected metal clusters”, Microsc. Microanal., 10 [Suppl 3] (2004) 62-63.

[28] S. Bals, R. Kilaas and C. Kisielowski, “Nonlinear imaging using annular dark field TEM”, Ultramicroscopy, 104 (2005) 281–289.

[29] A. Howie, “Image contrast and localized signal selection techniques“, J. Microscopy, 117 (1979) 11-23.

[30] K. Kimura, S. Hata, S. Matsumura and T. Horiuchi, “Tomographic dark-field TEM observation of ordered precipitates in a Ni-Mo alloy”, Advanced Materials & Processes, February (2006) 46-47.

[31] K. Kimura, S. Hata, S. Matsumura and T. Horiuchi, “Dark-field transmission electron microscopy for a tilt series of ordering alloys: toward electron tomography”, J. Electron Microscopy, 54 (2005) 373-377.

[32] M. Weyland and P. Midgley, “Electron tomograph”, Materials today, December (2004) 32-40.

[33] J. Frank, ”Electron Tomography”, Plenum Press, New York, 1992.

[34] P. Penczek and J. Frank, “Resolution in electron tomography”, in: “Electron Tomography”, edited by J. Frank, Springer, New York (2006) 307-330.

[35] P. Buseck, R. Dunin-Borkowski, B. Devouard, R. Frankel, M. McCartney, P. Midgley, M. Pósfai and M. Weyland, “Magnetite morphology and life on Mars”, Proc. National Acad. Sciences, 98 (2001) 13490-13495.

[36] A. Koster, R. Grimm, D. Typke, R. Hegerl, A. Stoschek, J. Walz and W. Baumeister, “Perspectives of molecular and cellular electron tomography“, J. Struct. Biol., 120 (1997) 276-308.

[37] M. Barth, R. Bryan, R. Hegerl and W. Baumeister, “Estimation of missing cone data in three-dimensional electron microscopy”, Scanning Microscopy, Suppl., no. 2 (1988) 277-84.

[38] G. Veith, A. Lupini, S. Pennycook, G. Ownby and N. Dudney, “Nanoparticles of gold on γ-Al_2O_3 produced by dc magnetron sputtering”, J. Catalysis 231 (2005) 151–158.

[39] B. Yuan, Q. Chen and M. Wang, “Micro-crystallization and properties of glass fibers”, J. Chin. Ceram. Soc., 16 [5] (1988) 408-415.

[40] Q. Chen, L. Zhu, Z. Wang and B. Yuan, “Stability and crystallization of Te-Se-X system I.R. transmission glasses”, Proc. of the 1991 Dalian International conference on Glass, China Science and Technology Press, (1991) 174-179.

[41] H. Jiang, H. Sun, F. Gan and B. Yuan, “Properties and structure of the IR transmitting glasses in the $CdCI_2$ based systems”, J. Materials Sci. Lett., 9 (1990) 1195-1196.

[42] H. Jiang, B. Yuan, H. Sun and F. Gan, “A study on the structures of glasses based on $CdCI_2$ and $PbCI_2$”, J. Materials Sci. Lett., 10 (1991) 1326-1328.

[43] Y. Yang and R. Egerton, “Test of two alternative methods for measuring specimen thickness in a transmission microscope”, Micron, 26 (1995) 1-5.

[44] S. Hillyard and J. Silcox, “Thickness effects in ADF STEM zone axis images”, Ultramicroscopy, 52 (1993) 325-334.

[45] D. Brandon and W. Kaplan, “Microstructural Characterization of Materials”, June (2008) ISBN: 0470027851.

[46] B. Fultz and J. Howe, “Transmission Electron Microscopy and Diffractometry of Materials”, Berlin; New York: Springer. (2008) ISBN: 978-3-540-73885-5, (also see 2001 ed.)

[47] C. Rossouw and M. Whelan, “The orientation dependence of measured inelastic scattering probabilities for fast electrons in single crystals”, J. Phys. D: Appl. Phys. 12 (1979) 1521-33.

[48] M. Vulovic, B. Rieger, L. van Vliet, A. Koster and R. Ravelli, “A toolkit for the characterization of CCD cameras for transmission electron microscopy”, Acta Crystallographica, D 66 (2010) 97-109.

[49] S. Senapati, “Evolution of lamellar structures in Al-Ag alloys”, MS thesis, University of Central Florida, (2005).

[50] M. Otten, “High-Angle Annular Dark-Field Imaging on a TEM/STEM System”, J. of Electron Microscopy Technique 17 (1991) 221-230.

[51] J. Liu and J. Cowley, “Imaging with High-Angle Scattered Electrons and Secondary Electrons in the STEM”, Ultramicroscopy 37 (1991) 50-71.

[52] R. Petrova, “Quantitative high-angle annular dark field scanning Transmission Electron Microscopy for Materials science”, PhD dissertation, University of Central Florida, (2006).

[53] E. Kirkland, “Advanced Computing in Electron Microscopy”, (1998) ISBN: 0-306-45936-1.

[54] E. Kirkland, R. Loane and J. Silcox, “Simulation of annular dark field STEM images using a modified multislice method”, Ultramicroscopy, 23 (1987) 77-96.

[55] S. Findlay, D. Klenov, S. Stemmer and L. Allen, “Atomic number contrast in high angle annular dark field imaging of crystals”, Materials Science and Technology, 24 [6] (2008) 660-666.

[56] H. Nukala, “Quantitative thickness mapping in high-angle annular dark-field (HAADF) scanning transmission electron microscopy (STEM)”, MS thesis, University of Central Florida, (2008).

[57] V. Jantou-Morris, M. Horton and D. McComba, “The nano-morphological relationships between apatite crystals and collagen fibrils in ivory dentine”, Biomaterials, 31 (2010) 5275-5286.

[58] D. Araújo, P. Achatz, R. El Bouayadi, A. García, M. Alegre, M. Villar, F. Jomard and E. Bustarret, “Local boron doping quantification in homoepitaxial diamond structures”, Diamond & Related Materials, 19 (2010) 972–975.

[59] R. Erni, H. Heinrich and G. Kostorz, “Quantitative characterisation of chemical inhomogeneities in Al-Ag using high-resolution Z-contrast STEM”, Ultramicroscopy, 94 (2003) 125-133.

[60] Rolf Erni, “Atomic-scale analysis of precipitates in Al-3at.%Ag: transmission electron microscopy”, Dissertation of doctor of natural sciences, ETH Zürich, (2003), Diss. ETH No. 1498.

[61] Y. Kotaka, “Essential experimental parameters for quantitative structure analysis using spherical aberration-corrected HAADF-STEM”, Ultramicroscopy, 110 (2010) 555–562.

[62] Y. Kotaka, K. Honda, T. Yamazaki, K. Watanabe, H. Fujisawa and M. Shimizu, “Quantitative analysis of atomic resolution HAADF-STEM (Z-contrast) imaging for $PbTiO_3$ / $SrTiO_3$ substrate dielectric thin films“, Microsc. Microanal., 12 (2006) 1352-1353.

[63] K. Kuramochi, T. Yamazaki, Y. Kotaka, M. Ohtsuka, I. Hashimoto and K. Watanabe, “Effect of chromatic aberration on atomic-resolved spherical aberration corrected STEM images”, Ultramicroscopy, 110 (2009) 36–42.

[64] D. Araújo, R. El Bouayadi, M. Gutiérrez, C. Pastore and M. Hopkinson, “InAs/GaAs quantum dots morphology: Nanometric scale HAADF simulations”, Materials Science and Engineering, B 165 (2009) 88–93.

[65] P. Voyles, P. Muller, J. Grazul, P. Citrin and H. Gossmann, “Atomic-scale imaging of individual dopant atoms and clusters in highly n-type bulk Si”, Nature, 416 (2002) 826-829.

[66] M. Haruta, H. Kurata, H. Komatsu, Y. Shimakawa and S. Isoda, “Effects of electron channeling in HAADF-STEM intensity in La_2CuSnO_6”, Ultramicroscopy, 109 (2009) 361–367.

[67] Z. Yu, D. Muller and J. Silcox, “Effects of specimen tilt in ADF-STEM imaging of a-Si/c-Si interfaces”, Ultramicroscopy, 108 (2008) 494-501.

[68] D. Klenov and S. Stemmer, “Contributions to the contrast in experimental high-angle annular dark-field images”, Ultramicroscopy, 106 (2006) 889–901.

[69] L. Menard, S. Gao, H. Xu, R. Twesten, A. Harper, Y. Song, G. Wang, A. Douglas, J. Yang, A. Frenkel, R. Nuzzo and R. Murray, “Sub-aanometer Au monolayer-

protected clusters exhibiting molecule-like electronic behavior: Quantitative high-angle annular dark-field scanning transmission electron microscopy and electrochemical characterization of clusters with precise atomic stoichiometry“, J. Phys. Chem., B 110 (2006) 12874-12883.

[70] L. Menard, H. Xu, S. Gao, R. Twesten, A. Harper, Y. Song, G. Wang, A. Douglas, J. Yang, A. Frenkel, R. Murray and R. Nuzzo, “Metal core bonding motifs of monodisperse icosahedral Au13 and larger Au monolayer-protected clusters as revealed by X-ray absorption spectroscopy and transmission electron microscopy“, J. Phys. Chem., B 110 (2006) 14564-14573.

[71] L. Menard, F. Xu, R. Nuzzo and J. Yang, “Preparation of TiO_2-supported Au nanoparticle catalysts from a Au13 cluster precursor: Ligand removal using ozone exposure versus a rapid thermal treatment“, J. Catalysis, 243 (2006) 64–73.

[72] K. Jarausc and D. Leonard, “Three-dimensional electron microscopy of individual nanoparticles”, J. Electron Microscopy, 58 [3] (2009) 175–183.

[73] Z. Li, N. Young, M. Di Vece, S. Palomba, R. Palmer, A. Bleloch, B. Curley, R. Johnston, J. Jiang and J. Yuan, “Three-dimensional atomic-scale structure of size-selected gold nanoclusters”, Nature, 451 (2008) 46-49.

[74] Z. Li, J. Yuan, Y. Chen, R. Palmer and J. Wilcoxon, “Local three-dimensional visualization of nanoparticle assemblies”, Adv. Mater., 17 (2005) 2885–2888.

[75] Z. Li, J. Yuan, Y. Chen, R. Palmer and J. Wilcoxon, “Direct imaging of core-shell structure in silver-gold bimetallic nanoparticles”, Appl. Phys. Lett., 87 (2005)

243103.

[76] J. LeBeau, S. Findlay, L. Allen and S. Stemmer, “Standardless atom counting in scanning transmission electron microscopy”, Nano Lett., 10 (2010) 4405-4408.

[77] J. LeBeau, S. Findlay, X. Wang, A. Jacobson, L. Allen and S. Stemmer, “High-angle scattering of fast electrons from crystals containing heavy elements: Simulation and experiment”, Phys. Rev., B 79 (2009) 214110.

[78] J. LeBeau, S. Findlay, L. Allen and S. Stemmer, “Quantitative atomic resolution scanning transmission electron microscopy”, Phys. Review Lett., 100 (2008) 206101.

[79] J. LeBeau and S. Stemmer, “Experimental quantification of annular dark-field images in scanning transmission electron microscopy”, Ultramicroscopy, 108 (2008) 1653-1658.

[80] J. LeBeau, A. Alfonso, S. Findlay, S. Stemmer and L. Allen, “Quantitative comparisons of contrast in experimental and simulated bright-field scanning transmission electron microscopy images”, Phys. Rev., B 80 (2009) 174106.

[81] J. LeBeau, S. Findlay, L. Allen and S. Stemmer, “Quantitative HAADF-STEM and EELS”, Microsc. Microanal., 14 [Suppl 2] (2008) 1352-1353.

[82] N. Young, Z. Li, Y. Chen, S. Palomba, M. Di Vece and R. Palmer, “Weighing supported nanoparticles: Size-selected clusters as mass standards in nanometrology”, Phys. Rev. Lett., 101 (2008) 246103.

[83] E. Carlino and V. Grillo, “Atomic-resolution quantitative composition analysis using scanning transmission electron microscopy Z-contrast experiments”, Phys. Rev.,

B 71 (2005) 235303.

[84] V. Grillo, E. Carlino and F. Glas, “Influence of the static atomic displacement on atomic resolution Z-contrast imaging”, Phys. Rev., B 77 (2008) 054103.

[85] T. Konno, E. Okunishi, T. Ohsuna and K. Hiraga, "HAADF-STEM study on the early stage of precipitation in aged Al-Ag alloys", J. Electron Microscopy, 53 (2004) 611-616.

[86] S. Pennycook, D. Jesson, M. Chisholm, N. Browning, A. McGibbon and M. McGibbon, “Z-contrast imaging in the scanning transmission electron microscope“, J. Micros. Soc. Amer., 1 (1995) 231-251.

[87] J. McBride, T. Kippeny, S. Pennycook and S. Rosenthal, “Aberration-corrected Z-contrast scanning transmission electron microscopy of CdSe nanocrystals”, Nano lett., 7 (2004) 1279-1283.

[88] S. Pennycook and D. Jesson, “High-resolution incoherent imaging of crystals“, Phys. Rev. Lett., 64 (1990) 938-941.

[89] T. Akita, K. Tanaka, K. Okuma, T. Koyanagi and M. Haruta, “TEM and HAADF-STEM study of a Au catalyst supported on a TiO_2 nano-rod”, J. Electron Microscopy, 50 (2001) 473-477.

[90] T. Yamazaki, N. Nakanishi, A. Reznik, M. Kawasaki, K. Watanabe, M. Ceh and M. Shiojiri, “Quantitative high-resolution HAADF-STEM analysis of inversion boundaries in Sb_2O_3-doped zinc oxide“, Ultramicroscopy, 98 (2004) 305-316.

[91] J. Pizarro, P. Galindo, E. Guerrero, A. Yáñez, M. Guerrero, A. Rosenauer, D. Sales and S. Molina, “Simulation of high angle annular dark field scanning

transmission electron microscopy images of large nanostructures", Appl. Phys. Lett., 93 (2008) 153107.

[92] Y. Peng, P. Nellist and S. Pennycook, "HAADF-STEM imaging with sub-angstrom probes: a full Bloch wave analysis", J. Electron Microscopy, 53 (2004) 257-266.

[93] C. Rossouw, L. Allen, S. Findlay and M. Oxley, "Channeling effects in atomic resolution STEM", Ultramicroscopy, 96 (2003) 299-312.

[94] O. Krivanek, N. Delby and A. Lupini, "Towards sub-angstrom electron beams", Ultramicroscopy, 78 (1999) 1–11.

[95] N. Browning, I. Arslan, P. Moeck and T. Topuria, "Atomic resolution scanning transmission electron microscopy", Phys. Stat. Sol., B 227 (2001) 229-245.

[96] H. Heinrich, B. Yuan, H. Nukala and B. Yao, "Quantitative scanning transmission electron microscopy for the measurement of thicknesses and volumes of individual nanoparticles", Mater. Res. Soc. Symp. Proc., 1184 (2009) 119-124.

[97] B. Yao, PhD dissertation, University of Central Florida, (2008).

[98] B. Yao, R. Petrova, R. Vanfleet, V. Lam and K. Coffey, "Compositional stability of FePt nanoparticles on SiO_2/Si during annealing", J. of Appl. Phys., 99 [8] (2006), Article No. 08E913.

[99] J. Zou and J. Mabon, Web-based electron microscopy application software: Web-EMAPS, Microsc. Microsnal., 10 [Suppl 2] (2004).

[100] L. Peng, G. Ren, S. Dudarev and M. Whelan, "Robust Parameterization of Elastic and Absorptive Electron Atomic Scattering Factors", Acta Cryst. (1996). A52, 257-276.

[101] H. Müller and H. Rose, “Electron Scattering”, in “High-Resolution Imaging and Spectrometry of Materials”, Eds. by F. Ernst and M. Rühle, ISSN 0933-033X, ISBN 3-540-41818-0, Springer Series in Materials Scince, (2003).

[102] L. Peng, G. Ren, S. Dudarev and M. Whelan, “Debye-Waller Factor and Absorptive Scattering Factors of Elemental Crystals”, Acta Cryst. A5, 456-470, (1996).

[103] H. Heinrich, “High-resolution transmission electron microscopy for nanocharacterization”, in: “Functional Nanostructures. Processing, Characterization, and Applications”, Edited by S. Seal, in series “Nanostructure Science and Technology”, series editor: D. Lockwood, for a book entitled “Functional Nanostructures” (Editor: S. Seal) Springer Science and Business Media, LLC, (2007) 414-503.

[104] M. Tanaka, M. Terauchi and T. Kaneyama, “Convergent-beam electron diffraction II” JEOL, Tokyo, (1988).

[105] J. Croy, S. Mostafa, J. Liu, Y. Sohn, H. Heinrich and B. Roldan Cuenya, “Support dependence of MeOH decomposition over size-selected Pt nanoparticles”, Catal. Lett., 199 [3-4] (2007) 209-216.

[106] O. Savychyn, F. Ruhge, P. Kik, R. Todi, K. Coffey, H. Nukala and H. Heinrich, “Luminescence-center-mediated excitation as the dominant Er sensitization mechanism in Er-doped silicon-rich SiO_2 films”, Phys. Rev. B 76 (2007) 195419.

[107] G. Aliev, B. Goller, P. Snow, H. Heinrich, B. Yuan and R. Aigner, “Porous silicon bulk acoustic wave resonator with integrated transducer”, Nanoscale Research Letters, 7 (2012) 378

[108] B. Yuan, H. Heinrich, B. Yao and A. Dutta, “Quantitative measurement of volumes for nanoparticles by high-angle annular dark-field transmission electron microscopy”, Microsc. Microanal., 16 [Suppl 2] (2010) 1764-1765.

[109] T. Kaiser, W. Sigle, D. Goll, N. Goo, V. Srot, P. van Aken, E. Detemple and W. Jäger, “Transmission electron microscopy study of the intermixing of Fe–Pt multilayers”, J. Appl. Phys., 103 (2008) 063913.

[110] L. Ono, B. Yuan, H. Heinrich and B. Roldan Cuenya, “Formation and thermal stability of platinum oxides on size-selected platinum nanoparticles: Support effects”, J. Phys. Chem., C 114 (2010) 22119–22133.

[111] S. Mostafa, F. Behafarid, J. Croy, L. Ono, L. Li, J. Yang, A. Frenkel and B. Roldan Cuenya, “Shape-dependent catalytic properties of Pt anoparticles”, J. Am. Chemical Soc., 132 (2010) 15714-15719.

[112] B. Roldan Cuenya, J. Croy, L. Ono, A. Naitabdi, H. Heinrich, W. Keune, J. Zhao, W. Sturhahn, E. Alp and M. Hu, “Phonon density of states of self-assembled isolated Fe-rich Fe-Pt alloy nanoclusters“, Phys. Rev., B 80 (2009) 125412.

[113] R. Heidenreich, “Fundamentals of Transmission Electron Microscopy”, Wiley, (1964), New York.